MOLECULAR MECHANISMS IN EARLY PREGNANCY AND THE FEMALE REPRODUCTIVE CYCLE

by

YUEHUAN LI

(Under the Direction of Xiaoqin Ye)

ABSTRACT

With the decreasing fertility rate in women over the past decades, there's a pressing demand for investigating the factors affecting female reproduction. Both endogenous factors like genetic mutations and endocrine factors, and exogenous factors like viral infection and environmental exposures, can contribute to infertility and impaired fecundity in women. In this dissertation, we used different mouse models to investigate the contributing factors in female fertility. In Chapter 2, the functions of endogenous factors lysosome and lysosomal ion channels in the corpus luteum (CL) during early pregnancy were studied. By deleting the ATPase H^+ Transporting V0 Subunit D2 gene (*Atp6v0d2*) in *Mcoln1*$^{-/-}$ mouse model (*Atp6v0d2*$^{-/-}$*Mcoln1*$^{-/-}$), the impaired female fertility and deficiencies of CL histology and progesterone (P4) steroidogenesis in *Mcoln1*$^{-/-}$ were partially rescued in *Atp6v0d2*$^{-/-}$*Mcoln1*$^{-/-}$ mice, suggesting the restored lysosomal transmembrane potential in *Atp6v0d2*$^{-/-}$*Mcoln1*$^{-/-}$ CL and the lysosomal impacts on female fertility. In Chapter 3, the regulation of endogenous factor—P4, in uterine fluid absorption during early pregnancy were studied in the P4-deficient mouse model (*RhoA*$^{f/f}$*Pgr*$^{Cre/+}$) and control mice with the combination of exogenous P4 and P4 receptor-antagonist (RU486) treatments. By intraluminally injecting the fluorescent dye Alexa Fluor 488

Hydrazide (AH) into preimplantation uteri in the above mouse models, we found bulk absorption in uterine luminal epithelium (LE) is the major way of uterine fluid absorption on day 0.5 post-coitum (D0.5), which decreased from D0.5 to D3.5. P4-deficiency and RU486 treatment in mice decreased bulk absorption in LE in preimplantation uterine fluid absorption, while the autofluorescence dots on apical LE, most likely indicating endocytosis, had little regulation by P4 during preimplantation. In Chapter 4, we investigated the effects of exogenous factor, influenza A virus (IAV) infection, in cycling female mice. Infection with mouse-adapted H3N2 IAV (x31) decreased mouse body weights and caused lung injury, which is associated with arrested female estrous cycles and increased ovarian follicles in early developmental stages, while the histology and cellular activities in infected ovaries and uteri were comparable to uninfected counterparts. This dissertation advances our knowledge of contributing factors involved in female reproduction.

INDEX WORDS: female reproduction, early pregnancy, lysosome, corpus luteum, uterine fluid, progesterone, influenza A, immunology, estrous cycle.

MOLECULAR MECHANISMS IN EARLY PREGNANCY AND THE FEMALE REPRODUCTIVE CYCLE

by

YUEHUAN LI

B.S., Beijing Normal University, Beijing, China, 2017

A Dissertation Submitted to the Graduate Faculty of The University of Georgia in Partial Fulfillment of the Requirements for the Degree

DOCTOR OF PHILOSOPHY

ATHENS, GEORGIA

2023

MOLECULAR MECHANISMS IN EARLY PREGNANCY AND THE FEMALE REPRODUCTIVE CYCLE

by

YUEHUAN LI

Major Professor:	Xiaoqin Ye
Committee:	Rabindranath De La Fuente
	Vincent Joseph Starai

Electronic Version Approved:

Ron Walcott
Vice Provost for Graduate Education and Dean of the Graduate School
The University of Georgia
May 2023

ACKNOWLEDGEMENTS

Six years of PhD study is quite a journey in my life, and I've been deeply grateful to complete my PhD degree here in the Ye lab at the University of Georgia.

I would like to start with expressing my sincere gratitude to my mentor Dr. Xiaoqin Ye. She has been dedicating every effort in teaching and research on female reproduction. She guided me into the reproductive field when I knew nothing about it, and supported me along the way academically, financially, and emotionally. She provided generous help not only on my 'professional trainings', research projects and career goals, but also always made sure that our living expenses were covered by scholarships, even during difficult times. I had some dark times when I grieved over the loss of my relatives, but she and the Ye lab members were there to care and support me. She is over-qualified to be my 'academic mom', but a lifelong friend and mentor to me. I am grateful to be one of her 'lab children'!

I would like to acknowledge my committee members, Dr. Rabindranath De La Fuente and Dr. Vincent Joseph Starai. They gave many insightful suggestions and in-depth discussions that contribute greatly to my research progress. Thank you for your abundant support and generous help that advanced my research along the way!

All the Ye lab members are like family to me. The older brothers and sisters, Dr. Shuo Xiao, Dr. Honglu Diao, Dr. Fei Zhao, and Dr. Rong Li, who gave valuable advice and support to my research and life decisions. My big brothers, Dr. Zidao Wang and Dr. Christian Lee Andersen, who taught me all the bench and research techniques, and gave me life advice when I first stepped my feet into UGA. I'm also grateful to have four talented undergraduate students as

lab assistants, they are Rachel (Haeyeun) Byun, Suvitha Viswanathan, Jaymie Bromfield, and Moya Zhang. We've become close friends and I'll always remember you all as being the joy of the lab work. The younger brothers, Jonathan Matthew Hancock and Taylor Elijah Martin, who were the fast learners to 'inherit' lab techniques and my chaperones for the late-night experiments. They were also supportive and helpful to make accommodations for me during my last few months, and I really appreciated your helps!

I would like to thank the professors and staffs in our department, college, and URAR who took care of our needs, allowing me to focus on my research. Special thanks to Dr. Wendy Watford, and her lab members, Dr. Krishna Latha and Denise Fahey, for your guidance to the Influenza project. I'll always remember counting sperms in your lab on Saturday mornings.

I want to thank my family and the loving environment I grew up with. My grandparents who raised me up and supported me without condition, and I shall keep going with your love. My father, Zuoyong Li, who taught me how to be a good person and led me to the right path, who supported me studying abroad for my ambition and took pride in me. My mother, Guiying Zhang, a strong woman who picked herself up after grief and always prioritizes my needs. My uncles, aunts, and cousins, who looked after my mother and I with unconditional supports.

I'm also grateful to have so many great friends, old friends who are always on my side, and new friends I met in USA who are the cherries on top of my American dream. I want to thank my boyfriend, Huazhen Zhou, who gave me emotional support and treated me with 'feasts' when I felt stressed and depressed.

I also want to thank my naughty hamsters Sissi, and my moody but loving bunny Luna, who gave me emotional support through my dark days, I will always love you. Lastly, *Mus musculus* who made my research possible, you all will be remembered.

TABLE OF CONTENTS

Page

LIST OF FIGURES

Page

LIST OF ABBREVIATIONS

HPO axis: hypothalamic-pituitary-ovarian axis; **GnRH**: gonadotropin-releasing hormone; **LH**: luteinizing hormone; **FSH**: follicle-stimulating hormone; **E2**: estrogen; **P4**: progesterone; **CL:** corpus luteum; **PR**: progesterone receptor; **ER**: estrogen receptor; **ECM**: extracellular matrix; **VEGFA**: vascular endothelial growth factor A; **FGF2**: fibroblast growth factor 2; **PGF2α**: prostaglandin F2α; **StAR**: steroidogenic acute regulatory protein; **P450SCC/CYP11A1**: P450 side chain cleavage; **3β-HSD**: 3β-hydroxysteroid dehydrogenase; **GE**: uterine glandular epithelium; **LE**: uterine luminal epithelium; **D**: gestational day; **uNK**: uterine natural killer cells; ***Atp6v0d2***: Atpase, H^+ transporting, lysosomal V0 subunit D2; **V-ATPase**: vacuolar-type ATPase; **IVF**: *in vitro* fertilization; **ENaC**: amiloride-sensitive epithelial Na^+ channel; **CFTR**: cystic fibrosis transmembrane conductance regulator; **AQP**: aquaporin; **LRO**: lysosome-related organelle; **SNARE**: Soluble NSF Attachment REcepetor; **HSC70**: heat shock cognate 70 kDa protein; **LAMP2A**: lysosomal-associated protein-2A; **TRPML1**: transient receptor potential cation channel, mucolipin subfamily, member 1; ***Mcoln1***: Mucolipin 1; **EV**: extracellular vehicles; **IAV**: influenza A virus; **RNP**: ribonucleocapsids; **HA**: hemagglutinin; **NA**: neuraminidase; **M1**: matrix 1 protein; **M2**: matrix 2 ion channel protein; **PAMPs**: pathogen associated molecular patterns; **PRRs**: pathogen recognition receptors; **IFNs**: interferons; **IL**: interleukin; **MHC**: major histocompatibility complex; **Th:** T helper cells; **Treg**: regulatory T cells; **CTL**: cytotoxic T lymphocyte; **E3**: estriol.

CHAPTER 1

INTRODUCTION

The mammalian female reproductive system includes the ovary, oviduct/fallopian tube, uterus, cervix, vagina, and mammary gland. After puberty, when the female mammals become sexually mature, the complex regulatory network between the brain and the female reproductive system has been established. This network is regulated by the neuroendocrine axis: hypothalamic-pituitary-ovarian axis (HPO axis) and the sexual hormones secreted from the ovary [10]. In mammals, the regular pulse of gonadotropin-releasing hormone (GnRH) from the hypothalamus is essential for female fertility, which acts as a final output from the neuronal system and further regulates the pulsatile secretion of luteinizing hormone (LH) and follicle-stimulating hormone (FSH) from the anterior pituitary [11]. Together the LH and FSH convey the message to the ovary, where the hormones secreted from the ovary can further pass down the signals to the rest of the reproductive system and send feedbacks back to the hypothalamus and pituitary (reviewed in Figure 1.1 [6]) for the establishment of female cycle (menstrual cycle in women and estrous cycle in rodents) [6]. During the pregnancy, the exquisite communication between the ovary and the female reproductive tract, mostly through hormones and small signaling molecules, is the key to a successful conception. Endogenous (e.g. genetic mutations and cellular dysfunction) and exogenous disruptions (e.g. viral infection and medical treatment) to the communication and hormone production can contribute to impaired fertility and pregnancy failure.

1.1 Ovary, corpus luteum, and ovarian hormones

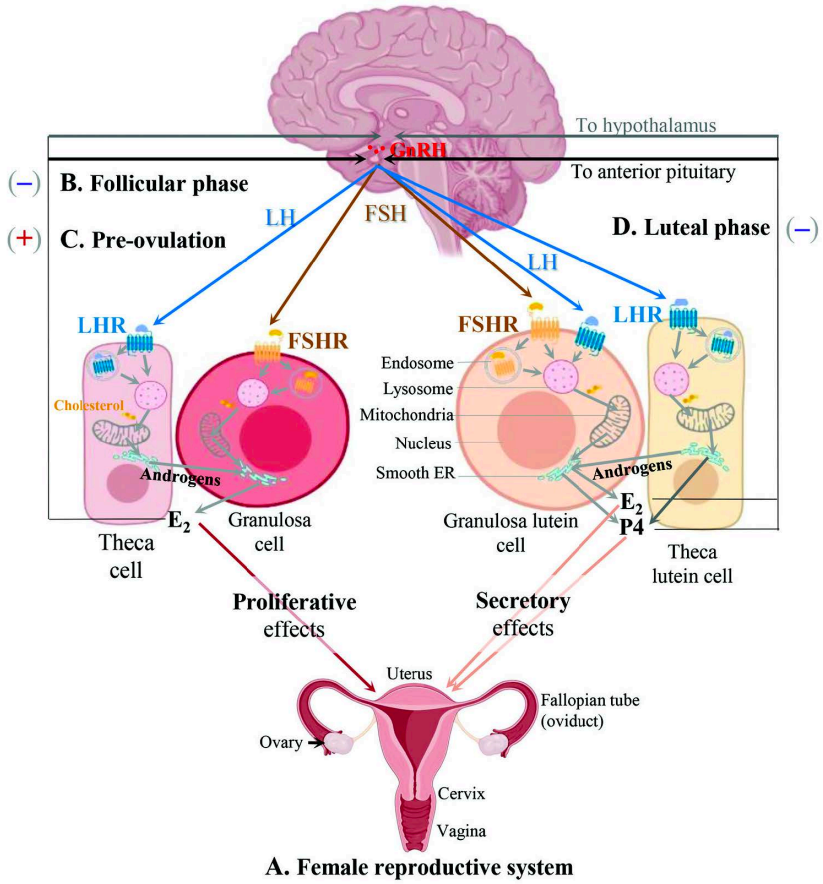

Figure 1.1. The regulatory network of HPO axis and the female reproductive system. Cited from Figure 5 in reference [6]. HPO axis: Hypothalamic-pituitary-ovarian; GnRH: Gonadotropin-releasing hormone; LH: Luteinizing hormone; FSH: Follicle-stimulating hormone; LHR: Luteinizing hormone receptor; FSHR: Follicle-stimulating hormone receptor; E2: Estrogen; P4: Progesterone.

1.1.1 Overview of the ovary and folliculogenesis

The ovaries are a pair of glands that located on either side of the uterus. They are dynamic organs that produce oocytes (also known as ova and eggs) and sexual hormones like estrogen (E2) and progesterone (P4), and the stages of oocytes development and hormonal production (steroidogenesis) varied throughout female reproductive cycles and pregnancy stages

[1]. The structure of ovary is also heterogenous, which generally includes ovarian follicles, corpus luteum, medulla, and surface epithelium in female mammals (Fig. 1.2, [1]). Ovary is also an essential part of the HPO axis to convey the messages from the central nervous system to the female reproductive system, and the ovarian functions are also regulated by the HPO axis [6]. The HPO axis drives different activities in the female reproductive system during different stages of the female cycle. Take the menstrual cycle as an example, during the follicular phase, GnRH from the hypothalamus induces the secretion of FSH and LH from the anterior pituitary, in which both drive the production of E2 from the ovarian follicle, where E2 can further regulate uterine

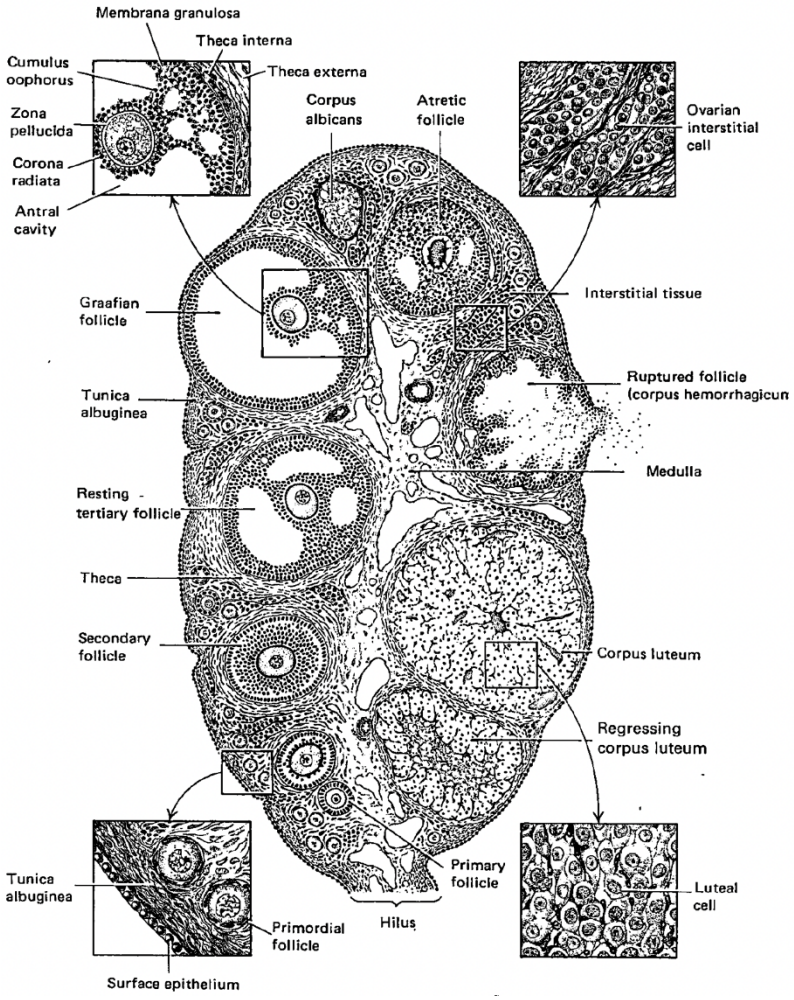

Figure 1.2. Internal structure of a dynamic ovary. Cited from Figure 2-3 p30 in reference [1].

proliferating effects and send negative feedbacks for FSH and LH production; whereas during the pre-ovulation time, E2 from the ovary drives positive feedbacks to reach FSH and LH surge and ultimately leads to ovulation; after ovulation (luteal phase), the ovulated ovarian follicle differentiates to corpus luteum which also responds to LH and FSH for P4 production, where P4 drives uterine secretory effects and also send negative feedbacks for FSH and LH secretion [6] (Fig. 1.1 [6]).

The ovarian follicle is the functional unit for oocyte development, which contains the oocyte and supportive somatic cells (granulosa cells and theca cells). The follicular development (also called folliculogenesis) starts from primordial follicles, to growing follicles (primary follicles and secondary follicles), and finally mature antral follicles (also called Graafian follicles) which are capable for ovulation [12] (Fig. 1.2, [1]). During the follicular development, the majority of the follicles undergo degeneration before ovulation are called atretic follicles, in which only less than 1% of the follicles can ovulate in mammalian ovaries [13]. The early phases of the folliculogenesis are gonadotropin-independent and regulated by intra-follicular factors, from the initial generation and differentiation of the primordial germ cells during the embryonic development to the continuous development to primordial follicles, primary follicles, and secondary follicles after birth [14]. After the primordial germ cells differentiate and proliferate in the genital ridge to form the oogonia, they further undergo partial meiosis to originate the oocytes. After birth, the oocytes are enveloped by a single layer of squamous (inactivated) granulosa cells to form the primordial follicle, which is a less-understood process regulated by mostly intrinsic factors like Forkhead Box O from the oocytes [14, 15]. Subsequently, the granulosa cells transform into a cuboidal shape (activated) and proliferate to the primary phase of the follicles. Under the control of predominately oocyte-secreted factors (like growth

differentiation factors and bone morphogenetic proteins) and granulosa cell-secreted factors, the follicles continue to expand and develop, featured with the proliferation of the granulosa cells, the formation of theca cells from the basement membrane of the outside granulosa cells, and the completion of first meiosis in the oocyte [14]. The regulatory factors involved in early stages of folliculogenesis are recently reviewed in [14, 15]. The later phases of the folliculogenesis are gonadotropin-dependent (regulated by the HPO axis), from the formation and maturation of antral follicles to ovulation. Antral follicles are characterized with a fluid-filled antrum cavity that separates the granulosa cells into cumulus granulosa cells surrounding the oocyte and mural granulosa cells forming the wall of follicles, which is regulated by FSH and LH and their responsive paracrine signals from granulosa cells and theca cells [14, 16]. Under the control of the HPO axis, the dominant antral follicle (not programmed for follicular atresia) undergoes progressively expansion through the proliferation of granulosa cells and the initiation of second meiosis of the oocyte to reach the pre-ovulatory stage [17]. The LH surge from the anterior pituitary during the midpoint of menstrual cycle stimulates the ovulation, featured with rupture of follicular wall and the detachment and expulsion of the cumulus-oocyte complex (ovum) into the oviduct in rodents and humans [1, 18].

1.1.2 Corpus luteum

After ovulation, the ruptured follicular wall inside the ovary remains as a collapsed sac, featured with clotted blood from the ovulation, which is called the corpus hemorrhagicum [1]. Followed with the remained granulosa cells and theca cells rapidly undergo a specific differentiation and tissue remodeling process, known as luteinization, to invade into the sac structure, the corpus hemorrhagicum quickly transforms into a transient yellow endocrine gland called corpus luteum (CL, plural: corpora lutea (CLs)) [1].

The luteinization is a sophisticated process that involves the cessation of cell proliferation, and the quick completion of cell differentiation, tissue remodeling, and vascularization within few hours to few days in most mammals. Before the ovulation, majority of the granulosa cells and theca cells in the preovulatory follicles are arrested at G_0/G_1 phase and exit from the proliferating cell cycle under the influence of LH and FSH and intracellular proteins like cyclins, cyclin-dependent kinases and cyclin-dependent kinase inhibitors [19, 20]. Under the control of LH surge, granulosa cells and theca cells undergo differentiation and become luteal cells. In some species like rodents, granulosa-derived and theca-derived luteal cells are miscellaneous throughout the corpus luteum without clear differences; in other species like humans and some domestic animals, theca-derived luteal cells are much smaller than granulosa-derived luteal cells with distinct responses to hormones and even different functions in primates [19, 20]. During the differentiation, granulosa cells become hypertrophy and transform from high to low nuclear-cytoplasmic ratio, with significant cellular changes in chromatin dispersion and mitochondrial morphology, and increased amounts of endoplasmic reticulum, Golgi complexes and lipid droplets, under the help of cytoskeleton proteins (like microtubule regulator: Ras homolog family member A) to fulfill the steroidogenesis functions as luteal cells [20, 21]. These changes are driven by the differential expression of hormonal receptors including FSH receptor, LH receptor, prolactin receptor, P4 receptor (PR), and E2 receptor (ER), and their responsive downstream molecules like cyclooxygenase-2, CATT/enhancer binding protein β, early growth response protein-1, and Nur77 (reviewed in [19]). Tissue remodeling is also a key step for CL formation. The remodeling of extracellular matrix (ECM) by proteases (e.g. matrix metalloproteinases) and their inhibitors, as well as the differential expression of follicular cell-surface glycoproteins are essential to assist follicular cell separation, migration, and

vascularization during luteinization [20]. As CL has one of the highest blood flow rates in organism, vascularization and angiogenesis are crucial during the luteinization. In the periovulatory follicles, the LH surge induces the breakdown of follicular basement membrane, the initial migration of endothelial cells, and the remodeling of the preexistent structure of follicular vasculature. After ovulation, these endothelial cells and its supporting cell—pericytes further migrate into the CL via ECM scaffold, along with extensive proliferation of these cells under the control of vascular endothelial growth factor A (VEGFA) and fibroblast growth factor 2 (FGF2). After colonization, these endothelial cells re-form the blood vessels under the help from pericytes, VEGFA, FGF2, and some platelet-derived factors to accomplish the vascularization in the CL [22].

In mammals, 1) if pregnancy does not occur or 2) if placenta takes over the P4 production (like in humans) or 3) at the term of delivery, the developed CL undergo regression/involution (also known as luteolysis), which 1) ensures the timely initiation of the next ovarian cycle or 2)&3) enables the on-site control of parturition. This process is quite controversial in two aspects: firstly, the presence of the CL and its function in steroidogenesis degenerate in different speeds in different species and during different reproductive time (ovarian cycle v.s. pregnancy); secondly, the mechanism of CL regression is primarily through apoptosis, but several studies indicate the involvement of other types of cell death like autophagy and necrosis [6, 20, 23, 24]. One well-known stimulator of the luteolysis is prostaglandin F2α (PGF2α), which mainly produced by the uterus. PGF2α can induce both the structural regression (decreased size and weight of CLs) through regulating cell death regulators and proteases, as well as the decreased steroidogenesis of CLs via suppressing responses to other hormones and re-directing the pathways in steroidogenesis [19].

1.1.3 Ovarian hormones

As an endocrine organ, one of the ovarian functions is to produce hormones through follicles and CLs. The two-cell-two-gonadotropin theory depicts the steroidogenesis pathways for E2 and P4 production in follicles and CLs under the control of HPO axis (Fig. 1.1&1.3). Take menstrual cycle as example, during the follicular phase, LH binds to its receptor in theca cell of developing follicles to produce androstenedione from the precursor of all steroid hormones—cholesterol. The androstenedione produced by theca cells diffuses to the nearby granulosa cells, where it will be further converted to estradiol (E2) under the control of FSH (Fig. 1.3 left) [1]. During the luteal phase or early pregnancy, the substantial steroidogenesis in the ovary is for P4 production in developed CL. The theca-derived luteal cells (theca-lutein cells)

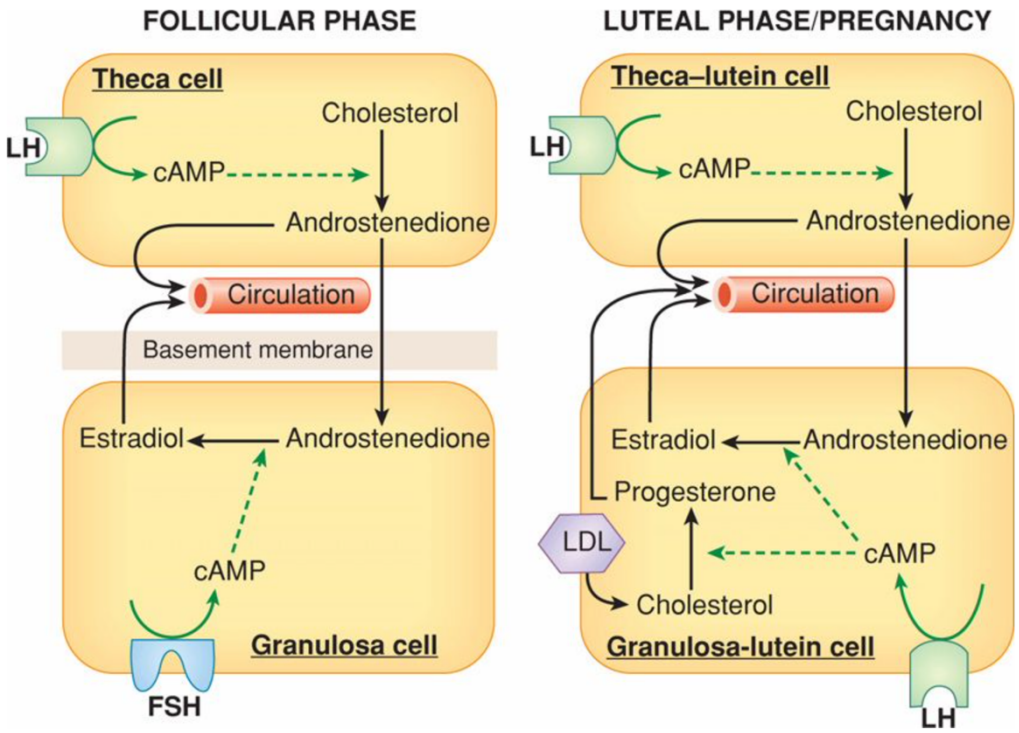

Figure 1.3. The two-cell-two-gonadotropin theory of ovarian steroidogenesis in follicles and CLs. Cited from Figure 5-2 in reference [5]. LH: luteinizing hormone; FSH: follicle-stimulating hormone; cAMP: cyclic adenosine monophosphate; LDL: low-density lipoprotein.

also response to LH and produce androstenedione as a precursor of P4 production in granulosa-lutein cells. However, granulosa-lutein cells become more autonomous, which they can synthesize E2, P4, and androstenedione from its own sources of cholesterol under the control of LH (Fig. 1.3 right) [19, 25]. Pathways involved in ovarian steroidogenesis are summarized in Fig. 1.4 [2]. Generally, the precursor cholesterol through whether uptake from the bloodstream by endocytosis or *de novo* synthesis from the endoplasmic reticulum within the cell can be stored as cholesterol esters in lipid droplets [26]. And the free cholesterol in the cytoplasm from lipid droplets or the two sources mentioned above will be transported to the mitochondria, in which the rate-limiting step of ovarian steroidogenesis occurs in the transport of cholesterol from outer to inner mitochondrial membrane via steroidogenic acute regulatory protein (StAR) [27, 28]. It is further converted to pregnenolone by P450 side chain cleavage (P450SCC/CYP11A1) on the

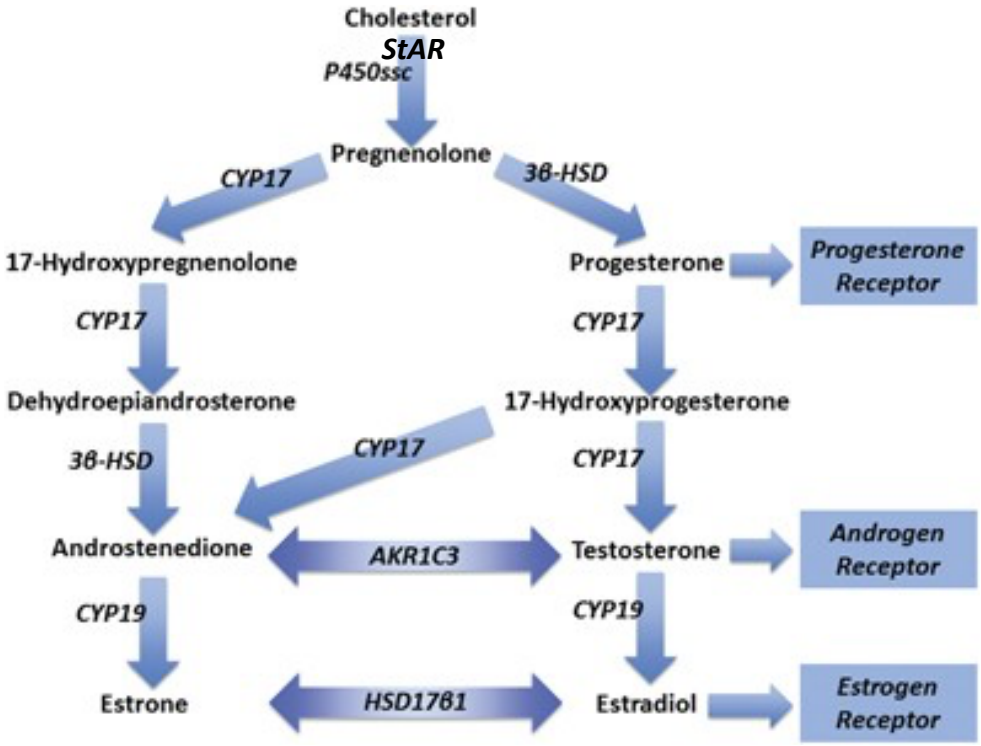

Figure 1.4. Detailed ovarian steroidogenesis pathways with major involved enzymes. Modified from Figure 1 in reference [2].

inner mitochondrial membrane and then transported to the smooth endoplasmic reticulum for P4 synthesis in luteal cells via 3β-hydroxysteroid dehydrogenase (3β-HSD) (Fig. 1.4) [27]. The E2 synthesis in follicular cells involves more steps and enzymes with two pathways and a required two-cell-two-gonadotropin system (Fig.1.3&1.4). During this process, some other steroid hormones like pregnenolone, androstenedione, and testosterone are produced in a less significant level (Fig. 1.4) [25].

1.2 Uterus in early pregnancy

1.2.1 Overview of the uterus

The uterus is currently the only site can support the embryo to develop to term, from embryo implantation to parturition. The shape of the uterus varied in different species, which is inverted pear-shaped in human and tubular-shaped (two uterine horns) in rodents [1, 4, 6]. The structure of the uterus, however, is conserved across species, which contains 3 layers in general: the outer layer perimetrium (also called the outer serosa), the middle muscle layer myometrium,

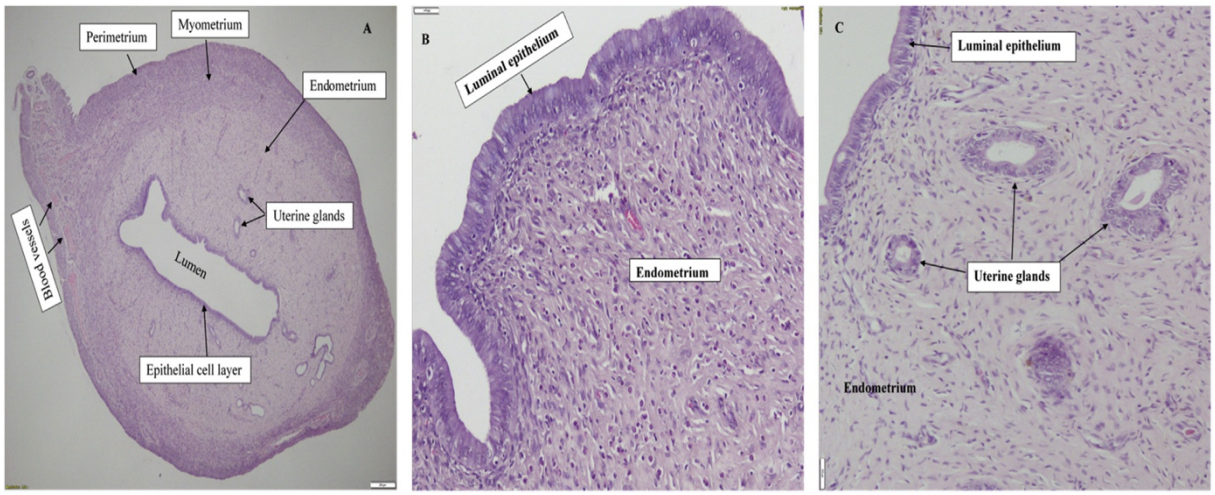

Figure 1.5. Cross sections of rat uterus. The magnification from left to right are 4x(A), 20x (B) , and 20x(C) with Hematoxylin-Eosin staining. Cited from Figure 4 in reference [7].

and the inner layer endometrium. The endometrium is heterogeneous and can be further divided into the stroma, the uterine glands (lining up by glandular epithelium, GE), and the uterine luminal epithelium (LE) that lining up the uterine lumen (Fig. 1.5).

The uterus, especially the endometrium, is a dynamic organ that responds to the changes of ovarian hormones E2 and P4 during female cycles in most mammals. In the menstrual cycle for humans (total length around 28 days), during the follicular phase, the stroma, LE, and GE undergo extensive proliferation under the control of high E2 level; during the luteal phase, the P4 dominant control induces vacuolization and secretion in uterine glands to create a spongy endometrium; menstrual phase starts when the levels of E2 and P4 droppped, with degeneration and slough of the endometrium as in menstrual discharge [1, 20]. The changes of uterus in estrous cycle (around 4-7 days) in rodents is similar to that in menstrual cycle except the absence

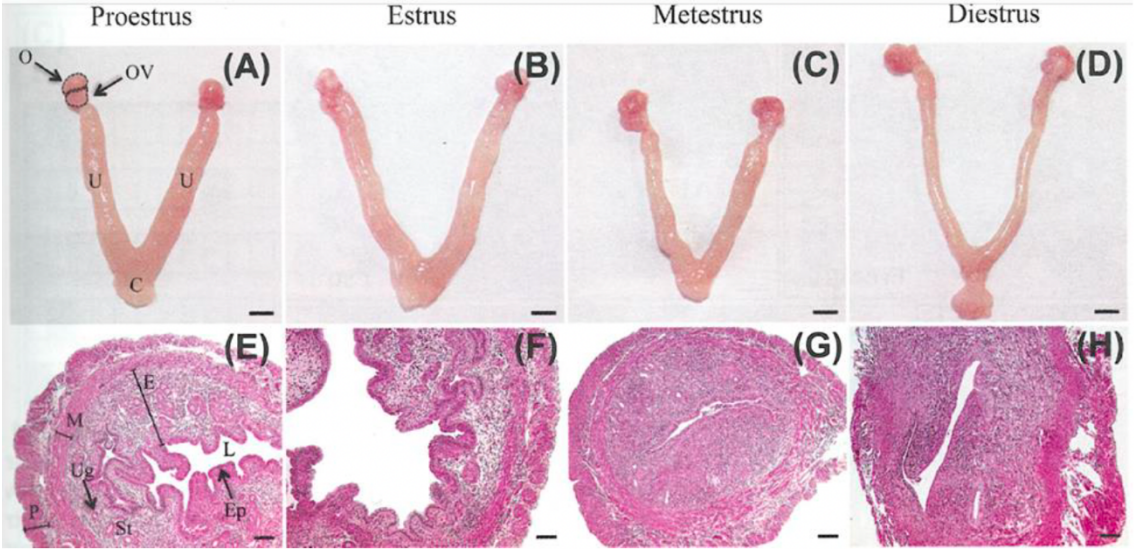

Figure 1.6. Mouse uterine macroscopy and microscopy during estrous cycle. A-D: Dissected female reproductive tract. E-H: Cross section of mous uterus stained with. Hematoxylin-Eosin. O: ovary; OV: oviduct; U: uterus; C: cervix; L: lumen; Ep: luminal epithelium; Ug: uttering glands; St: stroma; E: endometrium; M: myometrium; P: perimetrium. Scale Bar: 2mm for A-D; 0.1mm for E-H. Cited from Figure 2 in reference [4].

of the menstrual phase. There are four stages of estrous cycle featured with the pulsatile changes of E2 and P4: during proestrus and estrus stages, when E2 is the dominant hormones, endometrium proliferates and becomes thick and edematous with fluid-filled uterine lumen, featured with large lumen and lots of foldings on the LE (Fig. 1.6 A,B,E&F); during metestrus and diestrus, when P4 becomes dominant, uterus is elongated and the endometrium undergoes degeneration with ongoing vacuolization and apoptosis, as well as reduced uterine fluid in the lumen (small lumen with no folding on the LE) (Fig. 1.6 C,D,G&H) [4].

1.2.2 Uterine activities during early pregnancy

After ovulation, if fertilization occurs, the fertilized egg (the embryo) will start to develop in the oviduct and transport into uterus for further development. The embryo reaches the uterus on around day 3 post-coitus (D3) in mice and day 3-5 post-fertilization in human, where it continues to develop into blastocyst [29, 30].

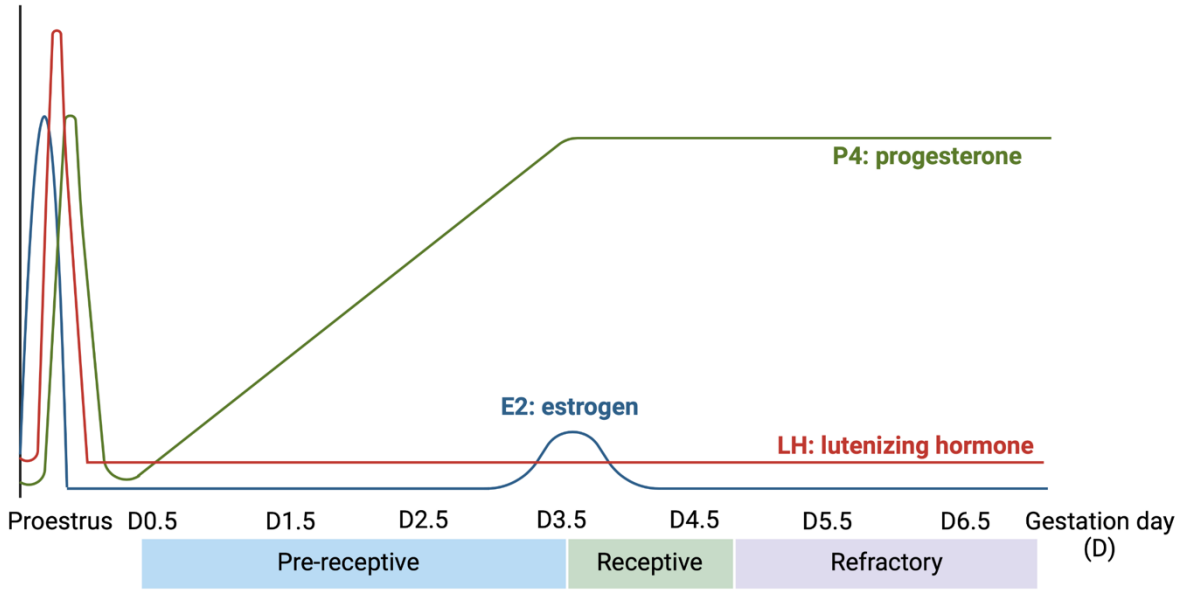

Figure 1.7. Hormonal regulation and uterine receptivity in mouse early pregnancy. Modified from reference [8]. The day with detected vaginal plug from mated female mice was designated as gestation day 0.5 (D0.5). The stages of uterine receptivity are defined in boxes.

In order to further support blastocyst growth, a successful pregnancy requires a receptive uterus for embryo implantation, which is referred to as the "implantation window". The implantation window is a limited period of time that is tightly regulated by the coordination of ovarian hormones P4 and E2 (Fig. 1.7). During the early pregnancy of mice, the preovulatory E2 surge induces LE proliferation, and the sequential P4 increase from the developing CL together with the nidatory E2 spike on D3.5, which work through their signaling networks via receptors PR and ER, further redirect the LE for differentiation and induce the stromal proliferation, which jointly establish the uterine receptivity for embryo implantation (Fig. 1.7 and Fig. 1.8A) [3, 29, 31]. Embryo implantation is the process by which the embryo, at blastocyst stage, apposes, attaches, and finally invades into uterus. The coordination between the embryo and receptive uterus must be achieved to enable a success implantation process. Embryo secrets factors, like

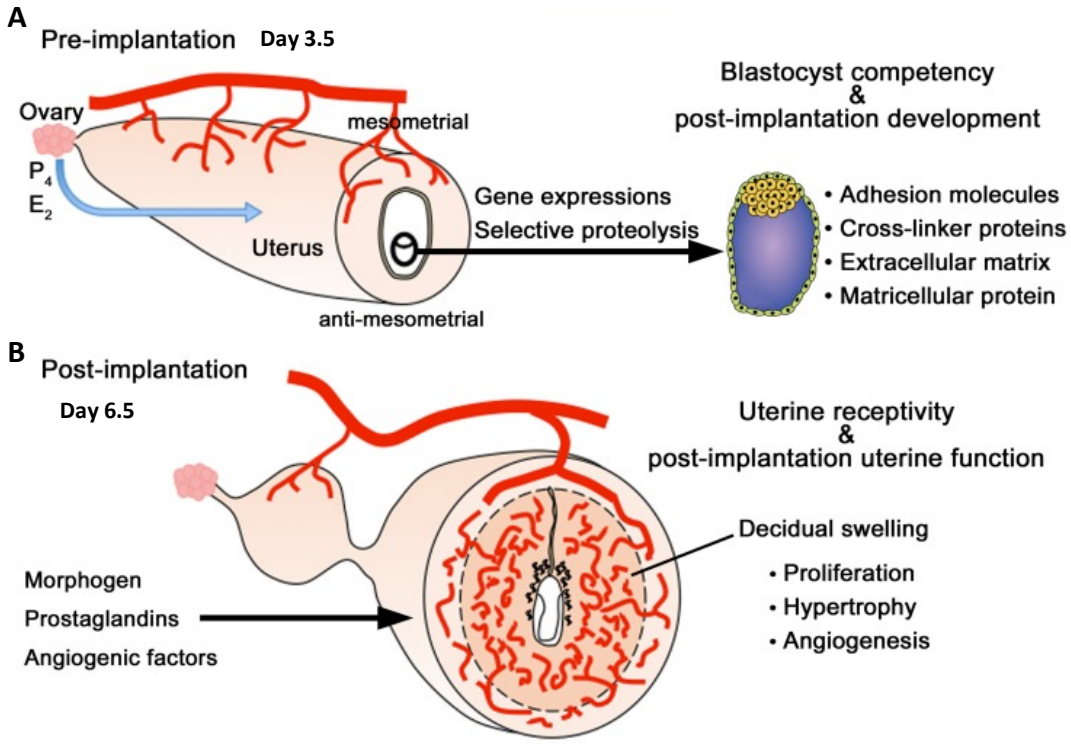

Figure 1.8. Factors regulating uterine receptivity and embryo implantation (A) and post-implantation (B). Modified and cited from reference Figure 2 in reference [3].

chorionic gonadotropin and cytokines, as well as extracellular vehicles and microRNAs to communicate with uterus [32]. In response to the embryonic signals, uterus in the receptive stage can further undergo cellular and molecular changes to facilitate the implantation. Implantation begins with the apposition of blastocyst to the LE. During this process, increased cyclooxygenase-driven prostaglandin E2 level in uterine LE and stroma responses to embryo apposition and help increase endometrial vascular permeability and embryo attachment. Afterwards, the embryo continues the attachment to the LE under the help of cell adhesion molecules like integrins, cadherins, selectins, and immunoglobulins. Finally, the trophoblast of embryo invades and migrates into the differentiated stromal cells called decidua, and reconstructs the maternal spiral arteries to make connection between maternal and fetus blood system for fetus development. Proteinase, growth factors and cytokines are involved in the penetration process [4, 33, 34]. Decidualization happens at the implantation sites after the embryo attachment to the LE, which is overall a remodeling process of the endometrium, including the differentiation of stroma, the influx of specialized uterine natural killer cells (uNK), the exclusion of maternal T and B cells, and the vascular remodeling (Fig. 1.8B) [29, 32]. This process only occurs during pregnancy in rodents but occurs regularly in every secretory phase of menstrual cycle in women, which is also controlled by E2 and P4. The remodeling of stroma featured with its differentiation from elongated, fibroblast-like mesenchymal cells into rounded, epithelioid-like decidual cells, with the secretion of several factors, like PRL and IGFBP-1, to facilitate embryo invasion, support angiogenesis, and modulate uterine immune system by rejecting T and B cells and promoting uNK influx, as well as placentation [34, 35].

Several studies have identified clusters of genes in the LE and endometrium that are differentially expressed during the peri-implantation time, which indicates the complex gene

network in the uterus to facilitate embryo implantation [36-38]. The application of mouse models, especially genetically engineered mouse models, together with the gene expression analysis, can further advance our standing of embryo implantation [39]. The acidification of the uterine epithelium (both LE and GE) during peri-implantation time is a novel finding from our lab via combining the gene expression analysis and the use of mouse models [29]. Our microarray analysis found a significant increase of the tissue-specific V0D2 subunit (*Atp6v0d2*) of vacuolar(H+)-ATPase (V-ATPase) on LE during mouse peri-implantation time [37]. The V-ATPase regulates the acidification of extracellular lumen when localized on plasma membrane and acidifies the intracellular organelles like lysosomes when localized on organelle membrane [40, 41]. We further detected the uterine epithelial acidification via LysoSensor Green DND-189, which is most likely from the lysosomal acidification in the epithelium and is associated with uterine receptivity in V-ATPase-inhibited and artificially-decidualized mouse models [42]. The detailed mechanisms and functions of epithelial acidification remain to be investigated [6].

The timely absorption of uterine fluid during early pregnancy is another contributing factor to successful embryo implantation. In human, patients with excessive uterine fluid accumulation have dramatically reduced embryo implantation rates after undergoing *in vitro* fertilization (IVF)-embryo transfer than the patients without uterine fluid accumulation, which suggests the importance of uterine fluid removal by the embryo implantation time [43, 44]. In mice, rapid uterine liquid absorption from D0.5 enables timely uterine lumen closure, which physically “locks” the embryo for intimate contact with LE for embryo implantation [29, 45]. Several *in vitro* studies and hormone-treated-ovariectomized rodents’ models confirms that ovarian hormone E2 promotes uterine fluid secretion, while P4 induces uterine fluid absorption, which the postovulatory P4 increase is expected to be the main regulator for preimplantation

uterine fluid absorption [29, 45-53]. One study ligated the uterine horn at oviductal and cervical ends in hormone-treated ovariectomized rats to prevent uterine fluid leakage from these two ends, but still observed the uterine fluid absorption upon P4 treatment, which indicates the absorption is mainly passing through the LE [46]. Ion channels on the apical side of LE like amiloride-sensitive epithelial Na^+ channel (ENaC) and cystic fibrosis transmembrane conductance regulator (CFTR), and those expressed on basolateral sides like Na^+/K^+ ATPase and other K^+ channels can create an osmotic gradient across the LE, which is the main driven force for the uterine fluid movement (secretion and absorption) [29, 45, 49, 51-54]. The uterine fluid absorption is also amiloride-sensitive, in which 100μM of intrauterine amiloride can reduce more than half of the fluid absorption in P4-primed rats, suggesting the major role of ENaC and other amiloride-sensitive channels in this absorptive function [29, 51, 52]. The water movements across the LE are primarily through water channels (aquaporins, AQPs), in addition to limited passive diffusion and paracellular flows of water through the LE. The AQPs have 13 family members (AQP 0-12), and AQP 4 and 5 are expressed on the uterine epithelium during peri-implantation in mice, in which AQP4 maybe involved in fluid absorption while AQP5 seems to be related to fluid secretion from the uterine glands [55-57]. The molecular mechanisms and detailed fluid passage of uterine fluid absorption during the pre-implantation time remain to be elucidated.

1.3 Functions of lysosome in female reproduction

1.3.1 Introduction of the lysosome

Lysosome is the most acidic organelle, in which the acidic lumen pH ~4.5-5.0 is optimal for more than 60 hydrolytic enzymes in it, like proteases, lipases, and phosphatases, etc [58, 59].

The acidity of lysosome is mainly regulated by V-ATPase on the lysosomal membrane to pump H^+ into the lysosomal lumen, while other ion channels on the lysosomal membrane help maintain the membrane potential across the lysosomal membranes and work as cellular signal transducers [6, 60]. Known as the digestive center in the cell, the lysosome also plays roles in vesicle trafficking (endocytosis and exocytosis), autophagy, cell death, metabolic signaling, and immune response [58, 61, 62].

Endocytosis delivers substrate to lysosomes for degradation [59]. There are generally four types of endocytosis: clathrin-mediated endocytosis, clathrin-independent endocytosis, pinocytosis, and phagocytosis (Fig. 1.9 A-D). Clathrin-mediated endocytosis involves clathrin and other modular proteins, which transiently assemble around the cytoplasmic face of the invaginated plasma membrane, select and concentrate cargo molecules, and shape the plasma membrane into a clathrin-coated endocytic vesicle [63]. Following the scission of the vesicle from the plasma membrane, the clathrin coat dissociates rapidly. The naked vesicle will either become an early endosome or fuse with an early endosome, both of which will eventually fuse with lysosomes for processing the cargo molecules [64] (Fig. 1.9A). Clathrin-independent endocytosis involves distinct coats (caveolae) or no specific coated intermediates [65]. The most common clathrin-independent pathway of endocytosis is mediated by caveolae (singular, caveola), which are a special type of lipid raft with caveolins and other proteins on small invaginations of the plasma membrane. The protein machinery may also involve the selection of cargo molecules. A caveola can detach from the plasma membrane and form a vesicle-like carrier called “endocytic caveolar carrier” [65]. The carrier with cargo molecules can be fused with early endosomes and eventually the lysosomes for processing cargo molecules (Fig. 1.9B). Pinocytosis involves the internalization of non-specific cargoes of extracellular fluids with

solutes. The pinocytosis vesicles are derived from invaginated pouches on the plasma membrane. After detaching from the plasma membrane, they will be internalized and fused with lysosomes for digestion of the cargoes [66] (Fig. 1.9C). Phagocytosis involves the plasma membrane in engulfing large extracellular particles. It is mediated by actin-dependent mechanism. Phagocytic cells express receptors that can recognize distinct molecular signatures endogenous to the target, or opsonic receptors that bind to opsonin deposited on the target. Receptor-ligand clustering triggers the formation of a phagocytic cup enclosing extracellular particles. The closure of the phagocytic cup will result in a phagosome, which will be internalized and fused with lysosomes to form phagolysosomes for elimination of the cargoes [67] (Fig. 1.9D).

The lysosome is also involved in exocytosis. The involvement of lysosomes in exocytosis is a relatively new discovery and less studied, as this function of lysosomes has little relationship to the conventional degradative role. It is now becoming clearer that lysosomes, along with modified lysosomal vesicles (also known as lysosome-related organelles, (LROs)), can be transported to the plasma membrane and fused with the plasma membrane to release the lysosomal contents into the extracellular space. The lysosome exocytosis is a highly regulated process. Upon stimulation, the increase of intracellular calcium level (sensed by synaptotagmin VII) or the depletion of cholesterol can both trigger lysosome exocytosis. With the help from microtubules and actins, the transport of lysosomes and LROs is regulated by Rab GTPases. The fusion of lysosomes and LROs with plasma membrane is facilitated by Soluble NSF Attachment REcepetors (SNAREs). Detailed mechanisms of lysosomes in exocytosis are still under investigation. Some known functions of lysosomal exocytosis include membrane repair during damage and infection, extracellular component degradation in bone remodeling and catabolism of lipoproteins, and delivery of proteins into cell surface in immune response [68] (Fig. 1.9F).

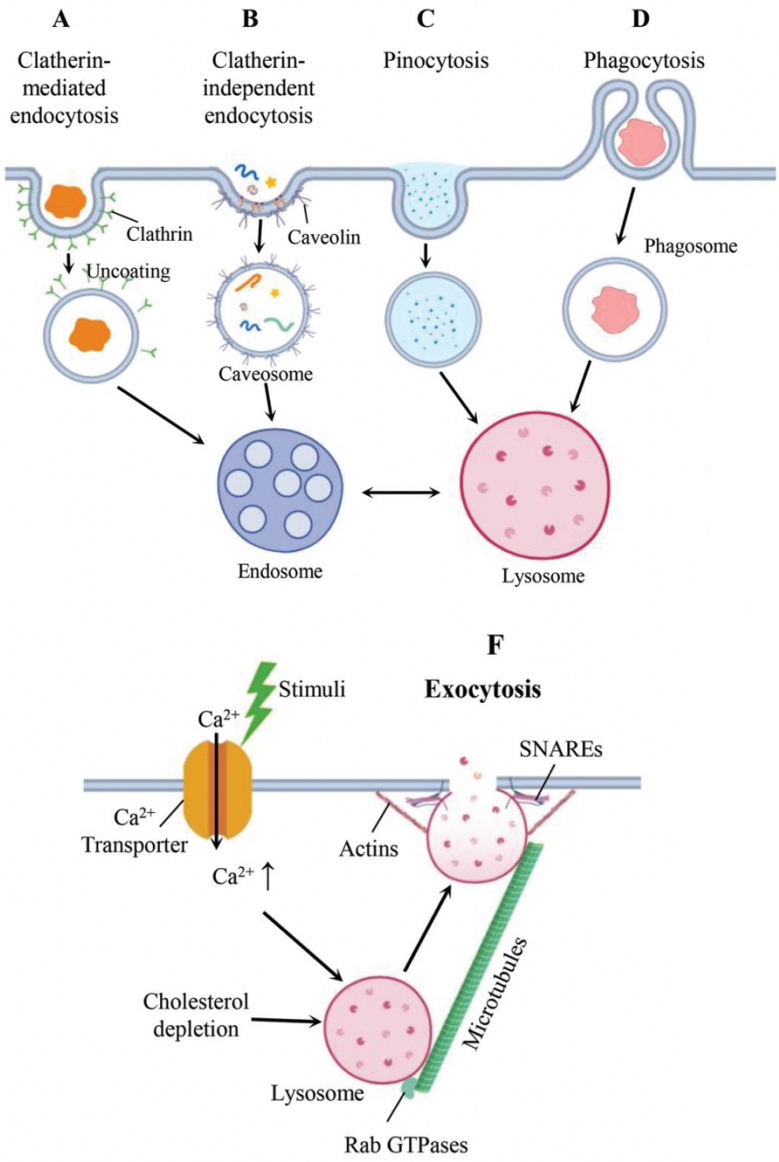

Figure 1.9. Main types of endocytosis and exocytosis involving lysosomes. Modified and cited from reference Figure 1 in reference [6].

Autophagy is an intracellular recycling pathway that delivers unwanted cytoplasmic components of endogenous or exogenous origin to the lysosome for degradation and nutrient cycling. Autophagic activity is upregulated under conditions like nutrient deprivation, oxidative stress, hypoxia, inflammation, and infection. There are three main types of lysosome-based autophagic pathways: macroautophagy, microautophagy, and chaperone-mediated autophagy

(Fig 1.10) [69]. Macroautophagy is the most dominant and well-studied autophagic pathway. The unwanted cytosolic components will be sequestered by a double-membraned vesicle called autophagosome, which will be fused with the lysosome to form autolysosome for digesting the sequestered cargoes [70] (Fig. 1.10A). Chaperone-mediated autophagy uses its unique machinery to degrade selected individual proteins in the cytoplasm without the formation of vacuoles. It requires a cytoplasmic complex of chaperone proteins including heat shock cognate 70 kDa protein (HSC70), which selectively recognizes and interacts with cytosolic proteins via their KFERQ-like motif. The substrate and HSC70 complex will interact with the transport receptor lysosome-associated membrane protein 2A (LAMP-2A), leading to LAMP-2A oligomerization and substrate translocation into the lysosomal lumen for degradation [71] (Fig. 1.10B). Microautophagy is defined as the direct engulfing and transporting of cytosolic components by

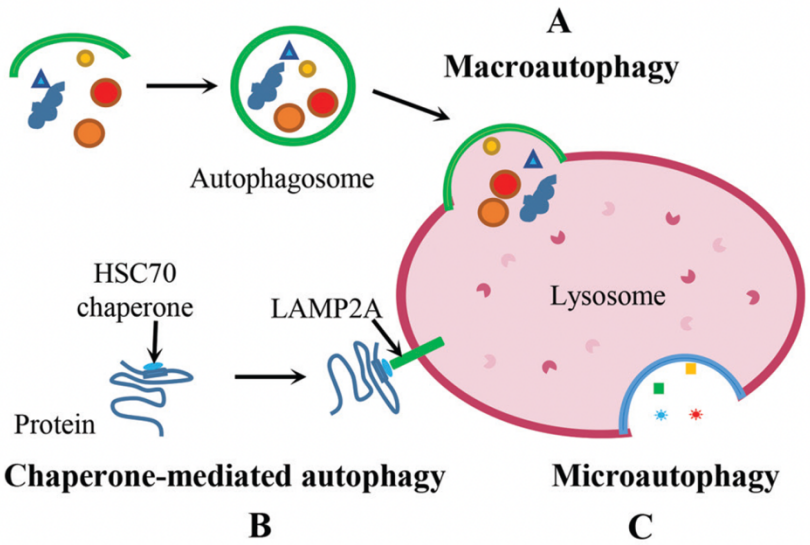

Figure 1.10. Three types of autophagy and their fusion with lysosome. (A) Macroautophagy. (B) Chaperone-mediated autophagy. (C) Microautophagy. HSC70: heat shock cognate 70 kDa protein; LAMP2A: lysosome-associated membrane protein 2A. Modified and cited from reference Figure 2 in reference [6].

lysosomal membrane into the lumen of the lysosome for digestion. A set of proteins have been identified to be important for microautophagy, but the molecular details of microautophagy remain to be explored [72] (Fig. 1.10C). The functions of autophagy in the female reproductive tract were recently reviewed [73].

Lysosomes play critical roles in cell death. Not only by endocytosis and autophagy can lysosomes help eliminate the waste from dead cell, but also the changes on lysosomal membrane permeabilization can release its digestive enzymes and trigger other types of cell death, such as apoptosis, necrosis, pyroptosis (a highly inflammatory form of programmed cell death in which cathepsins are involved), and ferroptosis (a type of programmed cell death dependent on iron and characterized by the accumulation of lipid peroxides) [74]. In addition, lysosomes are also implicated in cell death by entosis, the engulfment of one cell into another cell [75] (Fig. 1.11).

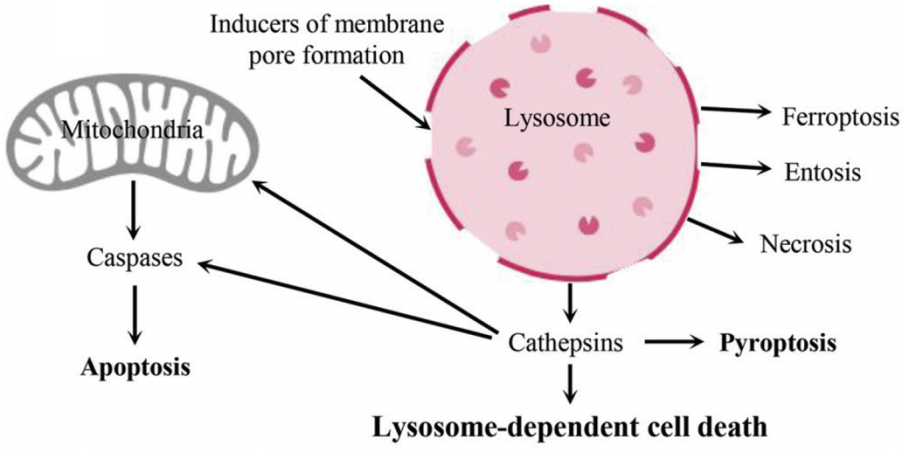

Figure 1.11. The involvement of lysosome in different types of cell death. Modified and cited from reference Figure 3 in reference [6].

1.3.2 Functions of the lysosome in female reproduction

We have recently reviewed the functions of the lysosome in the mammalian female reproductive system in [6] (Fig. 1.12).

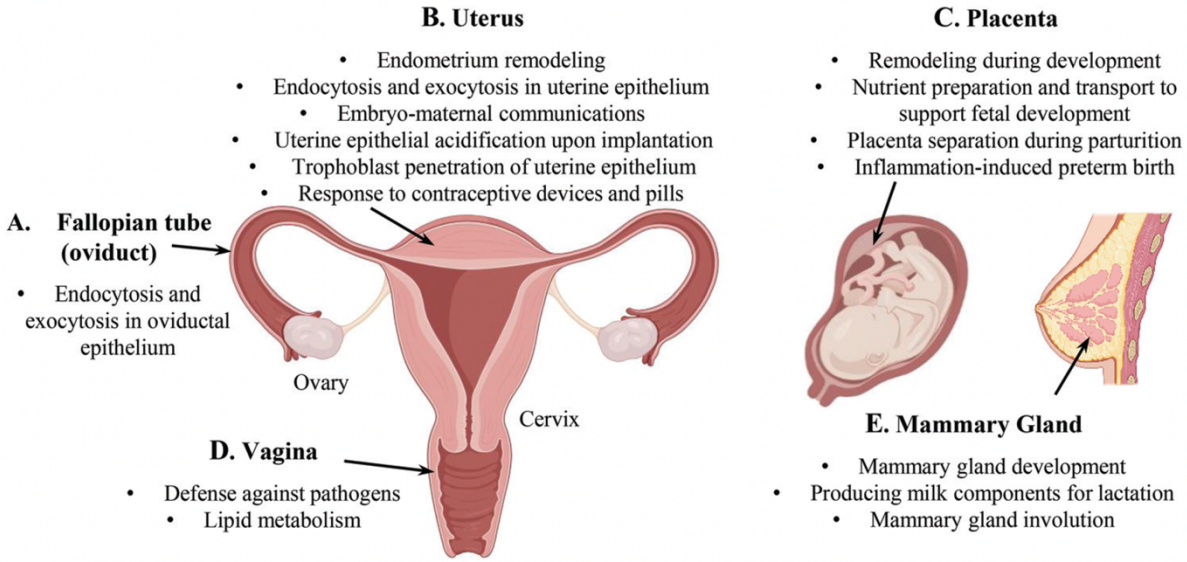

Figure 1.12. Summary of the known and suggested functions of lysosome in the female reproductive system (except ovary). Cited from reference Figure 4 in reference [6].

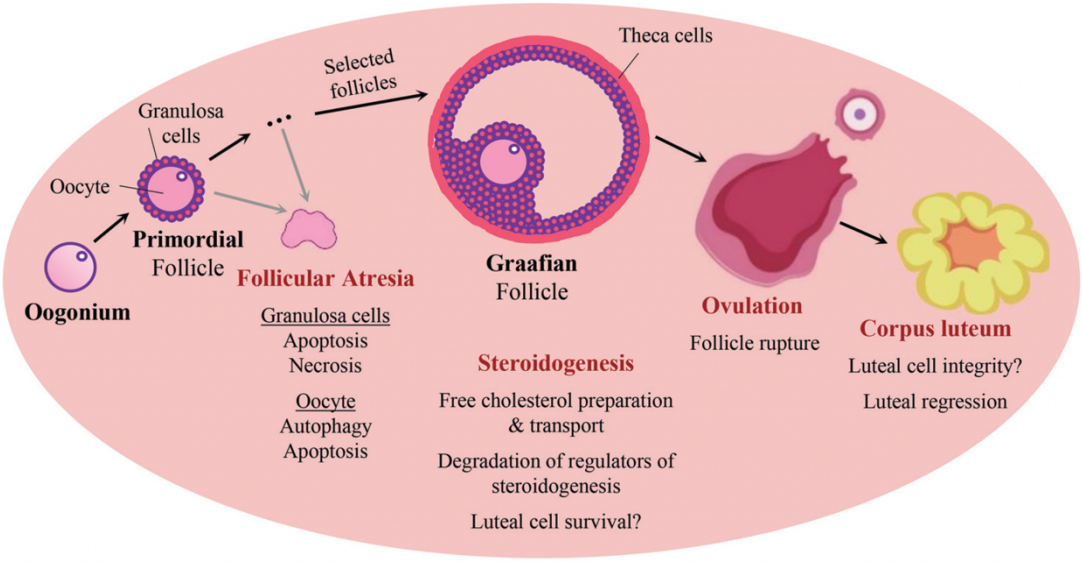

Figure 1.13. Summary of the lysosomal involvement in the ovary. Cited from reference Figure 6 in reference [6].

In the ovary, lysosome is involved in ovarian follicle atresia, ovulation, CL maintenance and regression, and steroidogenesis (Fig. 1.13). During the follicular atresia, lysosomes function in the depletion of granulosa cells through lysosomal membrane permeabilization for apoptosis

and necrosis [76-80], and assist in the degeneration of oocyte via autophagy and apoptosis [81, 82]. During the ovulation, lysosomes in the epithelium covering the pre-ovulatory follicles would aggregate at the plasma membrane, and then release the lysosomal enzymes into the extracellular space for follicle rupture to induce ovulation [83, 84]. As for the CL maintenance, our study from the *Mcoln1*$^{-/-}$ (encodes protein TRPML1 (transient receptor potential cation channel, mucolipin subfamily, member 1), an important lysosomal counter ion channel) female mice showed progesterone deficiency from the CL, and luteal cell degeneration and vacuolization, which suggests a novel role of lysosome in luteal cell survival and steroidogenesis [85]. CL regression is associated in increased number and size of lysosomes and lysosomal enzymes, as well as lysosomal-related cell death including autophagy, apoptosis, and necrosis [86-88]. In ovarian steroidogenesis, lysosomes have essential roles in releasing the free form of cholesterol, the common precursor for steroid hormones, from endosomes through lysosomal enzymes including Niemann-Pick type C (NPC) proteins--NPC1, a lysosomal membrane protein responsible for exporting free cholesterol, --and NPC2, a small and soluble protein binding cholesterol in the lysosome lumen [26, 27, 89] (Fig 1.1). Lysosomes are also in charge of the degradation and recycling of the regulators of ovarian steroidogenesis, like the LH-LHR and FS-FSHR complexes, and intrinsic receptors of PGF2α (Fig 1.1) [90-92].

In the oviduct, limited studies have implicated lysosomes in endocytosis and exocytosis in mouse, and potential replenishment of oviductal isthmus epithelium in large animals (Fig. 1.12A). Endocytosis and exocytosis activities, indicated by the localization of intravenously injected tracers, were found in the pre-ampulla segments of the oviduct during the early- and mid-pregnancy in mice, in which the involvement of lysosomes was unclear [93, 94]. However, a proteomics study detected the presence of several lysosomal enzymes in the bovine oviductal

fluid, which also suggested the lysosomal function in exocytosis in oviductal epithelial cells that lining up the oviductal lumen [95]. In the early pregnancy of sheep and goat, many lysosomes and lysosome-like bodies were found in the epithelium of the isthmus segment of oviduct, which suggests their roles in oviductal epithelial replenishment [96, 97].

In the uterus, the endocytosis and exocytosis in uterine epithelium, endometrium remodeling and uterine epithelial acidification (as mentioned in chapter 1.2.2) during peri-implantation, embryo-maternal communication, and responses to contraceptives are related to lysosomal functions (Fig. 1.12B). During the menstrual cycle of uterus, increased autophagy and apoptosis were found from proliferative phase to secretory phase; increased lysosomal activities were detected in the GE of secretory phase; macrophages enriched with lysosomal enzymes help with endometrial degeneration during menstrual phase; which all imply cell-specific functions of lysosomes during different menstrual stages [98-100]. The endocytosis and exocytosis activities in the mouse LE during early pregnancy are summarized in Fig 1.14. On D0.5 pre-implantation time, the intravenously injected tracer can be found on the basolateral membrane of LE, which

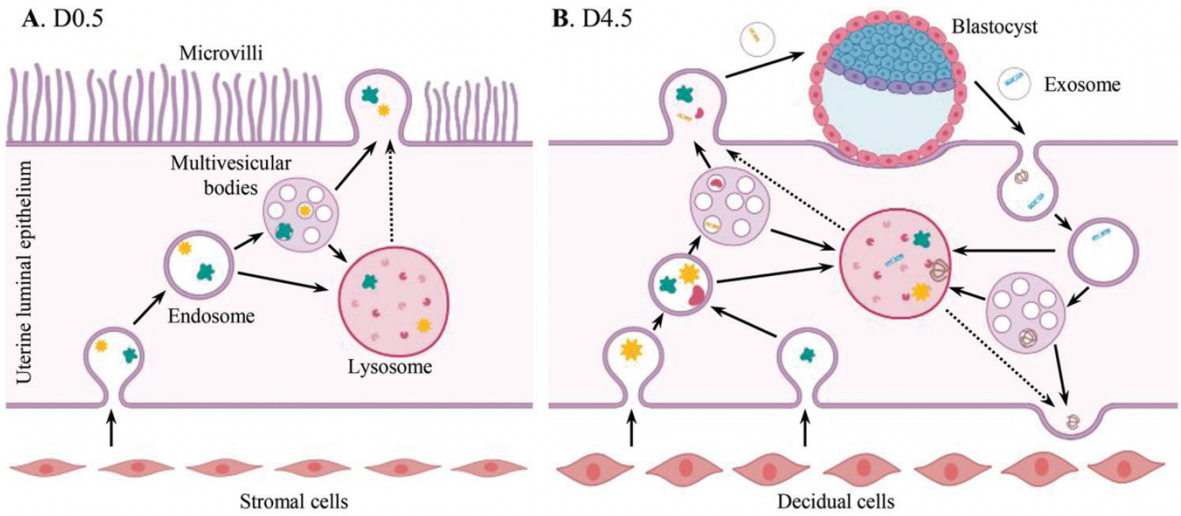

Figure 1.14. Summary of the endocytosis and exocytosis activities in mouse uterine luminal epithelium during early implantation. Cited from reference Figure 7 in reference [6].

indicates endocytosis activity where the endocytic cargo can be further fused with lysosome for degradation or redirect for exocytosis to the apical side of LE (Fig. 1.14A) [101]. On D4.5 implantation time, exocytosis on the apical LE and more endocytic activities were found on the basolateral LE, with large amount of endocytosis on the apical LE were detected by intrauterine-injected tracer (Fig. 1.14B) [101]. During the embryo implantation time, the establishment of uterine receptivity (uterine tissue remodeling) and stromal decidualization are both associated with increased number of lysosomes and lysosomal enzymes [100, 102-105]. When the embryo penetrates the LE during the implantation in rodents, the removal of LE cells through phagocytosis is associated with lysosomal functions [106, 107]. As previously mentioned in chapter 1.2.2, we used LysoSensor Green DND-189 (pKa ~5.2) to detect a novel phenomenon of uterine epithelium acidification during the peri-implantation time, in which this acidification is most likely in lysosomes due to its pH range (pH < 5.0) [42]. The communications between the embryo and the maternal side during the implantation time requires increased endocytosis and exocytosis on apical LE, especially the uptake of the embryo-derived extracellular vesicles (EVs). The fate of the EVs after endocytosed by the LE can be controlled by the lysosomes (Fig. 1.14B) [108, 109]. From a pharmacology view, increased number of lysosomes and release of lysosomal enzymes were seen in the blastocysts and endometrium after the treatment of hormonal and non-hormonal contraceptives, which implies the lysosomal responses in contraception [110-112].

In the placenta (Fig. 1.14C), lysosomal enzymes (like cathepsins) and autophagy-related proteins have different expression pattern in different cell types and different stages of placentation [113-116]. The role of lysosomes in nutrient transport in the placenta has been implicated in the pigs, which have extensive lysosomal system on maternal-fetal surface during

the mid-late gestation to support fetal development [117]. During the parturition process, dramatic increase of activities from lysosomal enzymes were found in the maternal tissues surrounding the placenta, suggesting the involvement of lysosomes in placenta separation [118]. Similar to this, altered autophagy activities was detected in inflammation-induced preterm labor, in which lysosome is one of the regulators [119].

In the cervix and vagina, changes of lysosomal enzymes and lysosomal activities were shown to be related to infection-induced metabolic responses and hormonal-controlled epithelial remodeling (Fig. 1.14D) [120-123].

1.4 Influenza and female reproduction

1.4.1 Introduction of the influenza A

Influenza (also known as flu) is a zoonotic respiratory disease that is cased by influenza viruses. Seasonal influenza result in 3-5 million severe illnesses with 0.29-0.65 million respiratory deaths globally [124]. There are four types of influenza viruses, A (IAV), B, C, and D, in which IAV is the only known type can cause pandemic influenza, which can cause more serious illness than seasonal flu [124, 125]. IAV is usually in spherical shape and is composed of a lipid envelop, matrix proteins and viral ribonucleocapsids (RNPs), which comprised with eight single stranded negative sensed RNAs with nucleoproteins and viral RNA polymerase [126] (Figure 1.15A). Four major types of proteins are found on the IAV envelop: hemagglutinin (HA), neuraminidase (NA), matrix 1 protein (M1), and matrix 2 ion channel protein (M2) (Figure 1.15A) [127]. HA can recognize the host receptor α-2,6-linked sialic acid (for most

human tissues) or α-2-3-linked sialic acid (for most birds) and help with virus entry into the host cell; NA plays major roles in the release of replicated viruses, while M1 helps in the formation of

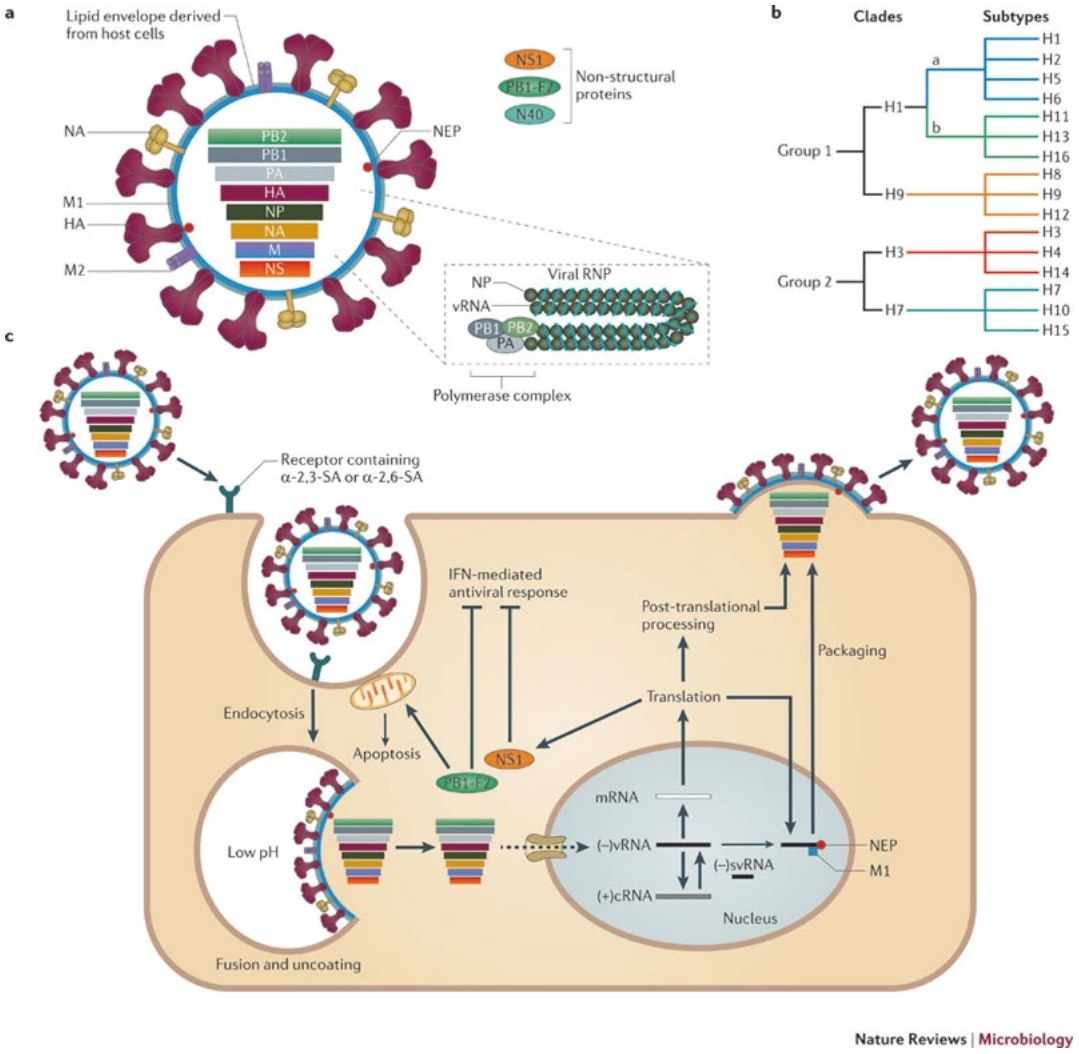

Figure 1.15. Summary of the Influenza A structure (A), classification (B), and replication (C). (A)NA: neuraminidase; HA: haemagglutinin; M1&M2: matrix proteins 1and 2; NEP: nuclear export protein; RNP: ribonucleoprotein; NP: nucleoprotein; PB1,PBZ, and PA: RNA-dependent RNA polymerase complex; NS1: non-structural protein 1. (C) α-2,6-SA or α-2,3-SA: α-2,6-linked or α-2-3-linked sialic acid; (-)vRNA: negative-sense viral RNA; (+)cRNA: complementary positive-sense RNA; (-)svRNA: negative-sense small viral RNAs. Cited from reference Figure 1 in reference [9].

the replicated viruses and M2 aids in viral fusion with the host. M2 and NA are the main targets for anti-IAV drugs like neuraminidase inhibitors and adamantanes antiviral drugs [127]. The classification of IAV is based on its surface proteins HA and NA, with 16 HA subtypes (H1-H16) and 9 NA subtypes (N1-N9) were divided into two major groups and five clades (Figure 1.15B), and H1N1 and H3N2 are the most circulating subtypes in human [124, 127].

The IAV infection/replication starts with the recognition of α-2,6-linked or α-2-3-linked sialic acid on the host cell through its surface protein HA, which leads to the receptor-based endocytosis/internalization of IAV [9] (Figure 1.15C). The acidic pH in endosomes both activates the conformational change in the HA, which induces the fusion of virus with the endosomes to release the viral RNPs into host's cytoplasm, and opens the M2 ion channel, which decreases the pH inside virion to also help the fusion process and trigger the uncoating of the viral RNP complex for replication [9, 128]. The adamantanes class drugs targeting M2 can block the fusion process and the replication of IAV [129]. Under the help from viral nuclear localization signals, the released RNPs are transported into the host's nucleus, where the negative sensed viral RNA will be transcribed by viral RNA polymerase into one mRNA for viral protein synthesis, one positive sensed complementary RNA for viral RNA replication, and some negative sensed small viral RNAs as regulators of the IAV replication [9, 130]. The replication of envelope proteins like HA, NA, and M2 starts with the protein synthesize from the transcribed viral mRNA in the endoplasmic reticulum, and then undergoes post-translational modification in the Golgi apparatus. The mature proteins and replicated viral RNAs are translocated to the host's plasma membrane under the assistance from Golgi apparatus and endoplasmic reticulum network, respectively [9, 126, 130]. The packaging of new viruses from those mature proteins and viral RNAs are regulated by M1 protein and nuclear export protein on

the host cell surface, from there the assembled IAVs buds out from the host cell mediated by the enzymatic activities from NA, which can release the newly formed viruses and destroyed the sialic acid on the host surface to avoid repeated infection on the same host [9, 130]. Anti-IAV drugs belong to the neuraminidase inhibitors family can block the activity of NA, therefore prevent the virus release and reduce the IAV infectivity [130].

IAV has high genetic variability due to its error-prone RNA polymerases, which increases the mutation rates during viral RNA replication; it also has high morphological and compositional variability for its surface proteins HA and NA due to the 'low-fidelity' of its protein assembly process [131]. The dynamic nature of IAV makes it easier to generate new subtypes by genetic reassortment and eventually to create the antigenic shift; at the same time the immune selection via the neutralization of antibodies targeting certain types of HA and NA but not the other types can cause the antigenic drift [9, 127, 129]. Both the antigenic shift and drift of IAV can have great impact on the effectiveness of antibody-based IAV vaccines and the potential of emerging new IAV pandemics [9, 129].

1.4.2 Immune response to influenza A infection

Upon IAV infection, the host immune system defends against infection through innate immune response, as well as hormonal and cell-mediated adaptive immunity.

The innate immune response is the first and fastest defense, usually happened in the epithelial cells in the airway and alveola as the primary targets of IAV infection, which initiates with the recognition of viral RNAs as the pathogen associated molecular patterns (PAMPs) by host pathogen recognition receptors (PRRs), including the retinoic acid inducible gene I protein, toll-like receptors and etc [132, 133]. Each PRR can detect a specific type of PAMPs that's unique to pathogens and not shared by the host, and further trigger the signaling pathways for the

production of interferons (IFNs) and pro-inflammatory cytokines like interferon 6 (IL-6), and IL-1β. These interferons and cytokines can induce the anti-viral signaling cascades and recruit immune cells including macrophages, dendritic cells, and natural killer (NK) cells, which all contribute to the defense/restriction against IAV infection [132-134].

The innate immune response activates the adaptive immunity for IAV clearance. The cell-mediated immunity relies on $CD4^+$ (helper) and $CD8^+$ (cytotoxic) T cells, which both of their activation occurs through the detection of virus-derived major histocompatibility complex (MHC, MHC-II for $CD4^+$ and MHC-I for $CD8^+$)-associated peptides on antigen-presenting cells, like dendritic cells and macrophages from innate immunity and B cells from adaptive humoral immunity [132, 135, 136]. Activated $CD4^+$ cells would differentiate into subtypes including T-helper cells (Th1,2 &17), regulatory T cells (Treg) and etc. Th1 cells produce anti-viral cytokines like IFN-γ and IL-2 to regulate cellular immunity of macrophages and $CD8^+$ cells; while Th2 cells secrete IL-4, IL-5, and IL-13 for the regulation of humoral responses from B cells [132, 135, 136]. Treg and Th17 cells work reciprocally, in which Treg suppresses the immunity from Th cells and $CD8^+$ cells for immunosuppression, while Th17 controls the function of Treg and produces IL-6 to promote T cell responses [132, 136]. The activated $CD8^+$ cells differentiate into cytotoxic T lymphocytes (CTLs) under the helps from IFNs and cytokines, which can induce apoptosis of IAV infected host cell and prevent virus replication through the production of cytokines and cytotoxic granules like perforin and granzymes that can bind to infected cells. Theses IAV-specific CTLs can also persist in the system after infection as memory cells to defend secondary infections [135]. For the humoral response, the activation of naïve B cells requires a T-cell dependent recognition of viral antigens, which leads to B cell differentiation into short-lived plasmablasts for initial rapid generation of IAV-specific

antibodies (starts with IgM, then IgG or IgA depends on the location) for the immediate defense against IAV [136-138]. Some activated B cells differentiate into long-lived plasma cells for long-term production of stronger antibodies (IgG and IgA), and some mature into memory B cells for the protection against secondary infection [137]. Viral HA and NA proteins are the major targets of these antibodies, which can cause IAV neutralization by blocking the functions of HA (for viral entry) and NA (for viral release), and some of the antibodies can also direct antibody-dependent cell cytotoxicity and Fc receptor-mediated phagocytosis of infected cells [135-137]. During IAV infection in mice and human, the 1st wave of antibody production starts around 3 days post infection, and the peak of antibody production is around 7-10 days after infection [135, 137].

As for the pathogenesis from IAV infection, apart from those tissue and cell damages from the infected sites, the pro-inflammatory cytokines and chemokines, like IFNs, IL-1β, IL6, IL-12 and such, induced from the immune responses after acute IAV infection are sometimes overreactive and dysregulated (known as 'cytokine storm'), which also contributes to pneumonia, lung damage and even death [139-141]. The damaged respiratory space is characterized with death of pulmonary epithelial cells, infiltration of immune cells, edema, and alveolar hemorrhage, which makes it more vulnerable to secondary bacterial and viral infections [142, 143]. On the contrary, as mentioned earlier in this chapter, the adequate inflammatory responses are actually in favor of IAV clearance, which emphases their dual functions. Therefore, the proper balance of inflammatory responses needs to be achieved in order to defend IAV but restrain the damage at the same time, in which anti-inflammatory responses and immunomodulatory therapies would be beneficial[142, 143]. In addition, the active repair of damaged tissue mediated through the interaction between innate immunity and the pulmonary

stem cells (via factors like IL-10 and IL-22) is also necessary for re-establishment of lung homeostasis [144-146].

1.4.3 Influenza A in female reproduction

Epidemiological studies and murine models both confirmed the sex differences in responding to IAV infections, which females during the reproductive age (15-49 years for human) generally suffer more adverse outcomes with higher rate of morbidity and mortality caused by inflammatory responses upon IAV infection [147-149]. Apart from the special condition of pregnancy, differences in sexual hormones and sex chromosome-linked genes are major contributors to the sex-dependent differential outcomes from IAV infection [148, 149].

The changes of circulating E2 and P4 levels during the reproductive cycles of non-pregnant females are the main sexual factors regulating immune responses. The function of E2 in regulating immune responses is complicated: in one aspect, treatment of E2 on IAV-infected female mice can stimulate the recruitment of immune cell via ERs and the secretion of certain cytokines to help with the clearance of IAV; in another aspect, the E2 treatment can also suppress the inflammatory responses by reducing the level of inflammatory cytokines like IFNγ and TNFα [148-154]. Overall, the E2 treatment on female mice showed a protective effect after IAV infection, while the other weak estrogen hormone mainly produced during pregnancy, estriol (E3), works solely as immunosuppressor by reducing both immune cell recruitment and pro-inflammatory responses to improve the outcomes from severe IAV infection [155]. The effect of P4 on the outcomes from IAV infection is controversial in different mouse strains: P4 treatment in infected females from C57BL/6 strain can improve infection outcomes by reducing inflammation and promoting pulmonary repair via TGF-β, IL-6, IL-22 and Th17 cells, while the treatment in ovariectomized CD-1 mice showed slightly worse outcomes than vehicle control

[153, 154, 156, 157]. Also, in females challenging with a sequential infection with a different strain of IAV from the primary infection, those underwent P4 or P4-based contraceptive treatment were more susceptible compared to placebo-treated females, which indicates a long-term adverse effect of P4 on IAV infection [157].

Another determinant factor is genetic difference on sex chromosomes. Even though one study compared gonadectomized male and female C57BL/6 mice upon IAV infection with no difference on overall infection outcomes [158], some recent studies in human and mice from different genetic backgrounds suggest that some immunity-associated genes are on sex chromosomes and can result in different susceptivity in IAV infection [159-161].

The World Health Organization has identified pregnancy as a risk factor for severe outcomes from IAV infection, which can increase the hospitalization rate up to 7-10 times higher than non-pregnant women, accompanied with higher chances of developing adverse pregnancy outcomes like pregnancy loss [162-168]. Many studies using mouse models recapitalized the same results when infecting the pregnant females with H1N1 IAV during mid-late gestation [169-175]. Compared to the non-pregnant females, pregnant BALB/c mice from several studies showed increased production of pro-inflammatory cytokines and chemokines, as well as increased infiltration of macrophages and neutrophils into the pulmonary area after IAV infection, which both exacerbate the pathogenesis and hamper the pulmonary repair [169, 170, 173]. However, one study using C57BL/6 mice, which is less sensitive to IAV infection compared to BALB/c mice, indicated adverse pregnancy outcomes but with comparable immune responses to IAV with even slightly reduced pulmonary inflammation in the pregnant females [176]. A recent study also confirms the genetic background of mice, especially the mating background, can alter the immune responses to IAV infection, which BALB/c-mated allogenic

pregnant C57BL/6 females showed increased morbidity and mortality compared to syngeneic pregnant C57BL/6 females, and recapitalized the reduction of inflammatory cytokines and anti-viral immune responses in allogenic pregnant C57BL/6 females [177]. The strain of the IAV may also affect the immune responses in pregnant mice, in which H3N2 IAV infection in pregnant C57BL/6 females can drive systemic inflammation response and cause potential developmental defects in fetus [175, 178]. When compared to non-infected pregnant females, IAV infection during mid-gestation in pregnant BALB/c mice showed shorter gestational period and increased adverse pregnancy outcomes via disruptions in pregnancy-supporting hormone levels and placental structure [171, 174]. The above mouse studies are all focusing on the IAV infection during mid-late gestation, while the current knowledge gap is how infection during early pregnancy, especially the critical embryo implantation time, can have effects on pregnancy outcomes. Some epidemiological studies indicate infection during first trimester is associated with congenital abnormalities in fetus like neural tube defects and cleft lip, while we cannot rule out other possible pregnancy defects like miscarriage, which is hard to be detected from epidemiology and currently has not been dressed in mouse models [162, 179, 180].

1.5 Hypothesis and specific aims

The female reproduction is a serial of delicate and complex activities that starts from the sexual development in utero, and then upon puberty, the female reproductive system undergoes regular reproductive cycles for the production of eggs. A successful fertilization of the egg marked the initiation of pregnancy, which requires even more sophisticated regulations to ensure the healthy development of the embryo to term. A lot of endogenous factors and exogenous factors can have detrimental effects on female reproduction, especially for the circularity of

female cycles and during the critical early pregnancy time, which accounts for about 80% of all cases of pregnancy loss [181].

Our long-term goal is to identify and study the molecular mechanisms of those determinant factors, from endogenous and exogenous sources, that can affect the female reproduction, and provide solutions to these factors-related impairments in female fertility. *My central hypothesis* is that endogenous factors, such as the ion channels on lysosomes and on plasma membrane of LE, and exogenous factors, like influenza A infection, can affect female reproduction during early pregnancy and the female reproductive cycle (Fig. 1.16).

Aim 1. Test the hypothesis that the impaired corpus luteum (CL) function in *Mcoln1*$^{-/-}$ mice can be partially rescued in *Atp6v0d2*$^{-/-}$*Mcoln1*$^{-/-}$ females. (Chapter 2)

This aim is based on the findings that both *Atp6v0d2* and *Mcoln1* genes encode lysosomal ion channels (V-ATPase and TRPML1 respectively) that work in the opposite directions to maintain the lysosomal transmembrane balance. In female reproduction, both genes are upregulated on LE during the embryo implantation time, and *Mcoln1*$^{-/-}$ female mice showed impaired fertility due to impaired CL function related to lysosomal defects. The double deletion of both *Atp6v0d2* and *Mcoln1* in mice (*Atp6v0d2*$^{-/-}$*Mcoln1*$^{-/-}$) can potentially restore the lysosomal balance and therefore rescue the phenotypes in the CL of *Mcoln1*$^{-/-}$ females. Overall female fertility in *Atp6v0d2*$^{-/-}$*Mcoln1*$^{-/-}$ mice and the detailed molecular changes in the CL will be compared and analyzed with *Mcoln1*$^{-/-}$ and control females.

Aim 2. Test the hypothesis that the progesterone (P4) signaling regulates uterine fluid absorption during early pregnancy via uterine luminal epithelium (LE). (Chapter 3)

It is based on the preliminary data that P4 can induce uterine fluid absorption in ovariectomized mice, as well as the absorption is mainly passing through the LE. The potential

passages of the uterine fluid are bulk absorption through the membrane channels and endocytosis on apical side of LE. A small-sized fluorescent dye (Alexa Fluor™ 488 hydrazide) that can pass through the membrane channels will be injected into the uterine lumen during the early pregnancy time to indicate the uterine fluid passage. Mouse models with P4 deficiency combined with P4 and PR antagonist treatment will be employed.

Aim 3. Test the hypothesis that influenza A (IAV) infection affects estrous cycle in C57BL/6 female mice. (Chapter 4)

It is based on our pilot experiment that mouse-adapted H3N2 IAV infection in C57BL/6 females showed an arrest in the diestrus stage of estrous cycle, as well as preliminary studies indicated that COVID-19 vaccine can temporarily increase the menstrual cycle length in women. Comparison between IAV-infected and non-infected C57BL/6 female littermates will be analyzed in the histology and immune responses of lung, ovary, and uterus.

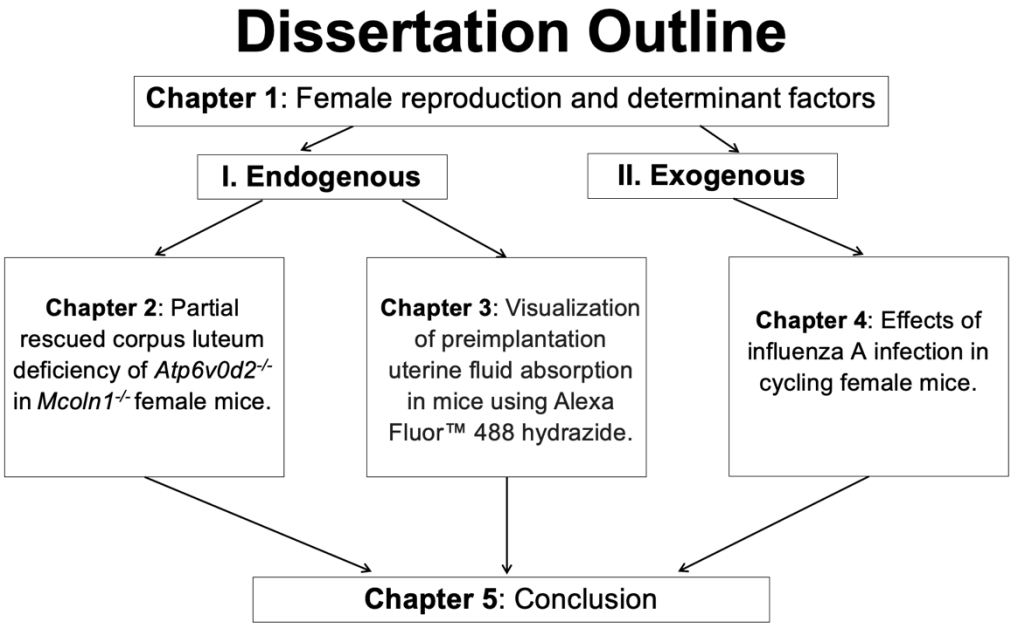

Figure 1.16. Outline of my dissertation.

CHAPTER 2

ATP6V0D2 DEFICIENCY PARTIALLY RESTORES DEFECTS IN *MCOLN1* DEFICIENT CORPUS LUTEUM[1]

[1] Li, Y., El Zowalaty, A.E., Hancock, J.M., Wang, Z., Martin, T.E., Zhan, T., Wang, Y., Andersen, C.L., Viswanathan, S., Bromfield, J., Atluri, V.A., Brismer, H.N., Kallish, K.R., and Ye, X. To be submitted to *Biology of Reproduction*.

2.1 Abstract

ATP6V0d2 is a subunit in V-ATPase that pumps H^+ into lysosomes. TRPML1 (*MCOLN1*/*Mcoln1*) pumps cations out of lysosomes. *Mcoln1*$^{-/-}$ mice recapitulate lysosomal storage disorder MLIV phenotypes. We previously demonstrated that *Mcoln1*$^{-/-}$ females had reduced fertility at 2 months old (2M) and quickly became infertile at 5M with degenerating corpus luteum (CL) and progesterone (P4) deficiency. We hypothesized that *Atp6v0d2* deficiency could cancel out *Mcoln1* deficiency to restore CL functions in *Atp6v0d2*$^{-/-}$*Mcoln1*$^{-/-}$ mice. Fertility test of *Atp6v0d2*$^{-/-}$*Mcoln1*$^{-/-}$ females (2M-7M) revealed normal mating activity but reduced fertility compared to control, yet ~25% of them remained fertile at 5M-7M but with dystocia. We analyzed a subset of 5M old mice in the fertility test on day 3.5 post-coitum (D3.5). Among the 11 *Atp6v0d2*$^{-/-}$*Mcoln1*$^{-/-}$ mice analyzed, 3 (27%) had normal P4 levels and CLs, while 8 had P4 deficiency (2 infertile (18%) & 6 once fertile (55%)). In contrast to *Mcoln1*$^{-/-}$ CLs that had extensive cell debris most likely due to necrosis, *Atp6v0d2*$^{-/-}$*Mcoln1*$^{-/-}$ CLs had reduced cell debris and increased cell survival regardless of P4 levels. However, similar to *Mcoln1*$^{-/-}$ CLs, P4-deficient *Atp6v0d2*$^{-/-}$*Mcoln1*$^{-/-}$ CLs had impaired luteal cell differentiation, enlarged lipid droplets, disrupted expression of endothelial basal lamina marker Col IV, and reduced expression of mitochondrial marker HSP60 and steroidogenesis rate-limiting protein StAR, indicating that additional *Atp6v0d2* deficiency compensates for *Mcoln1* deficiency-induced cell death but is insufficient to restore luteal cell differentiation and P4 steroidogenesis in the P4-deficient *Atp6v0d2*$^{-/-}$*Mcoln1*$^{-/-}$ CLs. This study demonstrates individual variations in coordination between ATP6V0d2 and TRPML1 in the corpus luteum.

2.2 Introduction

The lysosome is the most acidic membrane-bound intracellular organelle [41, 182, 183]. The acidity is specified by pH (potential of hydrogen) scale. The pH of the lysosomal lumen is ~4.6 while the common intracellular pH is ~7.0-7.4. Lysosomal acidity is critical for the activities of lysosomal enzymes to degrade macromolecules and for maintaining normal cellular homeostasis. The lysosomal lumen has higher $[H^+]$, $[Ca^{2+}]$, $[Na^+]$, and $[Cl^-]$, but lower $[K^+]$ than that in the cytosol. The ~500-fold $[H^+]$ gradient across the lysosomal membrane is established and maintained by the vacuolar-type H^+-ATPase (V-ATPase), which pumps H^+ into the lysosomal lumen [41, 182, 183]. Lysosomal counter ion channels and transporters dissipate the transmembrane voltage built up by V-ATPase and maintain lysosomal ionic homeostasis [85]. Among them are transient receptor potential cation channels of the mucolipin subfamily 1–3 (TRPML1-3, the primary lysosomal Ca^{2+} release channels), Na^+-selective two-pore channels 1 and 2 (TPC1-2), and various channels/transporters for conducting Cl^-, K^+, and catabolites, etc. [85]. The lysosome has essential functions in digestion, signaling, and trafficking, etc., and disrupted lysosomal functions are associated with >50 rare inherited metabolic disorders in humans, collectively termed lysosomal storage diseases [41, 60, 85, 182, 183].

V-ATPase has a transmembrane integral V0 domain for proton (H^+) translocation and a cytoplasmic peripheral V1 domain for ATP hydrolysis [40, 184]. The V0 domain includes subunits a, c, c″, d, e, which are encoded by *ATP6V0* genes, and accessory subunits Ac45 (*ATP6VAP1*) and M8-9 (*ATP6VAP2*) [185]. The V1 domain contains subunits A-H, which are encoded by *ATP6V1* genes. The d subunit in V0 domain connects V0 and V1 domains and forms a rotor with the D and F subunits in V1 domain. The rotation of the rotor is powered by ATP hydrolysis [184]. The d subunit is encoded by two genes, the more ubiquitously expressed

Atp6v0d1 and the more tissue-specific *Atp6v0d2* [40]. The V-ATPase pumps H^+ from the cytoplasmic compartment to the opposite side of the membrane where the V-ATPase is localized, which can be plasma membrane or the membrane of intracellular organelles, to acidify the extracellular environment or the lumen of intracellular organelles, respectively [186].

TRPML1, encoded by mucolipin 1 (*MCOLN1*, *Mcoln1*), is a counter ion channel localized in the membrane of late endosomes and lysosomes. It mediates the release of Ca^{2+}, Na^+, Fe^{2+}, and potentially other cations from the lysosomal lumen to cytosol to dissipate the transmembrane voltage built up by V-ATPase, thus indirectly regulating lysosomal lumen acidity [60, 85, 187]. TRPML1 is also critical for vesicular trafficking, lipid homeostasis, autophagy, plasma membrane repair, signaling in cellular adaptation to nutrient availability, etc. [60, 187]. TRPML1 deficiency has been associated with mucolipidosis type IV (MLIV) in both humans and mice [85, 188-191]. MLIV is a type of lysosomal storage disorders, which are inherited metabolic disorders resulting from mutations in lysosomal genes [60, 85, 187]. *Mcoln1*$^{-/-}$ mice, which are deficient of TRPML1, can recapitulate phenotypes associated with MLIV, such as neurodegeneration, ophthalmologic abnormalities, and muscular dystrophy [189, 191].

Our research has been focused on female reproduction, especially uterine receptivity for embryo implantation [192, 193]. Embryo implantation initiates when a competitive embryo attaches to the uterine luminal epithelium (LE), which occurs ~day 4 post-coitum (D4.0) in mice. Our microarray analysis (GEO number: GSE44451) of D3.5 and D4.5 mouse LE revealed *Atp6v0d2*, a previously uncharacterized gene in the LE, to be one of the most upregulated genes upon embryo implantation initiation [37]. This observation led us to the novel finding of uterine epithelial acidification, detected by LysoSensor Green DND-189, upon embryo implantation initiation in mice [42]. Mice deficient of *Atp6v0d2* (*Atp6v0d2*$^{-/-}$) have impaired osteoclast fusion

and increased bone formation [194]. *Atp6v0d2*$^{-/-}$ female mice have significantly reduced embryo implantation rate and marginally reduced delivery rate from the first mating only, and have normal fertility afterwards [42]. The inhibitory effect of bafilomycin (a V-ATPase inhibitor) on uterine receptivity coupled with LE acidification upon embryo implantation initiation, established an important role of V-ATPase in uterine receptivity for embryo implantation [42]. The function of V-ATPase in acidifying lysosome lumen requires the functions of counter ion channels. Prior to the recent finding that LRRC8 family proteins (components for the volume-regulated anion channels, or VRACs), which have known functions on the plasma membrane, also act within lysosomes [195], *Mcoln1* had the highest mRNA expression level in the peri-implantation LE (Fig. 2.1A, GEO number: GSE44451 [37]) among the known/putative lysosomal counter ion channels/transporters that were summarized recently [182]. In addition, the essential role of TRPML1/*Mcoln1* in lysosomal functions has been established in both humans and mice [85, 188-191]. Despite an earlier report indicating that *Mcoln1*$^{-/-}$ female mice were fertile [191], we still studied female fertility in the *Mcoln1*$^{-/-}$ mice. Our continuous fertility study demonstrated that *Mcoln1*$^{-/-}$ female mice had normal mating activities but reduced fertility at 2 months old (2M), and they quickly became infertile at 5M with progesterone (P4) deficiency, which was caused by defective corpus luteum integrity and function [196].

Lysosomal function, such as H^+ pumping by V-ATPase, requires the maintenance of lysosomal lumen ionic homeostasis and membrane potential ($\Delta\psi = V_{cytosol} - V_{lumen}$; $V_{lumen} = 0$ mV) [85]. Acidification of lysosomal lumen by V-ATPase, which is important for most lysosomal hydrolases to be functional, depends on the lysosomal $\Delta\psi$ (~−20 to −40 mV), which would require balanced efflux of countercations and/or influx of counteranions to compensate for the influx of H^+ by V-ATPase. Since TRPML1 is an important counter ion channel to efflux cations

from the lysosome, and ATP6V0d2 is one of the two V0d subunits for V-ATPase, we hypothesized that additional deletion of *Atp6v0d2* in the *Mcoln1*$^{-/-}$ female mice would alleviate the defects in the *Mcoln1*$^{-/-}$ CLs [196]. We tested this hypothesis in the *Atp6v0d2*$^{-/-}$*Mcoln1*$^{-/-}$ double knockout mice.

2.3 Materials and Methods.

Animals and genotyping. *Atp6v0d2*$^{-/-}$*Mcoln1*$^{-/-}$ mice were generated by breeding *Atp6v0d2*$^{+/-}$ mice [42], which were derived from Dr. Yongwon Choi's colony at the University of Pennsylvania [194], with *Mcoln1*$^{+/-}$ mice [196], which were purchased from The Jackson Laboratory (B6.Cg-Mcoln1tm1Sasl/J Stock No: 027110 [191]). Mice with genotypes of *Atp6v0d2*$^{+/+}$*Mcoln1*$^{+/+}$ (wild type), *Atp6v0d2*$^{+/-}$*Mcoln1*$^{+/+}$, *Atp6v0d2*$^{+/+}$*Mcoln1*$^{+/-}$, or *Atp6v0d2*$^{+/-}$ *Mcoln1*$^{+/-}$ were used as control. PCR was used for genotyping as described previously [42, 196]. All mice were housed in polypropylene cages on a 12h light/dark cycle (6:00-18:00) at 23 ± 1 °C with 30-50% relative humidity. All mice had free access to regular food and water. All methods used in this study were approved by the University of Georgia Institutional Animal Care and Use Committee (IACUC) and conform to National Institutes of Health guidelines and federal law.

Superovulation and real-time PCR. Wild type mice at 21 days old (N=3) were superovulated by i.p. injection with 5 IU/mouse PMSG followed with 5 IU/mouse of hCG 48 h after PMSG injection [21]. Both ovaries were dissected 72 h after hCG injection for CL isolation using a 25G needle under a stereoscope. The isolated CL fraction and the remaining ovarian tissues (-CL) were flash-frozen. Total RNAs were extracted using TRIzol (Life Technologies, 15596018) and cDNA was prepared using Superscript III First-Strand Synthesis kit (Invitrogen, 18080-400) with random primers. Real-time PCR was performed in 384-well plates using

PowerSYBR Green PCR Master Mix (Thermo Fisher, 4367659) on CFX384 TouchReal-Time PCR Detection System (Bio-Rad). The primer pairs used: *Atp6v0d2* forward primer, 5'-AGTTGCTATCCAGGACTCGG-3' and reverse primer 5'-CATTAGCCAGGAAGTTGCCATAG-3'; *Mcoln1* forward primer 5'-ATCTTGGTGGTCACTGTGC-3' and reverse primer 5'-AGTCCTCACTGGGGATGTCA-3'; *StAR* forward primer 5-CAGCTGCAGGACTCAGGAC-3' and reverse primer 5-ACGTCGAACTTGACCCATCC-3'; *Rsp11* forward primer 5'-CGTGACGAAGATGAAGATGC-3' and reverse primer 5'- GCACATTGAATCGCACAGTC-3'; and *Tuba1b* forward primer 5' TGCCTTTGTGCACTGGTATG-3' and reverse primer 5'-CTGGAGCAGTTTGACGACAC-3'.

Mating and fertility test. *Mcoln1*$^{-/-}$ female mice quickly became infertile at 5M [196]. For comparison, *Atp6v0d2*$^{-/-}$*Mcoln1*$^{-/-}$ female mice were tracked for mating and fertility from 2M to up to 7M. The reduction of mice in the cohort towards the end of tracking was mainly for two reasons: 1) randomly selected for serum collection at 5M, and 2) sacrificed at various ages following COVID-19 lockdown policy. Control female mice (N=29) and *Atp6v0d2*$^{-/-}$*Mcoln1*$^{-/-}$ female mice (N=40) at 2 months old (2M) were cohabitated with the same wild-type stud males. Each stud male was housed with two *Atp6v0d2*$^{-/-}$*Mcoln1*$^{-/-}$ females and two control females. Each female was checked every morning for a vaginal plug, which served as an indicator of mating the previous night. The day of vaginal plug detection was designated as day 0.5 post-coitum (D0.5, the mating night as D0). The plugged females were weighed every 3 days from D0.5 to D18.5. They continued cohabitation with their respective stud males and being checked for a vaginal plug every morning until steady weight gain was observed to confirm pregnancy. Each confirmed pregnant female was then housed separately and its body weight was monitored till

the delivery. Some females were plugged multiple times before a pregnancy could be confirmed by body weight gain; some pregnant females would stop gaining weight and end up losing the pregnancy; some females were plugged multiple times but never showed body weight gain associated with pregnancy and they were infertile. Plugging rate (the percentage of mice in each group with the presence of a vaginal plug), plugging latency (the time from cohabitation to the detection of the first vaginal plug), post-mating body weight gain, gestational period (the time from mating to delivery), litter size, and pregnancy rate were recorded. We defined the pregnancy age based on the mating age. For example, if a pregnancy was derived from a mating (indicated by the presence of a vaginal plug) before 3M old, the pregnancy age was 2M; likewise, the pregnancy age of 5M was from mating after 5M old but before 6M old; and the pregnancy age of 6-7M was from mating after 6M old but before 8M old. The term pregnancy rates were calculated as the percentage of mated females at the same mating age (2M, 5M, or 6-7M) that had confirmed pregnancy, indicated by steadily increased body weight after 6 days post-coitum.

Serum P4 and E2 measurement. At 5M, day 3.5 post-coitum (D3.5) control mice (N=4) and *Atp6v0d2*$^{-/-}$*Mcoln1*$^{-/-}$ mice (N=11) in the fertility test were randomly selected, with the later including 9 mice that had delivered at least one litter and 2 mice that had mating activities indicated by multiple vaginal plugs but never delivered pups or shown body weight gain associated with pregnancy. Between 11:00 h and 12:00 h, the D3.5 mice were anesthetized via isoflurane inhalation for blood collection via orbital sinus. Serum was collected after blood clotting at room temperature for 45 minutes and stored at -80°C. One ovary was fixed in 10% formalin solution and the other ovary was snap-frozen. Serum progesterone (P4) and 17β-

estradiol (E2) were measured in the Ligand Assay and Analysis Core of the Center for Research in Reproduction at the University of Virginia (Charlottesville, Virginia).

Ovary histology. The fixed ovaries were kept in the fixative for 24 hours and then transferred to 70% ethanol. They were processed for paraffin embedding as previously described [196] [21] [21, 197-199]. Paraffin sections (5 μm) through the widest middle portion of the ovaries were collected, processed, and stained with hematoxylin and eosin. Follicles and CLs were analyzed as we previously described [21, 199, 200].

Immunofluorescence. Immunofluorescence was used to detect collagen IV (Col IV) and heat shock protein 60 (HSP60) in the 5 months old D3.5 control and *Atp6v0d2*$^{-/-}$*Mcoln1*$^{-/-}$ frozen ovarian sections (10 μm) as previously described [21]. Briefly, frozen sections were fixed in 4% paraformaldehyde and subjected to antigen retrieval in 0.01 M sodium citrate (pH 6.0) at 95°C for 20 min. Sections were washed with 1xPBS followed by membrane permeabilization with 0.15% Triton X-100. The slides were then washed and blocked with 10% goat serum for 1 h at room temperature and incubated with anti-StAR (1:500, Abcam, ab96637), anti-Col IV (1:200, Abcam, ab19808), or anti-HSP60 (1:500, Cell Signaling Technology, mAb #12165) respectively for overnight at 4°C. The following day, the sections were washed in 1xPBS and incubated with secondary Alexa Fluor-conjugated goat anti-rabbit IgG antibody (1:200, Invitrogen, A11036 for Col IV, A11034 for StAR and HSP60) for 1 h. The sections were counterstained and mounted in DAPI (4',6'-diamino-2-phenylindole)-containing Vectashield (Vector Laboratories, Burlingame, CA, USA).

Lipid droplet staining. Frozen ovarian sections (10 μm) were fixed in 4% paraformaldehyde at room temperature for 20 minutes, washed twice in 1X PBS, then covered

with 1.6 μg/ml Nile red (N3013, Sigma-Aldrich) in 1X PBS at room temperature for 15 minutes. Sections were then washed in 1X PBS and counterstained with DAPI [21, 196].

Statistical Analysis. Data are presented as mean ± SD where applicable. Wilcoxon Rank Sum test was used for plugging latency. For parameters with percentage, two-tailed Fisher's exact test was used. Two-tailed unequal variance student t-test was used for the other quantitative data. Significance level is set at $P<0.05$.

2.4 Results.

2.4.1 Expression of *Atp6v0d2* and *Mcoln1* in the ovary

We previously demonstrated that TRPML1 was detected in the CL and *Mcoln1*$^{-/-}$ mice had premature infertility associated with degenerative luteal cells in the CL and P4 deficiency [196]. The first experiment we intended to perform was co-immunolocalization of ATP6V0d2 and TRPML1 in the luteal cells. However, we failed to obtain suitable antibodies. We eventually employed realtime PCR to detect *Atp6v0d2* and *Mcoln1* in the CLs surgically isolated from superovulated ovaries, with StAR (steroidogenic acute regulatory protein) as a marker for CL as StAR/*StAR* is dominantly expressed in the CL [21, 196]. Since the surgically isolated CLs were expected to have non-CL ovarian tissues and the remaining ovarian tissues, designated as "-CL", might include CLs as well, we did not expect this procedure as a clean approach. Overall, *StAR* expression levels in the CL fraction were 1.5~2.9 folds of the "-CL" fraction. Regardless, both *Atp6v0d2* and *Mcoln1* were detectable in the CL and the "-CL" fractions albeit the mRNA levels were much lower than *StAR* levels (Fig. 2.1B).

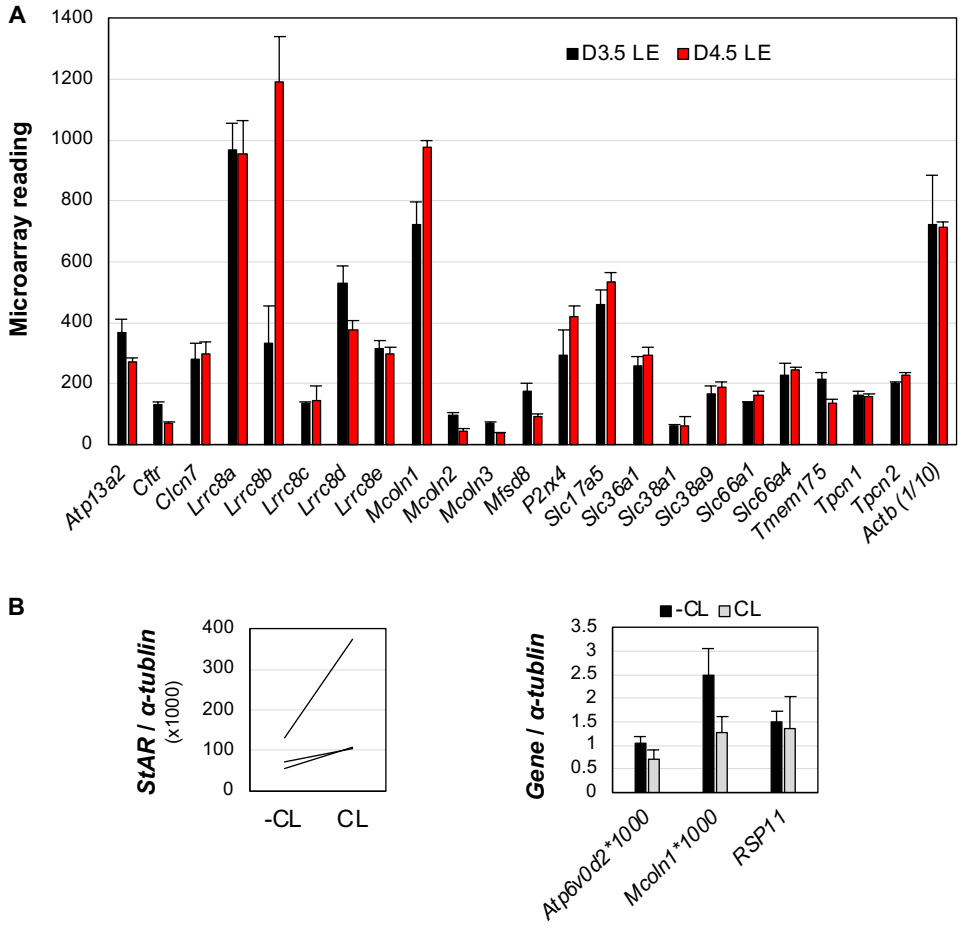

Figure 2.1. Microarray reading of lysosomal counterion channels in day 3.5 post-coitum (D3.5) and D4.5 wild type mouse uterine luminal epithelium (LE) and detection of *Atp6v0d2* and *Mcoln1* in superovulated mouse ovaries. A. Microarray readings for lysosomal counterion channels. N=3/group. *Actb* as a loading control, 1/10 of the reading were presented. B. Real-time PCR in corpus luteum (CL) and -CL tissue fractions surgically dissected from superovulated ovaries. N=3. Data was normalized with α-tubulin and RSP11 as a second loading control. The normalized readings of *StAR*, *Atp6v0d2*, and *Mcoln1* were multiplied by 1000 to be plotted on the same figures and for straightforward comparisons. *Atp13a2*: ATPase cation transporting 13A2; *Cftr*: cystic fibrosis transmembrane conductance regulator; *Clcn7*: chloride channel, voltage-sensitive 7; *Lrrc8a-e*: leucine rich

Figure 2.1. (continued) repeat containing 8A VRAC subunit A-E; *Mcoln1-3*: mucolipin TRP cation channel 1-3; *Mfsd8*: major facilitator superfamily domain containing 8; *P2rx4*: purinergic receptor P2X, ligand-gated ion channel 4; *Slc17a5, Slc36a1, Slc38a1, Slc38a9, Slc66a1, Slc66a4*: solute carrier family 17 member 5, family 36 member 1, family 38 member 1, family 38 member 9, family 66 member 1, family 66 member 4; *Tmem175*: transmembrane protein 175; *Tpcn1-2*: two pore segment channel 1-2; *Actb*: actin, beta; *Atp6v0d2*: ATPase, H^+ transporting, lysosomal V0 subunit D2; *RSP11*: ribosomal protein S11.

2.4.2 Mating and Fertility of *Atp6v0d2*$^{-/-}$*Mcoln1*$^{-/-}$ females

We generated *Atp6v0d2*$^{-/-}$*Mcoln1*$^{-/-}$ double knockout mice from our *Atp6v0d2*$^{+/-}$ mice [42] and *Mcoln1*$^{+/-}$ mice [196]. In the female fertility study, virgin control female mice (N=29) and *Atp6v0d2*$^{-/-}$*Mcoln1*$^{-/-}$ female mice (N=40) at 2 months (2M) old were cohabitated with the same wild-type stud males and checked for a vaginal plug every morning. They were all plugged within 17 days of co-habitation. The overall first plugging latencies were comparable between control and *Atp6v0d2*$^{-/-}$*Mcoln1*$^{-/-}$ female mice (Fig. 2.2A). The control mice had pregnancy rates of 100% (29/29), 94.1% (16/17), and 100% (9/9) at 2M, 5M and 6-7M, respectively; and those for *Atp6v0d2*$^{-/-}$*Mcoln1*$^{-/-}$ mice were 72.5% (29/40), 27.8% (5/18), and 23.1% (3/13), respectively (Fig. 2.2B). The majority of the pregnancies at 2M were from the 1st mating (23/29 in control mice and 22/29 in *Atp6v0d2*$^{-/-}$*Mcoln1*$^{-/-}$ mice), the remaining pregnancies were developed after multiple plugs were detected. For those 11 *Atp6v0d2*$^{-/-}$*Mcoln1*$^{-/-}$ mice that did not yield a pregnancy at 2M after 3+ vaginal plugs detected in each, they continued mating activities throughout the duration of fertility test, and 2 of them eventually produced a litter after 4M of

age, and the third one produced 1 litter after 4M of age with another litter after 5M of age. Therefore, 20% (8/40) of *Atp6v0d2*$^{-/-}$*Mcoln1*$^{-/-}$ mice were born infertile, and this infertility rate is significantly higher than the control (0/29=0%, P= 0.0172, two-tail Fisher's exact test).

The gestation periods were comparable between the two groups at all three time points, although those with dystocia took extra 2 or more days to finish delivery or were euthanized by the 3rd day of delivery. The litter sizes were smaller in *Atp6v0d2*$^{-/-}$*Mcoln1*$^{-/-}$ from 2M and 5M compared to control (6.5±1.9 vs. 8.0±2.9 at 2M; 5.6±1.9 vs. 8.3±2.5 at 5M). At 6-7M, all the pups from the pregnant *Atp6v0d2*$^{-/-}$*Mcoln1*$^{-/-}$ mice were born dead due to dystocia (Fig. 2.2C). Dystocia was not observed in either group at 2M. It was observed in ~10% of term pregnant control mice at 5M and 6-7M. For term pregnant *Atp6v0d2*$^{-/-}$*Mcoln1*$^{-/-}$ mice, 60% and 100% of them had dystocia at 5M and 6-7M, respectively (Fig. 2.2C).

There was an age-related differential body weight change during pregnancy. For all three pregnancy ages analyzed (2M, 5M, and 6-7M), the *Atp6v0d2*$^{-/-}$*Mcoln1*$^{-/-}$ mice had significantly lower body weight than their age-matched controls (Fig. 2.2D-2F). However, while this trend maintained during the rest of the pregnancies for *Atp6v0d2*$^{-/-}$*Mcoln1*$^{-/-}$ mice at pregnancy ages 5M and 6-7M (Fig. 2.2E, 2.2F), the pregnant *Atp6v0d2*$^{-/-}$*Mcoln1*$^{-/-}$ mice at 2M pregnancy age reached comparable body weights as the age-matched controls towards the late stage of pregnancy (Fig. 2.2D), this reflected significantly increased percentages of body weight gain at 2M pregnancy age in the *Atp6v0d2*$^{-/-}$*Mcoln1*$^{-/-}$ group compared to the control (Fig. 2.2D and data not shown). The body weights of *Atp6v0d2*$^{-/-}$*Mcoln1*$^{-/-}$ mice on D0.5 at 2M, 5M, and 6-7M were 20.0g ± 1.4g (vs. 22.0g ± 2.1g in control), 23.7g ± 1.0g (vs. 27.7±2.6 in control), and 23.0g ± 1.4g (vs. 27.8g ± 2.3g in control), respectively, all significantly lower that their age-matched controls (Fig. 2.2D-2F).

A similar mating study in *Mcoln1*$^{-/-}$ mice from 2M old showed that *Mcoln1*$^{-/-}$ female mice quickly became infertile at 5M (0/7) [196]. *Atp6v0d2*$^{-/-}$*Mcoln1*$^{-/-}$ mice had a pregnancy rate of 27.8% (5/18) at 5M and 23.1% (3/13) at 6-7M, indicating that there was a partial rescue of fertility after 5M old in the *Atp6v0d2*$^{-/-}$*Mcoln1*$^{-/-}$ mice compared to *Mcoln1*$^{-/-}$ mice. However, because of the small sample size and low rescuing rate, no statistically significant difference was achieved (0/7 vs. 5/18 at 5M, P=0.2743, two-tail Fisher's exact test). We have not examined the fertility of virgin *Mcoln1*$^{-/-}$ and *Atp6v0d2*$^{-/-}$*Mcoln1*$^{-/-}$ mice at 5M old and beyond.

2.4.3 General health of *Atp6v0d2*$^{-/-}$*Mcoln1*$^{-/-}$ females

We did not measure the body weight during postnatal development and did not notice any obvious abnormal activities, including mating activity, in the *Atp6v0d2*$^{-/-}$*Mcoln1*$^{-/-}$ female mice. However, based on the body weight of the mated females at D0.5, which should have comparable body weight as non-pregnant mice because significant pregnancy-associated body weight gain does not start before embryo implantation (~D4.0 in mice) (Fig. 2.2D-2F) [21], the *Atp6v0d2*$^{-/-}$*Mcoln1*$^{-/-}$ female mice had lower body weight than their age-matched control female mice at all the three ages examined (Fig. 2.2D-2F). Rigid hind legs started to show up in a few mice at ~6M old, same as that reported in *Mcoln1*$^{-/-}$ mice [191]. There were 13 *Atp6v0d2*$^{-/-}$ *Mcoln1*$^{-/-}$ females remaining in the 6-7M group of fertility test (Fig. 2.2B, 2.2C). They were maintained till 8M old because mating during 7M old could yield pregnancy at 8M old. The three pregnant mice were euthanized due to dystocia. Among the remaining 10 *Atp6v0d2*$^{-/-}$ *Mcoln1*$^{-/-}$ females at the end of the fertility test (8M), half of them had paralyzed hind legs and the other half could still move around, all of them were skinny with little fat tissues, all of them had abnormal bladders with the most obvious phenotype being enlarged bladders filled with urine, and three of them had whitish stomachs most likely from calcification (data not shown).

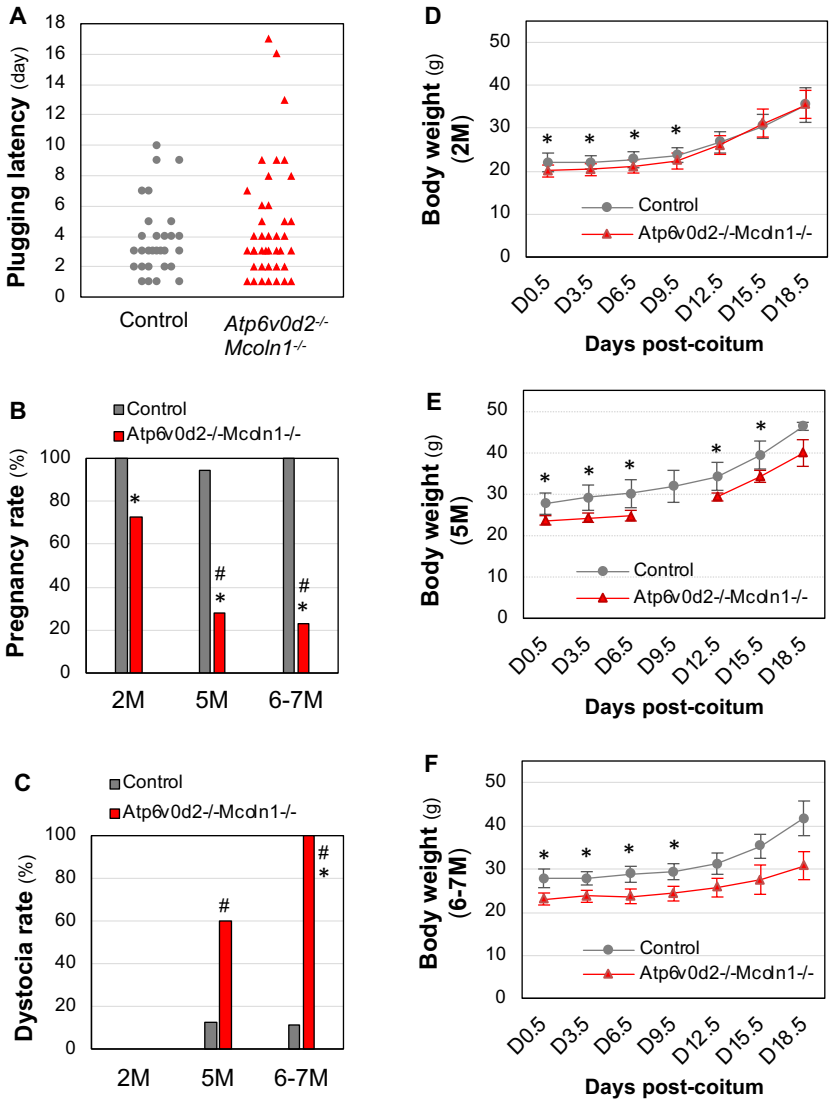

Figure 2.2. Fertility test in *Atp6v0d2*$^{-/-}$*Mcoln1*$^{-/-}$ female mice. A. Plugging latency from cohabitation to detection of the 1st vaginal plug. Control: grey dots, N=29; *Atp6v0d2*$^{-/-}$*Mcoln1*$^{-/-}$: red triangle, N=40. B. Pregnancy rates at 2M, 5M, and 6-7M. Pregnancy ages were based on the time when a vaginal plug was detected. * P<0.05, compared to respective control group; # P<0.05, compared to 2M *Atp6v0d2*$^{-/-}$*Mcoln1*$^{-/-}$ group. Control: N=29 (2M), 17 (5M), and 9 (6-7M); *Atp6v0d2*$^{-/-}$*Mcoln1*$^{-/-}$: N=40 (2M), 18 (5M), and 13 (6-7M). The reduction of 12 mice in the control cohort from 2M to 5M was due to previous pregnancy & nursing (3) therefore not in mating, sickness therefore euthanized (1), dissection for D3.5 serum collection at 5M (4), and

Figure 2.2. (continued) sacrificed following COVID-19 lockdown policy (4). The reduction of 8 mice in the control cohort from 5M to 6-7M was due to previous pregnancy & nursing (1) therefore not in mating, and sacrificed following COVID-19 lockdown policy (7). The reduction of 22 mice in the *Atp6v0d2*$^{-/-}$*Mcoln1*$^{-/-}$ cohort from 2M to 5M was due to previous pregnancy & nursing (1) therefore not in mating, death (1), dissection for D3.5 serum collection at 5M (11), and sacrificed following COVID-19 lockdown policy (9). The reduction of 5 mice in the *Atp6v0d2*$^{-/-}$*Mcoln1*$^{-/-}$ cohort from 5M to 6-7M was due to death before 6M (2), and sacrificed following COVID-19 lockdown policy (3). C. Dystocia rates at 2M, 5M, and 6-7M. * $P<0.05$, compared to respective control group. D-E. Body weight change during pregnancy at pregnancy ages of 2M (D), 5M (E), and 6-7M (F). The numbers of pregnant mice with body weight data were 22, 11, and 5 for control groups, and 26, 4, and 3 for *Atp6v0d2*$^{-/-}$ *Mcoln1*$^{-/-}$ groups, respectively. One missing data point in E was due to incomplete collection of the body weight data. Error bar, standard deviation; *, $P<0.05$, compared to the respective control at the same post-coitum day.

2.4.4 Most *Atp6v0d2*$^{-/-}$*Mcoln1*$^{-/-}$ females having P4 deficiency at 5M old

We previously showed that 100% of the 5M old *Mcoln1*$^{-/-}$ mice examined at D4.5 had P4 deficiency [196]. Since P4 levels reach a plateau by D3.5 in mice [193], comparable P4 levels are expected between D3.5 and D4.5 in the same mice. When the mice were 5M old, we randomly selected 4 control mice and 11 *Atp6v0d2*$^{-/-}$*Mcoln1*$^{-/-}$ mice in the fertility test cohorts for serum collection on D3.5. All 4 control mice had serum P4 levels >20 ng/ml, while some in the *Atp6v0d2*$^{-/-}$*Mcoln1*$^{-/-}$ group had much lower P4 levels. Based on P4 levels (<12 ng/ml as low P4)

and fertility history, the 11 *Atp6v0d2*$^{-/-}$*Mcoln1*$^{-/-}$ mice were divided into three sub-groups (Fig. 2.3A): 1) Low P4 & infertile. Two mice had low P4 levels and no pregnancy despite continuous mating activity indicated by vaginal plugs. The infertility rate (2/11) was comparable to the cohort (8/40). 2) Low P4 & once fertile. Six mice had low P4 levels and had previously produced 1-2 litters during the fertility test. 3) Normal P4. Three mice had comparable P4 levels to the controls and had previously produced 1-2 litters during the fertility test. The percentage of *Atp6v0d2*$^{-/-}$*Mcoln1*$^{-/-}$ mice with normal P4 levels (3/11=27.3%) at 5M was consistent with the pregnancy rate at 5M in the cohort (5/18=27.8%). The serum estrogen (E2) levels between the control and *Atp6v0d2*$^{-/-}$*Mcoln1*$^{-/-}$ mice at 5M were comparable (Fig. 2.3B).

In our previous study, none of the 7 *Mcoln1*$^{-/-}$ females examined at 5M had normal P4 levels and none were fertile [196]. In this study, we found 27.3% (3/11) *Atp6v0d2*$^{-/-}$*Mcoln1*$^{-/-}$ mice at 5M had normal P4 levels (Fig. 2.3A) and 27.8% (5/18) of them were fertile (Fig. 2.2B). Despite no statistically significant differences between the two groups (P4 level: 0/7 vs. 3/11, P=0.2451; fertility: 0/7 vs. 5/18, P=0.2743; two tailed Fisher's exact test), additional deletion of *Atp6v0d2* could rescue P4 level and fertility, or more precisely, prolong the fertility span, in a small portion of *Atp6v0d2*$^{-/-}$*Mcoln1*$^{-/-}$ mice (Fig. 2.2B).

2.4.5 Comparable numbers of follicles and CLs among control, *Mcoln1*$^{-/-}$, and *Atp6v0d2*$^{-/-}$ *Mcoln1*$^{-/-}$ ovaries at 5M

During early pregnancy, P4 is mainly synthesized in the CL, which is normally developed from ovulated follicles. We examined follicles and CLs in the D3.5 ovaries from 5M old control, *Mcoln1*$^{-/-}$ mice, and *Atp6v0d2*$^{-/-}$*Mcoln1*$^{-/-}$ mice. There was no significant difference in the average numbers of follicles at different stages and CLs among these three groups (data not shown). Normal CL numbers coupled with normal mating activities would suggest local factors, instead

of neuroendocrine defect, contributing for P4 deficiency in the *Mcoln1*$^{-/-}$ female mice and majority of *Atp6v0d2*$^{-/-}$*Mcoln1*$^{-/-}$ female mice at 5M old.

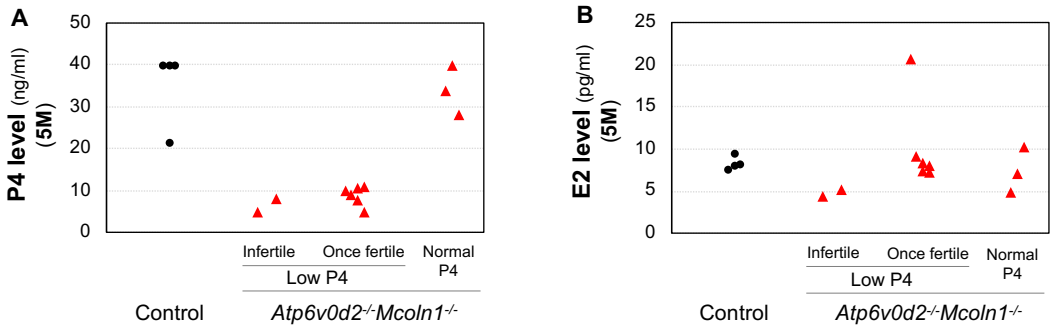

Figure 2.3. Serum progesterone (P4) level (A) and estrogen (E2) level (B). A subset of mice at 5M old was randomly selected from the cohort in the fertility test. Serum was collected at post-coitum day 3.5 (D3.5). N=4 for control mice, black dots; and N=11 for *Atp6v0d2*$^{-/-}$ *Mcoln1*$^{-/-}$ mice, red triangles. *Atp6v0d2*$^{-/-}$*Mcoln1*$^{-/-}$ mice were separated into three subgroups: low P4 & infertile (N=2), low P4 & once fertile (N=6), and normal P4 (N=3).

2.4.6 Completely or partially restored *Atp6v0d2*$^{-/-}$*Mcoln1*$^{-/-}$ CL morphology compared to *Mcoln1*$^{-/-}$ CL at 5M

Representative histology images of D3.5 ovaries are shown in Fig. 2.4A-4H1. In the control CLs, there was defined corpus luteal cords, which are clusters of luteal cells surrounding by endothelial cells, and the luteal cells generally appeared rounded with a large cytoplasm (Fig. 2.4A-4A1). The regressing CLs from a previous cycle had large empty spaces and some dense nuclei but no amorphous cell debris (Fig. 2.4F, 4F1). In the *Mcoln1*$^{-/-}$ CLs (Fig. 2.4B-4B1), corpus luteal cord and vasculature were less defined compared to the control CL (Fig. 2.4A-4A1); luteal cells had foamy cytoplasm, an indication of vacuolization; all CLs in the 6 *Mcoln1*$^{-/-}$

ovaries (1 ovary/mouse) examined were in two main categories: with medium to extensive amorphous cell debris, an indication of cell death (most likely necrosis), for the majority of CLs (Fig. 2.4B-4B1), or regressing without obvious amorphous cell debris but large empty spaces and some dense nuclei (0-2 CLs/ovary) (Fig. 2.4G-4G1), as seen in the control (Fig. 2.4F1). All 6 *Mcoln1*$^{-/-}$ ovaries examined had at least one CL with extensive amorphous cell debris (Fig. 2.4I).

We sectioned 2 ovaries (1 ovary/mouse) from each of the three *Atp6v0d2*$^{-/-}$*Mcoln1*$^{-/-}$ subgroups. In the only 2 *Atp6v0d2*$^{-/-}$*Mcoln1*$^{-/-}$ mice with low P4 & infertile, one had a CL with amorphous cell debris and undeveloped luteal cords (Fig. 2.4C-4C1), and the other had two CLs, one with undifferentiated luteal cells but no obvious amorphous cell debris (Fig. 2.4H-4H1) and the other regressing (data not shown). In the two *Atp6v0d2*$^{-/-}$*Mcoln1*$^{-/-}$ ovaries from low P4 & once fertile group, the CLs rarely had cell debris, but most luteal cells did not have a large cytoplasm area (Fig. 2.4D-4D1), indicating restored cell survival but not luteal cell differentiation. In the two *Atp6v0d2*$^{-/-}$*Mcoln1*$^{-/-}$ ovaries from normal P4 group, the CLs had similar morphology (Fig. 2.4E-4E1) to the control CLs (Fig. 2.4A-4A1), with restored cell survival and luteal cell differentiation. Regressing CLs from a previous cycle in the *Atp6v0d2*$^{-/-}$ *Mcoln1*$^{-/-}$ ovaries had similar morphology as seen in Fig. 2.4F1-4G1. These data demonstrate a general recovery of CL morphology with different degrees in the *Atp6v0d2*$^{-/-}$*Mcoln1*$^{-/-}$ CLs (Fig. 2.4C-4E1, 2.4H-4H1) compared to *Mcoln1*$^{-/-}$ CLs (Fig. 2.4B-4B1). There was a significant recovery of cell survival, indicated by the reduced amorphous cell debris, in the *Atp6v0d2*$^{-/-}$ *Mcoln1*$^{-/-}$ CLs (only 1 ovary out of 6 examined vs. all 6 *Mcoln1*$^{-/-}$ ovaries with significant amorphous cell debris in the CL) (Fig. 2.4I). However, restoration of luteal cell differentiation only occurred in the *Atp6v0d2*$^{-/-}$*Mcoln1*$^{-/-}$ mice with normal P4 levels (Fig. 2.4E-4E1).

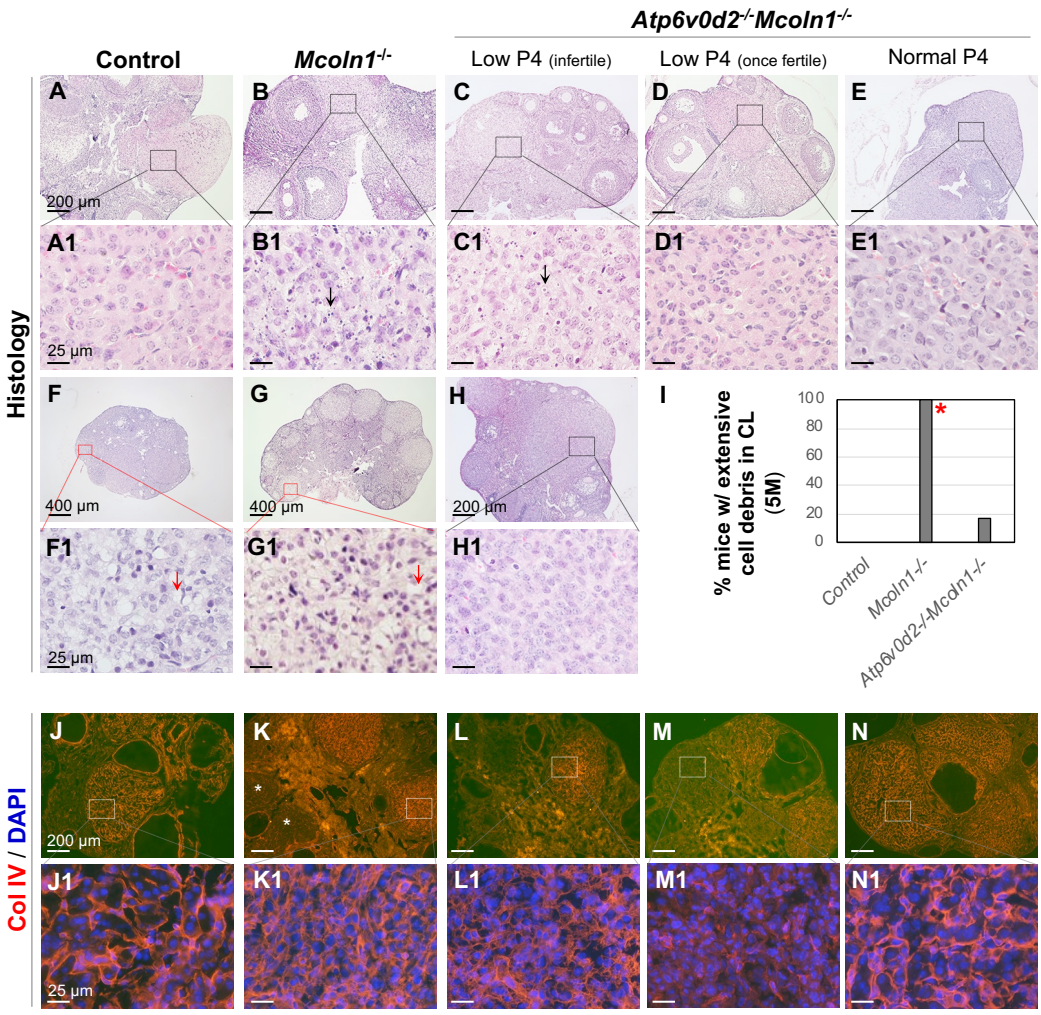

Figure 2.4. Histology of corpus luteum (CL) and collagen IV (Col IV) immunofluorescence in the ovaries. Ovaries were from D3.5 5M old mice that were in the fertility cohort (control and *Atp6v0d2*$^{-/-}$*Mcoln1*$^{-/-}$) or not in the fertility cohort but were non-virgin (*Mcoln1*$^{-/-}$). Five groups of mice were included: control mice, *Mcoln1*$^{-/-}$ mice, and three subgroups of *Atp6v0d2*$^{-/-}$*Mcoln1*$^{-/-}$ mice (low P4 & infertile, low P4 & once fertile, and normal P4). A-H1: H&E staining in fixed ovaries. Black arrow in B1 & C1, amorphous cell debris; F1 & G1, regressing CL from a previous cycle; red arrow in F1 & G1, empty cytoplasm; I. Percentage of mice with extensive amorphous cell debris in the CL. N=4-6/group; * P<0.05, compared to both the control group and the combined *Atp6v0d2*$^{-/-}$*Mcoln1*$^{-/-}$ group, which had

Figure 2.4. (continued) 2 samples each from the three subgroups. J-N1: Col IV staining in frozen ovaries. A, F, J: Control; B, G, K: *Mcoln1*$^{-/-}$; C, H, L: *Atp6v0d2*$^{-/-}$*Mcoln1*$^{-/-}$ low P4 & infertile; D, M: *Atp6v0d2*$^{-/-}$*Mcoln1*$^{-/-}$ low P4 & once fertile; E, N: *Atp6v0d2*$^{-/-}$*Mcoln1*$^{-/-}$ normal P4. A1-H1 & J1-N1: enlarged from the boxed area in A-H & J-N, respectively. P4: progesterone. Col IV: collagen IV. Scale bar: 400 μm in F & G; 200 μm in A-E, H, J-N; and 25 μm in A1-H1 and J1-N1. No specific staining in the follicle or CL but autofluorescence in the interstitial areas of the negative control ovaries (data not shown).

2.4.7 Varied Col IV expression patterns in *Atp6v0d2*$^{-/-}$*Mcoln1*$^{-/-}$ CL at 5M

Collagen IV (Col IV) is a marker of the basal lamina of endothelial cells. It is highly expressed in the CL but not the follicles [21, 199], corresponding to the high vasculature in the CL but not follicles [201]. Immunofluorescence of Col IV in the control ovary revealed a continuous net-like Col IV expression pattern that surrounded the empty spaces without Col IV staining, reflecting endothelial cells wrapping around clusters of luteal cells in the luteal cords (Fig. 2.4J-4J1). In the age-matched D3.5 *Mcoln1*$^{-/-}$ CLs, the net-like Col IV expression pattern was much denser, leaving smaller empty spaces surrounded by the continuous Col IV staining (Fig. 2.4K-4K1), an indication of undeveloped / under-developed luteal cords in the *Mcoln1*$^{-/-}$ CL. Similar patterns of Col IV staining in the *Mcoln1*$^{-/-}$ CL were also observed in the *Atp6v0d2*$^{-/-}$ *Mcoln1*$^{-/-}$ CLs with low P4 levels, regardless of the fertility history (Fig. 2.4L, 2.4L1, 2.4M). Among the three CLs shown in Fig. 4M, two had similar Col IV expression patterns (data not shown) as seem in Fig. 2.4K1 and Fig. 2.4L1; one CL had much less overall Col IV intensity

(Fig. 2.4M) than other CLs, and the Col IV staining was disorganized and low (Fig. 2.4M1), this CL was most likely a regressing CL from a previous cycle (Fig. 2.4M1). The CLs from *Atp6v0d2*$^{-/-}$*Mcoln1*$^{-/-}$ mice with normal P4 levels had comparable Col IV expression pattern (Fig. 2.4N-4N1) as the control CLs (Fig. 2.4J-4J1).

2.4.8 Lipid accumulation associated with P4 deficiency in *Atp6v0d2*$^{-/-}$*Mcoln1*$^{-/-}$ CLs

Lysosomal storage disorder MLIV caused by mutations in *MCOLN1* gene is associated with lipid accumulation [202, 203]. Lipid droplets contain cholesterol, the precursor for P4 synthesis [27]. Nile Red was used to detect lipid droplets in the CL [21, 196]. The lipid droplets in the control CLs were relatively small and uniform, some were too small to be distinctive in the image (Fig. 2.5A-5A1). Those in the *Mcoln1*$^{-/-}$ CLs had varied sizes with increased number of larger ones (Fig. 2.5B-5B1). The lipid droplets in the *Atp6v0d2*$^{-/-}$*Mcoln1*$^{-/-}$ CLs with low P4 levels also had increased numbers of larger sizes (Fig. 2.5C-5D1) similar as that in the *Mcoln1*$^{-/-}$ CLs (Fig. 2.5B-5B1). The lipid droplets in the *Atp6v0d2*$^{-/-}$*Mcoln1*$^{-/-}$ CLs with normal P4 levels (Fig. 2.5E-5E1) were relative fine and uniform as those in the control (Fig. 2.5A-5A1). These data indicate complete recovery of lipid droplet sizes in the CLs of *Atp6v0d2*$^{-/-}$*Mcoln1*$^{-/-}$ mice with normal P4 but not obvious recovery in the CLs of *Atp6v0d2*$^{-/-}$*Mcoln1*$^{-/-}$ mice with P4 deficiency compared to those in the *Mcoln1*$^{-/-}$ CLs.

2.4.9 Recovery of mitochondrial density and StAR expression in CLs of *Atp6v0d2*$^{-/-}$*Mcoln1*$^{-/-}$ mice with normal P4 levels

P4 synthesis initiates in the mitochondria and the rate-limiting step is the transport of cholesterol from the outer to the inner mitochondrial membrane by StAR (steroidogenic acute regulatory protein) [27, 28]. Heat shock protein 60 (HSP60) is a mitochondrial marker. Both HSP60 and StAR were highly detected in the cytoplasm of luteal cells in the control CLs (Fig.

2.5F, 2.5F1, 2.5K, 2.5K1) and *Atp6v0d2*$^{-/-}$*Mcoln1*$^{-/-}$ CLs from mice with normal P4 levels (Fig. 2.5J, 2.5J1, 2.5O, 2.5O1). Their expression levels in the other three groups with low P4 levels were consistently low (Fig. 2.5G-5I1, 2.5L-5N1). These results demonstrate the correlation between the mitochondrial density and StAR expression levels with serum P4 levels regardless of genotypes. The investigated parameters at 5M are summarized in Table 1.

Table 1. Summary of the parameters at 5M

Parameters	Control	*Mcoln1*$^{-/-}$	*Atp6v0d2*$^{-/-}$*Mcoln1*$^{-/-}$		
	Normal P4	Low P4 & infertile	Low P4 & infertile	Low P4 & once fertile	Normal P4
No. follicle & CL	Comparable				
Cell debris in CL	-	+++	++/-	-	-
Luteal cell differentiation	+++	-	-	-	+++
Col IV	Normal	Disorganized	Disorganized	Disorganized	Normal
Lipid droplets	+	+++	+++	+++	+
HSP60	+++	-	-	-	+++
StAR	+++	-	-	-	+++

+: higher level of cell debris, more larger lipid droplets, or higher expression of HSP60 and StAR.

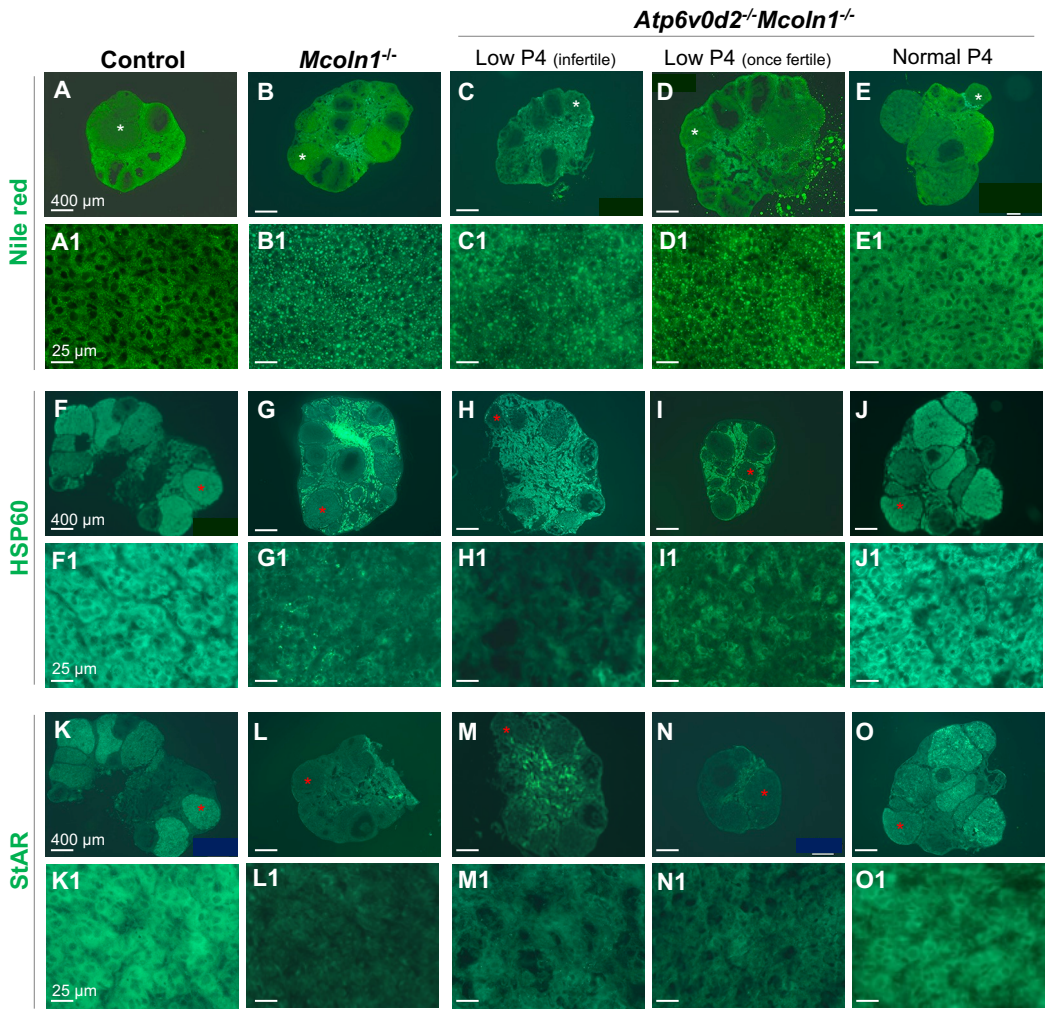

Figure 2.5. Nile red staining of lipid droplets and immunofluorescence detection of HSP60 and StAR in frozen ovaries from 5M old mice at D3.5. Five groups of mice were included: control mice, *Mcoln1*$^{-/-}$ mice, and three groups of *Atp6v0d2*$^{-/-}$*Mcoln1*$^{-/-}$ mice (low P4 & infertile, low P4 & once fertile, and normal P4). A-E1: Nile red staining. F-J1: HSP60. K-O1: StAR. A, F, K: Control; B, G, L: *Mcoln1*$^{-/-}$; C, H, M: *Atp6v0d2*$^{-/-}$*Mcoln1*$^{-/-}$ low P4 & infertile; D, I, N: *Atp6v0d2*$^{-/-}$*Mcoln1*$^{-/-}$ low P4 & once fertile; E, J, O: *Atp6v0d2*$^{-/-}$*Mcoln1*$^{-/-}$ normal P4 level. A1-O1: enlarged from the CL labeled with * in A-O, respectively. P4: progesterone; HSP60: heat shock protein 60; StAR: steroidogenic acute regulatory protein. Scale bar, 400 μm in A-O, and 25 μm in A1-O1. No specific staining in the follicle or CL but autofluorescence in the interstitial areas of the negative control ovaries (data not shown).

2.5 Discussion

One deficiency in this study was the lack of direct evidence of colocalization of V-ATP subunit ATP6v0d2 (encoded by *Atp6v0d2*) and TRPML1 (encoded by *Mcoln1*) in the wild type luteal cells and absence of them in the *Atp6v0d2*$^{-/-}$*Mcoln1*$^{-/-}$ luteal cells. We were fortunate to receive a vial of anti-TRMPL1 antibody from Dr. Abigail A Soyombo [189] before she closed her lab. With this antibody, we detected TRPML1 in the ovary, including luteal cells in the CL [196]. Prior to the initiation of this project, we tested a few commercially available anti-ATP6v0d2 and anti-TRPML1 antibodies for immunohistochemistry and immunofluorescence, but none worked. With the breeding for generating *Atp6v0d2*$^{-/-}$*Mcoln1*$^{-/-}$ mice ongoing, we made customized antibodies but again, none worked. We resorted to the literature for support that ATP6v0d2 and TRPML1 are expected to co-localize in some intracellular organelles, especially lysosomes [85].

Collagen IV (Col IV), a basal lamina marker of endothelial cells, was shown in our previous study to have comparable overall intensity to the interstitial compartment in the D3.5 *Mcoln1*$^{-/-}$ CLs, while the control CLs had overall higher expression levels than the interstitial compartment [196]. In this study, we did not consistently observe such a pattern. This might be due to different batches of the antibody used in these two studies and/or varied intensity of autofluorescence in the intestinal compartment (but not follicles or CLs) that we consistently detect in the negative controls (data not shown). Regardless, the Col IV expression patterns in the control and *Mcoln1*$^{-/-}$ CLs and no staining in the follicles were consistent in the two studies. Although we observed partial recovery in the CL morphology, e.g., less cell death indicated by reduced amorphic cell debris in the *Atp6v0d2*$^{-/-}$*Mcoln1*$^{-/-}$ CLs, no obvious difference was observed in the Col IV staining patterns among *Mcoln1*$^{-/-}$ group and two *Atp6v0d2*$^{-/-}$*Mcoln1*$^{-/-}$

subgroups with low P4 levels. CL morphology indicated that these three group & subgroups lacked well-differentiated luteal cells. This observation indicates that Col IV staining pattern correlates with luteal cell differentiation and P4 levels but not cell survival in the CL.

Luteal cell differentiation and P4 levels are also correlated with lipid droplet accumulation and expression of HSP60 and StAR in the CL. Lipid droplet accumulation is a hallmark of MLIV, which is due to TRPML1 deficiency caused by *MCOLN1* mutations [202, 203]. TRPML1 deficiency can lead to mitochondrial fragmentation likely due to inefficient autophagolysosomal recycling of mitochondria [204]. The expression of HSP60, a mitochondrial marker, and StAR, which carries out the rate-limiting step in steroidogenesis to transport the substrate cholesterol from the outer to the inner mitochondrial membrane, is directly related to the mitochondrial quantity and function. Comparable lipid droplet accumulation and reduced expression of HSP60 and StAR in the 5M D3.5 *Mcoln1*$^{-/-}$ group and two *Atp6v0d2*$^{-/-}$*Mcoln1*$^{-/-}$ subgroups with low P4 levels would suggest that the levels of restoration in the *Atp6v0d2*$^{-/-}$ *Mcoln1*$^{-/-}$ CLs of these two subgroups was enough to restore luteal cell survival in most mice but was insufficient to restore the lysosomal functions in regulating lipids and mitochondria. This places cell survival as the fundamental cellular event to be restored first.

There might be a threshold for restoration of other lysosomal functions. We observed about a quarter of *Atp6v0d2*$^{-/-}$*Mcoln1*$^{-/-}$ female mice with normal P4 levels and all the examined CL parameters at 5M (Table 1), indicating full recovery of lysosomal functions in the CL of this subgroup of *Atp6v0d2*$^{-/-}$*Mcoln1*$^{-/-}$ mice compared to that in the *Mcoln1*$^{-/-}$ CL. Consistently, we observed ~a quarter of *Atp6v0d2*$^{-/-}$*Mcoln1*$^{-/-}$ female mice remained fertile till 7 months old and some pregnancies expanded to 8 months old. We did not continue fertility tests beyond then due to progressive neurological defects. We do not know the molecular mechanisms leading to the

full recovery of CL functions and fertility of ~a quarter of *Atp6v0d2*$^{-/-}$*Mcoln1*$^{-/-}$ female mice while partial recovery of CL cell survival only in the remaining ~three quarters of *Atp6v0d2*$^{-/-}$ *Mcoln1*$^{-/-}$ female mice at 5M. One potential explanation is that ATP6V0d2 plays varied roles in the CLs leading to varied outcomes. TRMPL1 was shown to be a lysosomal channel that can leak out H^+ to coregulate lysosomal pH with V-ATPase [203]. TRMPL1 deficiency in cells from MLIV patients and *Mcoln1*$^{-/-}$ mice leads to overly acidified lysosomes due to accumulation of H^+ in the lysosomal lumen [203]. Therefore, if V-ATPase is impaired in pumping H^+ into the lysosomal lumen, the accumulation of H^+ in the lysosomal lumen would be alleviated in the TRMPL1 deficient lysosomes. When such an alleviation reaches a threshold to restore the lysosomal ionic homeostasis and membrane potential, the lysosomal functions will be restored. In the CLs where ATP6V0d2 play a significant role in V-ATPase activity for pumping H^+ in the lysosomal lumen and its role could not be compensated by ATP6V0d1 or other channels, ATP6V0d2 deficiency will lead to reduced V-ATPase activity and less H^+ pumped into the lysosomal lumen, reaching a new balance for the lysosome to be fully functional. In the CLs where ATP6V0d2 affect V-ATPase activity to a lesser significant level, ATP6V0d2 deficiency will correct the imbalance caused by TRPML1 deficiency to a lesser extent, such as improving cell survival in the CL but no other parameters examined (Table 1 and Fig. 2.6).

However, the assumed restoration of lysosomal functions seems to be cell type specific, most likely due to ATP6V0d2 being the more tissue-specific d subunit of the V-ATPase and cell/tissue-specific functions of V-ATPase subunits are common [40, 194]. The restoration of CL function and fertility in the ~a quarter of *Atp6v0d2*$^{-/-}$*Mcoln1*$^{-/-}$ female mice at 5M and 6-7M does not seem to occur in the uterine myometrium. We observed 60% (5M) and 100% (6-7M) of fertile *Atp6v0d2*$^{-/-}$*Mcoln1*$^{-/-}$ mice with dystocia. Since the most common cause of dystocia is

inefficient uterine contraction, the age-dependent progressively increased rates of dystocia in the pregnant *Atp6v0d2*$^{-/-}$*Mcoln1*$^{-/-}$ mice indicates that lysosomal functions are important for uterine contraction. There have been studies connecting lysosomal functions with parturition (reviewed in [205]), but systemic studies are still lacking. Our initial reason for studying players in the lysosomal functions in the uterus was the observations of the dramatic upregulation of *Atp6v0d2* in the uterine luminal epithelium and uterine epithelial acidification upon embryo implantation initiation [37, 42]. We have not examined *Atp6v0d2* expression in the myometrium towards parturition. We previously detected *Atp6v0d2* in uterine luminal epithelium of D4.5 mouse uterus but *Atp6v0d2* was undetectable in D4.5 myometrium [42]. If ATP6V0d2 remains undetectable in the myometrium throughout the pregnancy, the dystocia in the 5-7M *Atp6v0d2*$^{-/-}$*Mcoln1*$^{-/-}$ mice would be caused by *Mcoln1* deletion. Using the gift anti-TRPML1 antibody from Dr. Soyombo [189], we detected TRPML1 in the mouse myometrium during early pregnancy (unpublished observation). We have not examined TRPML1 expression in the mouse myometrium towards parturition. These observations suggest a novel function of TRPML1 in parturition.

This study demonstrates that deletion of both *Atp6v0d2* and *Mcoln1* in female mice can restore CL cell survival in most mice and can restore fertility in a quarter of the mice compared to deletion of *Mcoln1* alone. Although the mechanisms behind the various individual effects remain to be investigated, this study provide the first *in vivo* genetic evidence on coordination of different lysosomal players in luteal cell function.

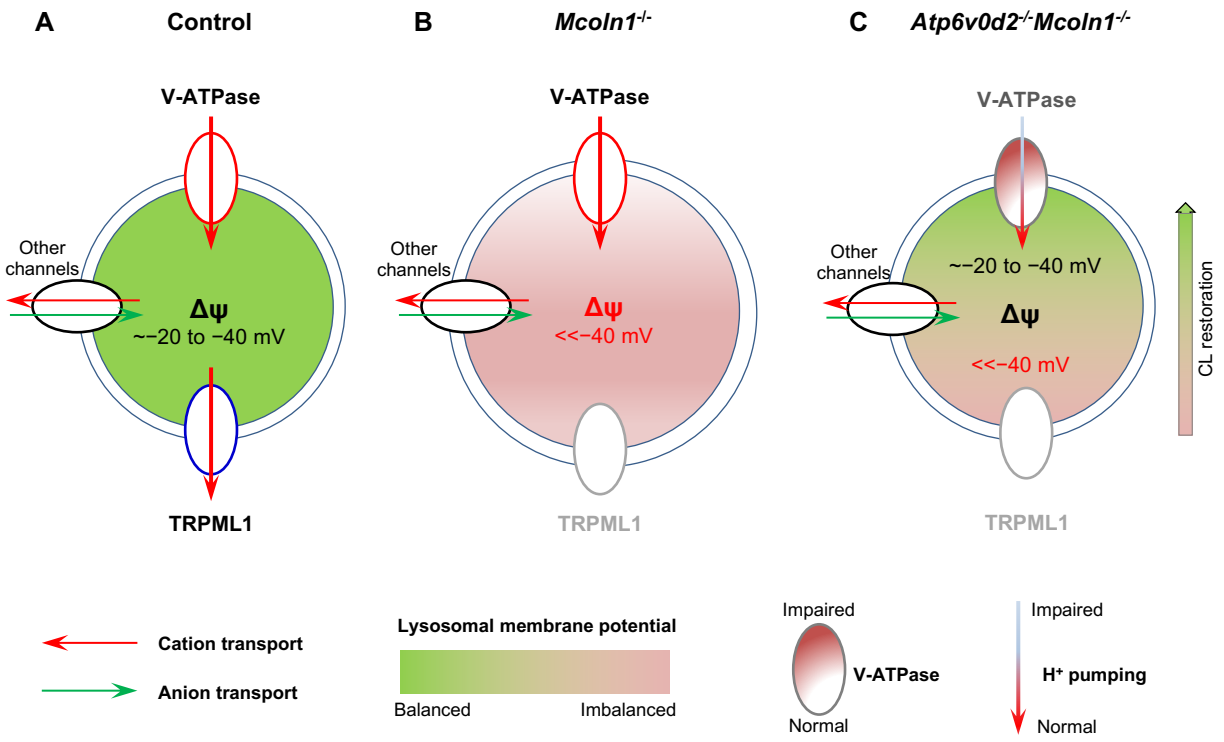

Figure 2.6. Proposed model for varied rescuing effects in *Atp6v0d2*$^{-/-}$*Mcoln1*$^{-/-}$ CL compared to *Mcoln1*$^{-/-}$ CL. *Atp6v0d2* encodes one of the two ATP6V0d subunits for V-ATPase, which pumps H^+ from cytosol to lysosomal lumen. *Mcoln1* encodes TRPML1, a cation counter ion channel that transport cations, including H^+, from lysosomal lumen to cytosol. TRPML1 deficiency leads to MLIV, a progressive and severe lysosomal storage disorder with a slow onset. The proposed model is for D3.5 CLs from 5M old mice that have been in mating since 2M old. A. Control. Balanced lysosomal lumen ionic homeostasis and membrane potential (Δψ), indicated by the green lumen. B. *Mcoln1*$^{-/-}$. Imbalanced lysosomal ionic components and disrupted membrane potential, which is expected to be abnormally negative due to accumulation of cations resulted from TRPML1 deficiency, indicated by the pink lumen. C. *Atp6v0d2*$^{-/-}$*Mcoln1*$^{-/-}$. Gradient rescue of lysosomal lumen ionic homeostasis and membrane potential by additional ATP6V0d2 deficiency. In the CLs where ATP6V0d2

Figure 2.6. (continued) deficiency leads to more impairment of V-ATPase activity in pumping H^+ in the lysosomal lumen, the imbalance caused by TRPML1 deficiency could be canceled out to reach a new balance for the lysosome to be fully functional, indicated by gradient reddish V-ATPase, greyish arrow, and greenish lysosomal lumen. In the CLs where ATP6V0d2 deficiency has no or minor impairment of V-ATPase activity, the imbalance caused by TRPML1 deficiency could not or could only be partially corrected, indicated by gradient whitish V-ATPase, reddish arrow, and pinkish lysosomal lumen.

Acknowledgements

The authors thank the Office of the Vice President for Research, Interdisciplinary Toxicology Program, and Department of Physiology and Pharmacology at the University of Georgia, and the National Institutes of Health (NIH R01HD065939 (co-funded by ORWH and NICHD), R03HD097384, and R03 HD100652 to XY) for financial support. Serum P4 and E2 levels were determined at The University of Virginia Center for Research in Reproduction Ligand Assay and Analysis Core, which is supported by the Eunice Kennedy Shriver NICHD/NIH (NCTRI) Grant P50-HD28934.

CHAPTER 3

VISUALIZATION OF PREIMPLANTATION UTERINE FLUID ABSORPTION IN MICE USING ALEXA FLUOR™ 488 HYDRAZIDE[2]

[2] Li, Y., Martin, T.E., Hancock, J.M., Li, R., Viswanathan, S., Lydon, J.P., Zheng, Y., Ye, X. 2023. *Biology of Reproduction*. 108(2):204-217. Reprinted here with permissions of the publisher.

3.1 Abstract

Uterine fluid plays important roles in supporting early pregnancy events and its timely absorption is critical for embryo implantation. In mice, its volume is maximum on day 0.5 post-coitum (D0.5) and approaches minimum upon embryo attachment ~D4.0. Its secretion and absorption in ovariectomized rodents were shown to be promoted by estrogen and progesterone (P4), respectively. The temporal mechanisms in preimplantation uterine fluid absorption remain to be elucidated. We have established an approach using intraluminally injected Alexa Fluor™ 488 Hydrazide (AH) in preimplantation control (*RhoA*$^{f/f}$) and P4-deficient *RhoA*$^{f/f}$*Pgr*$^{Cre/+}$ mice. In control mice, bulk entry (seen as smeared cellular staining) via uterine luminal epithelium (LE) decreases from D0.5 to D3.5. In P4-deficient *RhoA*$^{f/f}$*Pgr*$^{Cre/+}$ mice, bulk entry on D0.5 and D3.5 is impaired. Exogenous P4 treatment on D1.5 and D2.5 increases bulk entry in D3.5 P4-deficient *RhoA*$^{f/f}$*Pgr*$^{Cre/+}$ LE while progesterone receptor (PR) antagonist RU486 treatment on D1.5 and D2.5 diminishes bulk entry in D3.5 control LE. The abundance of autofluorescent apical fine dots, presumptively endocytic vesicles to reflect endocytosis, in the LE cells is generally increased from D0.5 to D3.5 but its regulation by exogenous P4 or RU486 is not obvious under our experimental setting. In the glandular epithelium (GE), bulk entry is rarely observed and green cellular dots do not show any consistent differences among all the investigated conditions. This study demonstrates the dominant role of LE but not GE, the temporal mechanisms of bulk entry and endocytosis in the LE, and the inhibitory effects of P4-deficiency and RU486 on bulk entry in the LE in preimplantation uterine fluid absorption.

3.2 Introduction

It was first reported exactly 100 years ago that the volume of fluid in the uterine cavity/lumen (uterine fluid) is dynamic during estrous cycle in rats, with uterine fluid accumulation at proestrus and estrus [206]. The uterine fluid volume is also dynamic during early pregnancy, as it peaks within the first day post-ovulation/post-coitum and reaches minimum at the time of embryo implantation in rodents (reviewed in [45, 193]). In the physiological condition, the uterine fluid volume is the net result of secretion and absorption. The general observations in ovariectomized rodent models are that ovarian hormones estrogen (E2) induces uterine fluid secretion while P4 promotes uterine fluid absorption [46, 51, 207-211].

Uterine fluid plays important roles in supporting early pregnancy events. Key events in natural early pregnancy include fertilization, embryo development, and embryo transport in the Fallopian tube (human)/oviduct (mouse); as well as continuous embryo development, transport, and implantation in the uterus [8, 45, 193]. Preovulatory E2-induced uterine fluid secretion facilitates semen liquefaction to free the sperm and provides a conducive environment for sperm migration to the Fallopian tube/oviduct for fertilization [212, 213]. Postovulatory P4-induced uterine fluid absorption leads to uterine lumen closure, which enables intimate contact of the implanting embryo with the uterine luminal epithelium (LE) to initiate embryo implantation [193]. Uterine fluid, which is recently revealed in heifers to be metabolically semi-autonomous [214], also relays maternal signals to the preimplantation embryo, and vice versa, to facilitate embryo-maternal communications for embryo implantation [193, 210, 215]. The orchestration of early pregnancy events leading up to embryo implantation is critical for successful pregnancy [193, 216]. In assisted early pregnancy, such as in vitro fertilization-embryo transfer (IVF-ET) that does not involve other early pregnancy events in the female reproductive tract prior to

embryo implantation, uterine fluid is still a critical factor for successful embryo implantation. For example, patients with excessive uterine fluid retention at the time of IVF-ET is correlated with reduced rate of embryo implantation, which was confirmed by rising serum β-HCG levels and the presence of gestational sacs [217]. Timely absorption of preimplantation uterine fluid is critical for embryo implantation in both humans and mice [198, 210, 218-222].

Uterine fluid movement is accompanied with ion movement and endocytic activity. In ovariectomized rats, E2 treatment induces secretion of water, sodium ion (Na^+, the dominant electrolyte in the uterine fluid), and potassium ion (K^+) into the uterine lumen accompanied with an increased Na^+/K^+ ratio, while P4 treatment reabsorbs water, Na^+, and K^+, with a reduced Na^+/K^+ ratio [46, 207]. Since ligations of the uterine horn to block uterine fluid leakage through oviductal side and cervical side do not affect P4-induced uterine fluid absorption [46], uterine fluid absorption has to pass through the uterine epithelium, which borders the uterine lumen where the uterine fluid stays. Because of the limited paracellular flow in the uterine epithelium [101], transcelluar flow through the apical membrane of uterine epithelium is expected to be the essential passage for uterine fluid absorption. Since there is limited capacity for water passive diffusion through the lipid bilayer of the plasma membrane and osmotic gradient is in general a main driving force for water movement through the plasma membrane, the absorption of the dominant electrolyte Na^+ in the uterine fluid will generate an osmotic gradient, which is expected to facilitate water absorption via bulk entry. Na^+ is absorbed through sodium channels, and its entry via the amiloride-sensitive epithelial Na^+ channel (ENaC, encoded by *Scnn1a*, *Scnn1b*, *Scnn1g*) is the rate-limiting step for Na^+ absorption across several epithelial tissues [223], therefore, ENaC is expected to be a key player to transport Na^+ from the uterine fluid to the uterine epithelial cells. Indeed, a uterine perfusion study in E2 and P4-treated ovariectomized

rats reveals that amiloride inhibits P4-induced uterine fluid absorption [51]. A study of electrogenic ion transport across the cultured primary mouse uterine epithelial cells reveals the dominant contribution of apically absorbed Na^+ for the basal current, which can be inhibited by ENaC inhibitor amiloride [224]. These studies indicate the essential role of ENaC in apical Na^+ transport into the uterine epithelial cells. To maintain intracellular homeostasis, the absorbed Na^+ ions are pumped out of the epithelial cell into subepithelial space, a process involving the Na^+/K^+ ATPase located on the basolateral membrane [225, 226]. Na^+/K^+ ATPase is composed of a catalytic α subunit and an auxiliary β subunit. ATP1A1 is the dominant α subunit in the LE [37]. Water channels/aquaporins (AQPs) have their primary functions in facilitating bidirectional water movement across cell membranes in response to osmotic gradients, among other functions [227-229]. There are 13 AQPs (AQP0-AQP12) in three categories: classical aquaporins (AQP0, AQP1, AQP2, AQP4, AQP5, AQP6, and AQP8) that are considered primarily selective to water; aquaglyceroporins (AQP3, AQP7, AQP9, and AQP10) have larger pore sizes and also permeate glycerol, urea, and other small non-charged solutes; and nonorthodox aquaporins (AQP11 and AQP12) that are intracellular paralogs with functions still under investigation [230]. One study examined the expression of *Aqp0-Aqp9* in mouse uterus and showed that only *Aqp4* and *Aqp5* were mainly detected in the preimplantation mouse uterine epithelium [231]. Another study demonstrated the upregulation of AQP5 and AQP8 by E2 in the preimplantation mouse GE and AQP5 and AQP8 had *in vivo* function in uterine fluid secretion [210]. Embryo implantation requires a receptive uterus, and the establishment of uterine receptivity is associated with the appearance of pinopodes, the protrusions of the LE apical surface that have endocytic activity, and their appearance is P4-dependent [232-235]. These studies demonstrate that P4 signaling regulates both bulk entry and endocytosis of uterine fluid.

During early pregnancy, P4 is mainly synthesized from the corpus luteum, which is normally developed from the newly ovulated ovarian follicle [201]. Preimplantation serum P4 levels rise shortly after ovulation and copulation in mice [236-238] and the general consensus is that it reaches a plateau prior to embryo implantation [8, 193], which initiates ~day 4.0 post-coitum (D4.0) in mice [239]. Massive uterine fluid reduction occurs on D0.5 [193] when endocytosis of macromolecules from uterine lumen was reported undetectable [101]. There have been debates on cellular mechanisms of uterine fluid absorption and to this point, the roles of LE and GE in uterine fluid absorption have not been differentiated. We hypothesized that bulk entry and endocytosis are two mechanisms that temporally mediate P4 regulation of preimplantation uterine fluid absorption, and uterine epithelium LE and GE may play different roles in uterine fluid absorption. This hypothesis was tested in control and our *RhoA*$^{f/f}$*Pgr*$^{Cre/+}$ mouse model with P4 deficiency [21], coupled with exogenous P4 or RU486 treatments. We have developed a novel method using Alexa Fluor™ 488 Hydrazide (AH) to visualize uterine fluid absorption during early pregnancy in mice.

3.3 Materials and Methods

Mice and treatments. CD-1 mice were purchased from Charles River (8-10 weeks old) for pilot experiments to evaluate various parameters for establishing the AH injection and detection procedures, including intraluminal injection, AH concentration and volume, post AH injection dissection timing, detection of AH fluorescence, and selection of early pregnancy time points. The established AH injection and detection procedures were subsequently used in *RhoA*$^{f/f}$ (control) and *RhoA*$^{f/f}$*Pgr*$^{Cre/+}$ female mice, which have P4 deficiency and are infertile, via mating *RhoA*$^{f/f}$ females with *RhoA*$^{f/f}$*Pgr*$^{Cre/+}$ males that we generated and genotyped as described

previously [21]. Virgin adult *RhoA*$^{f/f}$ (control) and *RhoA*$^{f/f}$*Pgr*$^{Cre/+}$ female mice (~6 months old) were mated with wild type stud males and checked for the presence of a vaginal plug every morning. The day of plug identification is defined as D0.5 (note: D0.5 is also designated as D1 or occasionally D0 in the literature; when the related papers with different designations are cited, the dating of early pregnancy is converted to our dating system). Same genotype littermates were assigned into different time points/treatment groups. There were 7 groups of mice: D0.5 *RhoA*$^{f/f}$, D0.5 *RhoA*$^{f/f}$*Pgr*$^{Cre/+}$; D3.5 *RhoA*$^{f/f}$ oil, D3.5 *RhoA*$^{f/f}$ P4, D3.5 *RhoA*$^{f/f}$ RU486; D3.5 *RhoA*$^{f/f}$*Pgr*$^{Cre/+}$ oil, and D3.5 *RhoA*$^{f/f}$*Pgr*$^{Cre/+}$ P4. N=3-5/group. Treatments were a single subcutaneous (s.c.) injection of the same chemical each on D1.5 and D2.5 between 11-12 h with one of the following: vehicle control (0.1 ml sesame oil, Sigma, S3547-1L), P4 (2 mg/0.1 ml/mouse, Sigma, P0130-25G), or RU486 (200 µg/0.1 ml/mouse, Fisher, B1511100). All mice were maintained on Labdiet mouse chow 5053. They were housed in polypropylene cages with free access to food and water on a 12 h light/dark cycle (0600–1800) at 23±1°C with 30–50% relative humidity. All methods used in this study were approved by the University of Georgia Institutional Animal Care and Use Committee (IACUC) Committee and conform to National Institutes of Health guidelines and federal law.

Alexa hydrazide (AH) injection and tissue dissection. Alexa Fluor™ 488 Hydrazide (AH, MW: 570.48) (ThermoFisher, A10436) was dissolved in 1x PBS at 80 µg/ml, which was then 1:1 mixed with 1% Evans blue dye (MP Biomedicals, 151108) solution for tracing AH injection into the uterine lumen, to make the AH working solution at 40 µg/ml for intrauterine luminal injection. *AH injection*: At ~11 h on D2.5 (for the pilot experiment), and D0.5 and D3.5, the assigned mice were anesthetized with isoflurane (Patterson Veterinary Supply, 07-893-1389) inhalation for surgery. The uterine horns were located via a small dorsal incision on each side.

AH (~6.5 µl for D0.5 uterine horns and ~4.5 µl for D3.5 uterine horns) was injected into each uterine horn via the uterotubal junction. The blue color would quickly spread to the cervical side of the uterine horn. The left and right uterine horns were dissected at 5 minutes (min) and one hour (1 h), respectively, after AH injection. Approximately ~2/3 of the uterotubal side of the uterine horn was processed for detecting AH fluorescence and the rest ~1/3 of the cervical side of the uterine horn was flash-frozen.

Detection of uterine fluid absorption via AH fluorescence. The uterotubal side ~2/3 uterine segment was fixed in 4% paraformaldehyde in 1xPBS (pH 7.2) at 4°C for 2 hours, rinsed in 1xPBS twice, and then immersed in 25% sucrose in 1xPBS (pH 7.2) at 4°C for overnight. In the following day, the uterine tissue was embedded in Tissue-Tek O.C.T for cross sections (10 µm) in the dark. Sections were counterstained and mounted in 4',6'-diamino-2-phenylindole (DAPI)-containing Vectashield (Vector Laboratories). Images of AH fluorescence (green) and DAPI staining (blue) were captured.

Detection of uterine autofluorescence. D0.5 and D3.5 mice were processed exactly as for AH injection except that the mice were intraluminally injected with the same volume of vehicle (1xPBS with Evans blue dye). The uterine horns were dissected and processed similarly as those from AH injection.

Immunofluorescence. E-Cadherin (E-Cad, Cell Signaling, 24E10), lysosomal-associated membrane protein 2 (LAMP2, DSHB, ABL-93) and alpha 1 sodium-potassium ATPase (ATP1A1, abcam, ab7671) were detected via immunofluorescence as previously described [21]. Briefly, frozen sections were fixed in 4% paraformaldehyde for 20 min and then subjected to antigen retrieval in 0.01M sodium citrate (pH 6.0) at 95ºC for 20 min. Sections were then washed with 1xPBS and permeabilized with 0.15% Triton X-100. The slides were washed and

blocked with 10% goat serum (ThermoFisher, 16210064) for 1 h at room temperature; they were subsequently incubated with anti-E-Cad (1:1000), or anti-LAMP2 (1:80), or anti-ATP1A1 (1:1000) in a humid chamber at 4^{o}C for overnight. On the following day, slides were first washed in 1x PBS and then incubated with a secondary antibody (ThermoFisher, A11034 (1:200) for detecting E-Cad, A11007 (1:1000) for detecting LAMP2, and A11031 (1:200) for detecting ATP1A1). The sections were counterstained and mounted with DAPI for examination. Negative controls were processed together without the primary antibody. Uterine sections from different groups of mice were placed on the same slides for processing to detect ATP1A1. Images were captured at the same exposure setting using a Carl Zeiss imaging system with an AxioCam MRc5 digital camera. The presented ATP1A1 images had a resolution of 300 pixels/inch and were only edited for sizes but none of the other parameters, such as exposure levels or contrasts.

Semi-quantification of data. Bulk absorption and endocytosis were semi-quantified by two authors independently. The average of each parameter from each mouse was counted as one data point for statistical analyses. Semi-quantification of bulk absorption was based on the estimation of the percentage of LE segment(s) with discernable smeared cellular AH fluorescence relative to the surrounding area: 5 (>90%, intense), 4 (>50%, intense), 3 (>20%, intense), 2 (>5%, intense), 1 (scattered, intense), 0.5 (scattered, not intense), and 0 (nondiscernable). The abundance of autofluorescent apical fine dots, which were presumptively endocytic vesicles to reflect endocytosis, in the LE cells was semi-quantified based on the estimation of the percentage of LE cells with fine autofluorescent dots forming a string of apical punctae: 3 (>90%), 2 (>50), 1 (>5%), 0.5 (scattered), and 0 (nondiscernable). Bulk absorption in GE was rare, therefore, was not quantified. Since we did not observe any consistent difference in

the presence of green dots in the GEs among different groups, endocytosis in GE was not quantified.

Statistical Analysis. The semi-quantitative data are presented as mean±SD. Paired two-tailed student t-test was used for comparisons of parameters between 5 min and 1 h of the same set of samples. Ranking coupled with two-tailed unequal variance student t-test was used for other comparisons between two genotypes or between two time points or two treatments within the same genotype. Significance level was set at $P<0.05$.

3.4 Results

3.4.1 Establishing intraluminal AH injection and AH fluorescence detection procedure

AH was used in organ culture of intestinal tissues at 20 μg/ml [240]. We made the AH working solution at 40 μg/ml with blue dye to track the spreading of AH in the uterine lumen. The final AH concentrations in the uterine lumen are expected to vary greatly because there is a big difference in the uterine fluid volume during early pregnancy in mice, e.g., from up to 100 μl/uterine horn on D0.5 (Fig. 3.1A, large uterine lumen with extensive LE and LE folding upon drainage of uterine fluid) to possibly a few μl or even less approaching embryo implantation (Fig. 3.1B, narrow uterine lumen). We adjusted the injected AH volumes to ~6.5 μl in D0.5 uterine horns and ~4.5 μl in D2.5 & D3.5 uterine horns and ensured that the spreading of the injected blue dye mixed with AH dye to the cervical side could be visualized. Although the final AH concentrations in the injected uterine horns varied depending on the uterine fluid volume in each uterine horn, the pilot results from D0.5 and D2.5 mice indicated that the injection regimen was suitable for detecting AH signals in the uterine epithelium.

To track the time course of AH fluorescence in the uterine luminal epithelium (LE), we chose a middle early pregnancy day, D2.5, and injected AH fluorescent dye into the uterine horns ~11 am on D2.5. The mice were dissected at different intervals from 5 min to 24 h later. To preserve the AH fluorescence for detection, we first fixed the dissected uterine tissues in 4% paraformaldehyde at 4°C for two hours, then two uterine segments from the same uterine horn were processed with or without sucrose immersion for overnight. Although AH green fluorescence was detectable in the LE before and after sucrose treatment, the fine dots (endocytic vesicles) on the apical LE cells could only be distinguished in the sections after sucrose treatment. However, some bright dots in the GE were clearly distinguishable with or without sucrose treatment (data not shown). Therefore, the overnight sucrose treatment is necessary to preserve the fine endocytic vesicles with AH fluorescence, especially in the LE (Fig. 3.1C-1E).

The time course detection of green fluorescence, presumably AH fluorescence, revealed that although the patterns of green fluorescence in different LE regions of the same D2.5 uterine sections varied, the general trend was that LE cells with intense smeared cellular green fluorescence decreased with time, while distinctive green fine cellular dots in the apical side of LE cells generally increased with time from 5 min to 24 h post AH injection. Images from three time points are shown in Figure 3.1C-1E. At 5 min post AH injection, a few LE cells had bright smeared cellular green fluorescence in the whole cell but LE cells with distinctive apical green fine dots were minimal and the number of such dots was also minimal (Fig. 3.1C). At 1 h (Fig. 3.1D) and 24 h (Fig. 3.1E) post AH injection, no LE cells with bright smeared cellular green fluorescence were observed, most LE cells had varied numbers of distinctive green fine dots mainly in their apical side and much less frequently in the basolateral side, and more such fine dots formed a string of punctae in the apical side of LE at 24 h post AH injection (equivalent to

D3.5). This survey reveals that when a D2.5 uterus receives exogenous liquid in the uterine lumen, bulk absorption (seen as bright smeared cellular green fluorescence) diminished with time, while endocytosis (presumably reflected by the distinctive cellular green fine dots) generally increased with time during early pregnancy.

Since the transition of the patterns of green fluorescence (smeared vs. fine dots), reflecting different uterine fluid absorption mechanisms, was already detectable from 5 min to 1 hr after AH injection, we decided on two time points for detecting AH fluorescence: 5 min and 1 h after AH injection, with one uterine horn for each time point so that the time course effects could be evaluated in the same mouse. We also decided to choose two preimplantation time points: D0.5 when the uterine lumen is filled with uterine fluid (Fig. 3.1A) and D3.5 when the uterine fluid is approaching the minimum to prepare for embryo implantation (Fig. 3.1B) [193], for visualizing temporal mechanisms in preimplantation uterine fluid absorption as well as the function of P4 signaling in preimplantation uterine fluid absorption (Fig. 3.1F, 3.1G). P4-deficient *RhoA*$^{f/f}$*Pgr*$^{Cre/+}$ mice [21], exogenous P4-injected *RhoA*$^{f/f}$*Pgr*$^{Cre/+}$ mice, and PR antagonist RU486-treated *RhoA*$^{f/f}$ control mice were employed to investigate P4-PR signaling in the uterine fluid absorption during early pregnancy (Fig. 3.1G).

3.4.2 Detection of AH fluorescence in D0.5 *RhoA*$^{f/f}$ (control) and *RhoA*$^{f/f}$*Pgr*$^{Cre/+}$ uteri

In the D0.5 control uterus, the uterine lumen is filled with uterine fluid, which is drained during dissection and consequently, the LE layer becomes folded because it does not contract as the outer myometrial layer does (Fig. 3.1A). At 5 min post AH injection, the LE layer was highlighted by green AH fluorescence under a lower magnification (Fig. 3.2A); and under a higher magnification, most LE cells were seen to have bright smeared AH fluorescence in the

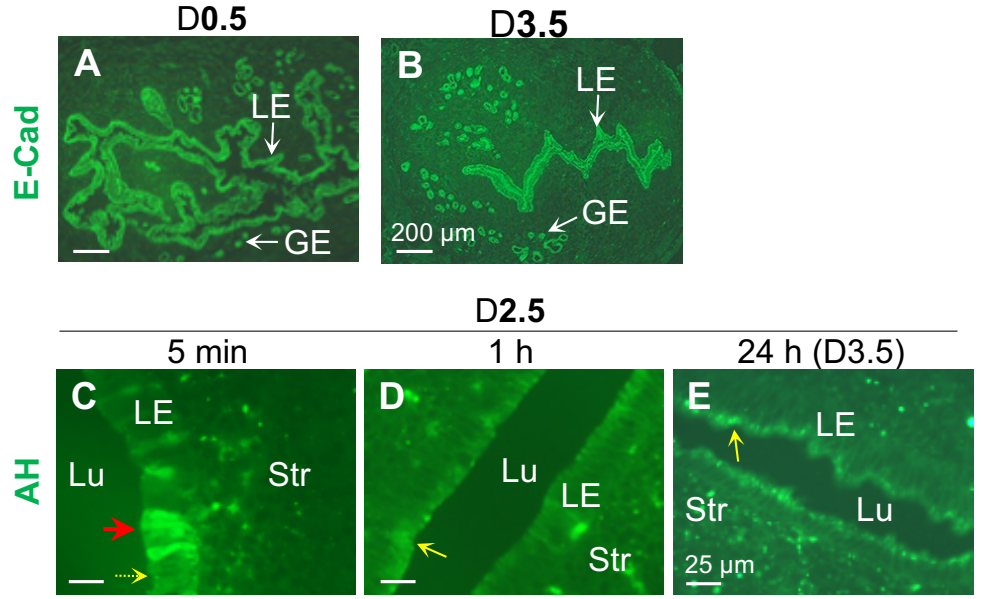

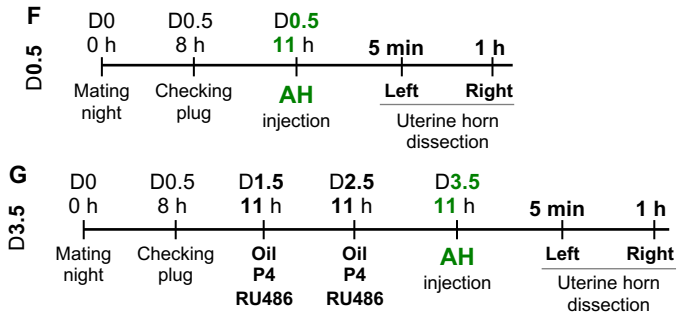

	Oil	P4	RU486
***RhoA*$^{f/f}$** (control)	x	x	x
***RhoA*$^{f/f}$*Pgr*$^{Cre/+}$** (P4 deficiency)	x	x	

Figure 3.1. E-Cad immunofluorescence (A-B), establishment of uterine AH injection and fluorescence detection procedures (C-E), and outline of experimental design (F-G). A & B: E-Cad immunofluorescence in D0.5 (A) and D3.5 (B) mouse uteri to show the dramatic reduction of uterine luminal epithelium (LE), thus uterine lumen and uterine fluid volume, from D0.5 to D3.5. C-E: D2.5 CD-1 mouse uterine horns were injected with AH and dissected 5 min to 24 h after AH injection. C. 5 min. Scattered LE cells (red arrow) with intense diffused AH fluorescence in the whole cell; minimal fluorescent dots (dotted yellow arrow) in apical side of some LE cells. D. 1 h & E. 24 h. No LE cell with intense diffused AH fluorescence in the whole cell; AH fluorescence dots on apical LE. LE, uterine luminal epithelium;

Figure 3.1. (continued) GE, glandular epithelium; Str, stroma; Lu, uterine lumen; red arrow, LE cells with intense diffused AH fluorescence; yellow arrow, clustered AH fluorescence dots on apical LE; dotted yellow arrow, scattered AH fluorescence dots on apical LE; scale bar, 25 μm. F. D0.5. After the identification of a vaginal plug to confirm mating, the mated/plugged *RhoA*$^{f/f}$ (control) and *RhoA*$^{f/f}$*Pgr*$^{Cre/+}$ females were undergoing surgery for AH injection into both uterine horns at ~11 h. The left and right uterine horns were dissected 5 min and 1 h after AH injection, respectively. G. D3.5. The mated/plugged females received one of the treatments (oil, P4, and RU486 (for control mice only)) on both D1.5 and D2.5, with AH injection on D3.5, with the 5 groups summarized in the table below. AH injection and tissue collection were the same as in D0.5 (F).

entire cell (Fig. 3.2A1). However, such bright smeared AH fluorescence in the LE cells was not seen in the GE cells, which had either no visible fluorescence or various sizes and numbers of distinct green dots that could be seen in both apical side and basal side (Fig. 3.2A1), but overall, more appeared to be on the apical side. At 1 h post AH injection, LE cells with intense green fluorescence decreased. There was an individual variation among different mice, two mice had no LE cells with obvious smeared green fluorescence while three mice still had a few segments of the LE layer with intense smeared green fluorescence (Fig. 3.2B). A zoom-in image of an area with transition green fluorescence indicated that the middle part of the LE cells started to show less intensity (Fig. 3.2B1), suggesting that the nucleus had less green fluorescence than that in the cytoplasm. In addition, a few green dots appeared in the apical site of the LE cells that had less intense green fluorescence (Fig. 3.2B1). There was a trend of reduced LE cells with intense smeared green fluorescence from 5 min to 1 h post AH injection in both D0.5 (Fig. 3.2A, 3.2B, 3.4A) and D2.5 uteri (Fig. 3.1C, 3.1D). We have noticed that LE cells with intense smeared

green fluorescence (bulk absorption) usually do not have noticeable green fine dots (endocytosis) in the apical side, and LE cells with multiple green fine dots in the apical side usually do not have intense smeared green fluorescence. The coexistence of green fine dots in the apical side of LE cells and intense smeared green fluorescence is rare and has only been observed in a few LE cells in two uteri of all 7 groups in this study (data not shown). It is possible that the green fine dots are masked by intense smeared green fluorescence.

In the D0.5 *RhoA*$^{f/f}$*Pgr*$^{Cre/+}$ uterus, the uterine lumen was also filled with uterine fluid. At 5 min post AH injection, the green fluorescence in the LE layer (Fig. 3.2C) did not have the overall intensity seen in the control LE layer (Fig. 3.2A) under a lower magnification. A few LE cells were brighter with smeared green fluorescence than the rest of the LE cells (Fig. 3.2C1). Limited green fine dots were visible in the apical site of some LE cells (data not shown). At 1 h post AH injection, most uterine sections did not show LE cells with bright smeared AH fluorescence (Fig. 3.2D) except sections from one uterus that had a few scattered LE cells with less intense smeared green fluorescence (data not shown). A few green dots were present in the apical side of a few LE cells (Fig. 3.2D1), and some could be seen throughout a few LE cells (Fig. 3.2E2). These observations reveal that bulk uterine fluid absorption through the LE was reduced in the D0.5 *RhoA*$^{f/f}$*Pgr*$^{Cre/+}$ uterus but the presence of green fine dots in the apical side of LE appeared to be comparable to those in the control (Fig. 3.2A-2E & Fig. 3.4). Interestingly, we observed a rare phenomenon that a few GE cells had bright smeared AH fluorescence (Fig. 3.2E2, 3.2E3) while the LE cells in the same section only had green dots (Fig. 3.2E1-2E3). This phenomenon was observed in only one D0.5 *RhoA*$^{f/f}$*Pgr*$^{Cre/+}$ uterus among all 7 groups of mice in this study. Since we only examined 2 sections per uterine horn, it is highly possible that we missed detection of this phenomenon in other uterine areas. Regardless, it is reasonable to

conclude that bulk absorption in the GE is not common and is not a major contributing factor to uterine fluid absorption.

In addition to the intense smeared green fluorescence and green fine dots in the uterine epithelium described above, we occasionally observed scattered large and bright dots, which could be infiltrated immune cells, in the LE layer (data not shown); however, we consistently observed green fluorescence, most as clusters of dots with various sizes, in the stromal layer and less in the myometrial layer of all the uterine sections examined and it did not appear to correlate with AH entry into the uterine epithelium, especially bulk entry into the LE. It has been reported that cellular components, such as NADPH and avins, and intracellular organelles including mitochondria and lysosomes, in mammalian cells are autofluorescent (e.g., at 488 nm, the same wavelength for detecting AH fluorescence), and different cells (e.g., immune cells) have different autofluorescence [241-244]. Autofluorescence in preimplantation uteri was examined below.

3.4.3 Detection of uterine autofluorescence

In two intraluminally vehicle-injected D0.5 *RhoA*$^{f/f}$ control uterine sections, we detected similar green fluorescence in the stroma, GE, and myometrium as seen in the AH-injected D0.5 uterine sections (Fig. 3.2F-2K1), indicating autofluorescence in these uterine compartments. On the other hand, none of the LE cells in the vehicle-injected D0.5 control uterine sections had intense smeared green fluorescence (Fig. 3.2F-2K1), confirming that the intense smeared green fluorescence was indeed AH fluorescence (Fig. 3.2A-2C1). However, we also detected autofluorescence in the LE as fine dots that were similar as seen in AH-injected uterine sections (Fig. 3.2G, 3.2J, vs. Fig. 3.2B1, 3.2E2). We also detected scattered large and bright dots (most likely immune cells) in the LE layer as seen in the AH-injected uterus (data not shown, but

similar as in Fig. 3.2M, 3.2P). We also examined two D3.5 *RhoA*$^{f/f}$*Pgr*$^{Cre/+}$ uteri and found similar pattern of autofluorescence as seen in D0.5 control uterine sections (Fig. 3.2F-2K1) except that there appeared to be more green dots on the LE apical side (Fig. 3.2L-2Q1), and 1 h after vehicle injection, a string of apical punctae could be observed in segments of LE layer (Fig. 3.2P), which were also seen in the AH injected D3.5 *RhoA*$^{f/f}$*Pgr*$^{Cre/+}$ uterine sections (Fig. 3.3). In addition, scattered large and bright dots, which were most likely immune cells, in the LE layer (Fig. 3.2M, 3.2P). These data demonstrate extensive autofluorescence in the preimplantation uterine compartments and bulk absorption could be specifically detected by AH dye. It was reported that mitochondria and lysosomes can produce autofluorescence [241], intraluminal markers taken up by endocytosis were channeled into lysosomes in ~D4.5 rat LE [245], and it was apical endocytosis but not apocrine secretion for the accumulation of vesicles accumulated in the apical side of D4.5 rat LE (embryo penetration through LE occurs ~D4 20 h in mice and ~D5 9 h in rats [193]) [246]. We detected LAMP2, a marker of lysosome-associated membranes, as apical punctae in the D3.5 control LE (Fig. 3.2R-2U). These observations support that the autofluorescent green fine dots in the apical LE cells are an indication of apical endocytosis in the LE cells.

3.4.4 Detection of AH fluorescence in D3.5 *RhoA*$^{f/f}$ (control) and *RhoA*$^{f/f}$*Pgr*$^{Cre/+}$ uteri

Unlike D0.5 mouse uterus that is normally filled with uterine fluid (Fig. 3.1A), D3.5 mouse uterus normally has minimal uterine fluid and a narrow uterine lumen (Fig. 3.1B), therefore, the injected AH solution may slightly enlarge the uterine lumen in certain areas. We used oil-injected mice as the vehicle control for the P4-treated and RU486-treated mice in the set of mice on D3.5, which were injected with oil on D1.5 and D2.5 (Fig. 3.1G). In the D3.5 *RhoA*$^{f/f}$

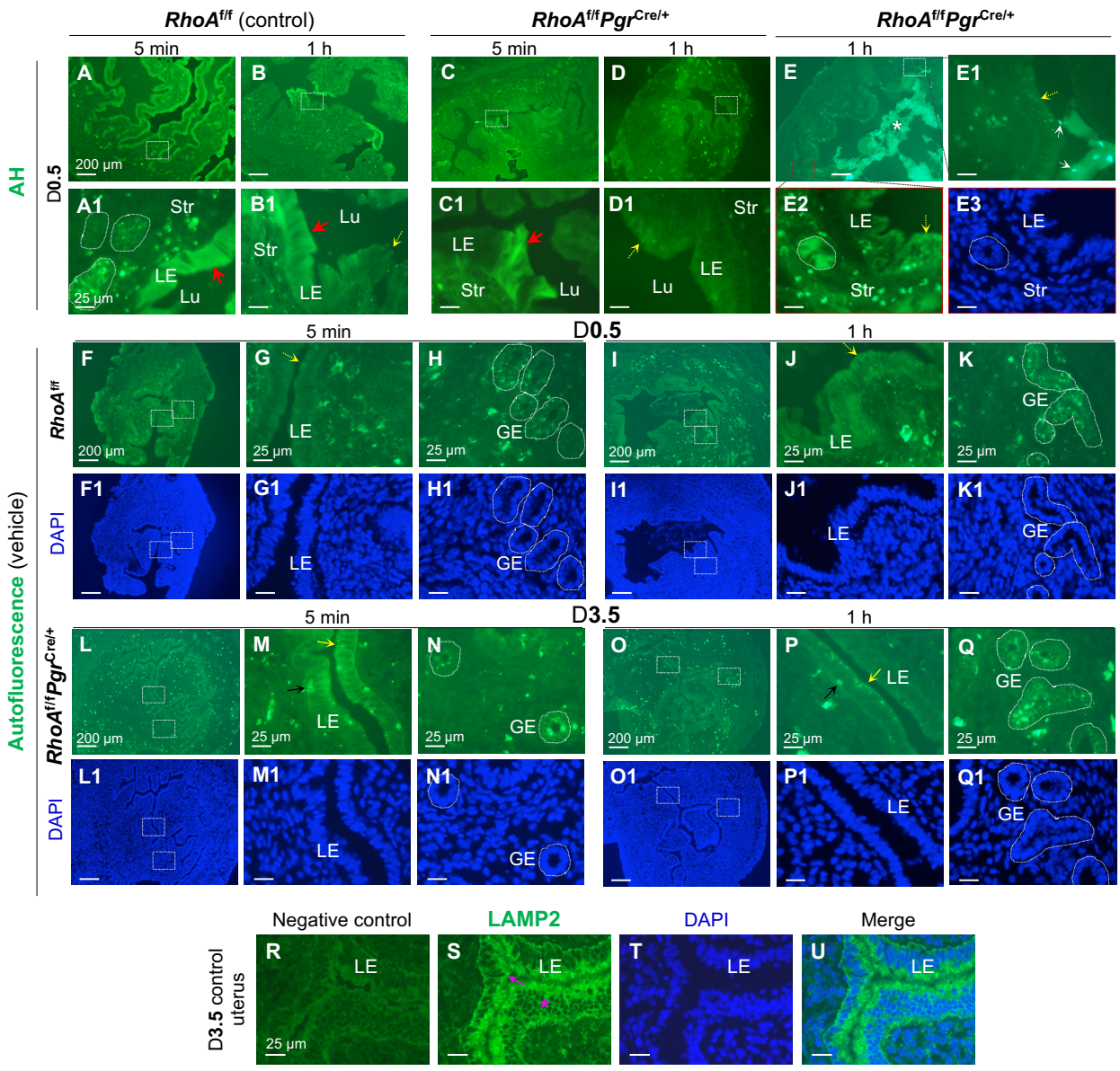

Figure 3.2. AH fluorescence in D0.5 uteri, detection of autofluorescence in D0.5 and D3.5 uteri and LAMP2 in D3.5 uterus. A-E3: from AH-injected D0.5 uteri. A. D0.5 *RhoA*$^{f/f}$ (control) 5 min. B. D0.5 *RhoA*$^{f/f}$ (control) 1 hr. C. D0.5 *RhoA*$^{f/f}$*Pgr*$^{Cre/+}$ 5 min. D. D0.5 *RhoA*$^{f/f}$*Pgr*$^{Cre/+}$ 1 hr. A1-D1, enlarged from the boxed area in A-D, respectively. E. D0.5 *RhoA*$^{f/f}$*Pgr*$^{Cre/+}$ 1 hr to show sperm (white arrows) in the uterine lumen (E1) and a rare observation of bulk entry in some GE (E2). E3, DAPI staining of the same area in E2. White star in E, most likely AH-stained semen. F-K1: from vehicle-injected D0.5 *RhoA*$^{f/f}$ control uteri. F. 5 min post vehicle injection.

Figure 3.2. (continued) I. 1 h post vehicle injection. J & K, enlarged from the boxed areas in I. L-Q1: from a vehicle-injected D3.5 *RhoA*$^{f/f}$*Pgr*$^{Cre/+}$ uterus. L. 5 min post vehicle injection. M & N, enlarged from the boxed areas in L. O. 1 h post vehicle injection. P & Q, enlarged from the boxed areas in O. F1-Q1, DAPI staining of images in F-Q, respectively. A-Q: LE, uterine luminal epithelium; GE, glandular epithelium; Str, stroma; Lu, uterine lumen; red arrow, LE cells with intense diffused AH fluorescence; yellow arrow, clustered AH fluorescence dots on apical LE; dotted yellow arrow, scattered AH fluorescence dots on apical LE; black arrow, most likely infiltrated immune cell; white circle, uterine gland. R-U. Detection of LAMP2 in a D3.5 control uterus. R. Negative control; S. LAMP2; Pink arrow, LAMP2 localization in LE as apical punctae; pink *, because of sectioning angle, single layer LE appeared to be multiple layers. T. DAPI; U. Merged image of LAMP2 and DAPI. scale bar, 200 μm in A-F, F1, I, I1, L, L1, O, O1, and 25 μm in the rest images.

(control) mice, there were patches of and/or scattered LE cells with bright smeared AH fluorescence (Fig. 3.3A, 3.3A1) 5 min post AH injection. At 1 h post AH injection, LE cells with bright smeared AH fluorescence were decreased and most LE cells had AH fluorescent dots in the apical side (Fig. 3.3B, 3.3B1). GE had green fluorescent dots in various sizes and numbers (data not shown).

In the D3.5 *RhoA*$^{f/f}$*Pgr*$^{Cre/+}$ uterus (Fig. 3.3C-3D1), the LE cells with bright smeared AH fluorescence were rarely seen at both 5 min and 1 h post AH injection. Among all sections from 5 mice in this group, only a few scattered LE cells in the uterine sections from three mice at 5 min and one mouse at 1 h post AH injection showed identifiable but not intense smeared AH fluorescence (data not shown). These observations indicate less activity of bulk AH absorption in

the LE from the D3.5 *RhoA*$^{f/f}$*Pgr*$^{Cre/+}$ uterus compared to that in the D3.5 control uterus at the examined time points. However, the LE apical green fine dots in different mice varied and there was no significant difference in the overall level between this group and the the control group (Fig. 3.4B).

3.4.5 Effects of P4 on AH fluorescence in D3.5 *RhoA*$^{f/f}$ (control) and *RhoA*$^{f/f}$*Pgr*$^{Cre/+}$ uteri

Since D3.5 *RhoA*$^{f/f}$*Pgr*$^{Cre/+}$ mice have P4 deficiency [21], we gave exogeneous P4 injections to both *RhoA*$^{f/f}$ (control) and *RhoA*$^{f/f}$*Pgr*$^{Cre/+}$ mice on D1.5 and D2.5 and dissected them on D3.5 (Fig. 3.1G). In the P4-treated D3.5 control mouse uterus, the AH fluorescence detected as bright smeared cellular signal or dot signal at 5 min (Fig. 3.3E, 3.3E1) and 1 h (Fig. 3.3F, 3.3F1) post AH injection was generally comparable to that seen in the oil-injected D3.5 control mouse uterus (Fig. 3.3A-3B1). However, compared to oil-injected D3.5 *RhoA*$^{f/f}$*Pgr*$^{Cre/+}$ mice, P4-treated D3.5 *RhoA*$^{f/f}$*Pgr*$^{Cre/+}$ mice had a narrower uterine lumen and patches of LE cells with bright smeared AH fluorescence in uterine sections from all 5 mice in this group at 5 min post AH injection and 2 mice at 1 h post AH injection (Fig. 3.3G-3H1 and data not shown). The appearances of uterine lumen and the pattens of green fluorescence signals in the LE are generally similar to those in the *RhoA*$^{f/f}$ control mice (Fig. 3.3A-3B1, Fig. 3.3E-3F1, Fig. 3.4B) except an increased percentage of LE cells with bright smeared AH fluorescence 5 min post AH injection (Fig. 3.4A). These results demonstrate that exogenous P4 facilitates uterine fluid absorption in the P4-deficient D3.5 *RhoA*$^{f/f}$*Pgr*$^{Cre/+}$ mice, indicated by the narrower uterine lumen and enhanced bulk absorption. P4 treatment did not seem to have any obvious effect on green fluorescence in the GE cells (data not shown).

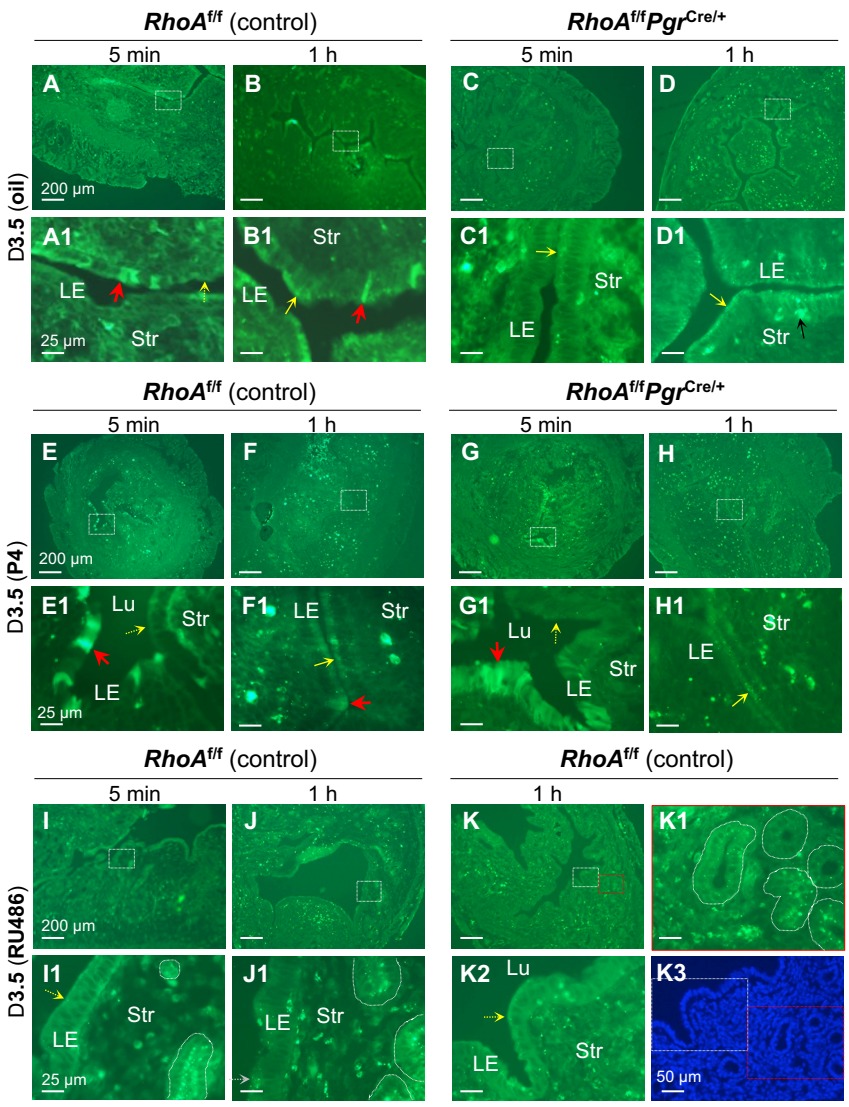

Figure 3.3. AH fluorescence in D3.5 uterus. A. Oil (vehicle)-treated D3.5 *RhoA*$^{f/f}$, 5 min. B. Oil-treated D3.5 *RhoA*$^{f/f}$, 1 h. C. Oil-treated D3.5 *RhoA*$^{f/f}$*Pgr*$^{Cre/+}$, 5 min. D. Oil-treated D3.5 *RhoA*$^{f/f}$*Pgr*$^{Cre/+}$, 1 h. E. P4-treated D3.5 *RhoA*$^{f/f}$, 5 min. F. P4-treated D3.5 *RhoA*$^{f/f}$, 1 h. G. P4-treated D3.5 *RhoA*$^{f/f}$*Pgr*$^{Cre/+}$, 5 min. H. P4-treated D3.5 *RhoA*$^{f/f}$*Pgr*$^{Cre/+}$, 1 h. I. RU486-treated D3.5 *RhoA*$^{f/f}$, 5 min. J. RU486-treated D3.5 *RhoA*$^{f/f}$, 1 h. A1-J1, enlarged from the boxed area in A-J, respectively. K. Another RU486-treated D3.5 *RhoA*$^{f/f}$, 1 h to show the varied AH fluorescent dots in a cluster of uterine glands (K1). K1 and K2, enlarged from the boxed areas in K. K3, DAPI staining covering the areas in K1 and K2. LE, uterine luminal epithelium;

Figure 3.3. (continued) Str, stroma; Lu, uterine lumen; red arrow, LE cells with intense diffused AH fluorescence; yellow arrow, clustered AH fluorescence dots on apical LE; dotted yellow arrow, scattered AH fluorescence dots on apical LE; black arrow, most likely infiltrated immune cell; white circle, uterine gland; scale bar, 200 μm in A-K, 50 μm in K3, and 25 μm in A1-K2.

3.4.6 Effects of RU486 on AH fluorescence in D3.5 *RhoA*$^{f/f}$ (control) uterus

Since P4 mainly acts through progesterone receptor (PR) in the uterus, we also treated *RhoA*$^{f/f}$ control mice with PR antagonist RU486 on D1.5 and D2.5 as a pharmacological loss of function model (Fig. 3.1G). RU486-treated *RhoA*$^{f/f}$ control mice have an enlarged uterine lumen, an indication of uterine fluid retention (Fig. 3.3I-3K). The LE cells lack bright smeared AH fluorescence (Fig. 3.3I1, 3.3J1, 3.3K2), a similar phenotype as seen in oil-treated D3.5 *RhoA*$^{f/f}$*Pgr*$^{Cre/+}$ mice (Fig. 3.3C1, 3.3D1, 3.4A). The GE had various numbers of green fine dots, which were on the apical side of some GEs (Fig. 3.3I1-3J1) but not other GEs (Fig. 3.3K1).

3.4.7 General observations of endocytosis in LE and GE

Overall, there is increased endocytosis, reflected by a string of apical punctae in the LE from 5 min to 1 h post AH injection on D3.5 and from D0.5 to D3.5 LE (Fig. 3.4B). Exogenous P4 and RU486 do not seem to affect this trend (Fig. 3.4B). Among the uterine glands in all uterine sections examined, the numbers and sizes of green dots were varied in different GE cells of the same uterine gland, in different uterine glands of the same uterine sections, and among different uterine samples in the same group. Unlike the green fine dots mainly detected in the apical LE, the green dots in the GE cells were often detected in the basal side also, although

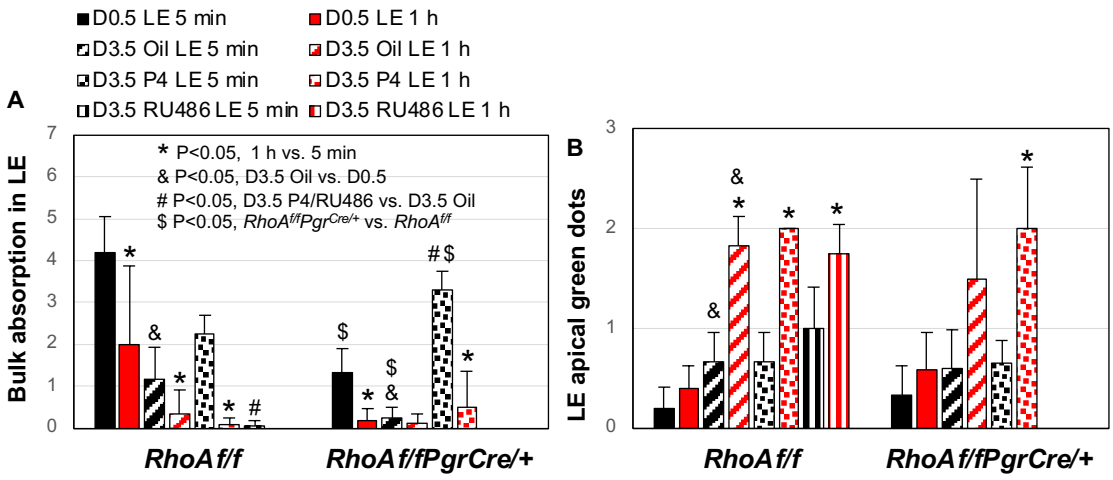

Figure 3.4. Semi-quantification of AH fluorescence indicative of bulk absorption and LE apical green fine dots indicative of endocytosis in LE. A. Bulk absorption in LE. Based on the rough estimation of the percentage of LE segment(s) with discernable smeared cellular AH fluorescence: 5 (>90%, intense), 4 (>50%, intense), 3 (>20%, intense), 2 (>5%, intense), 1 (scattered, intense), 0.5 (scattered, not intense), and 0. B. LE apical green dots indicative of endocytosis in LE. Based on the estimation of the percentage of LE cells with distinctive cellular AH fluorescent dots forming a string of apical punctae: 3 (>90%), 2 (>50), 1 (>5%), 0.5 (scattered), and 0 (nondiscernable). Error bar, standard deviation; * P<0.05, 1 h vs. 5 min, paired two-tailed student t-test; & P<0.05, D3.5 Oil vs. D0.5; # P<0.05, D3.5 P4/RU486 vs. D3.5 Oil; $ P<0.05, *RhoA*$^{f/f}$ vs. *RhoA*$^{f/f}$*Pgr*$^{Cre/+}$ for the same parameter; &, #, $, ranking coupled with two-tailed unequal variance student t-test; N=3-5.

overall more seemed to be in the apical side. There was a lack of consistent difference in the green dots, in the GE cells among all 7 groups, suggesting that endocytosis in the GE is not sensitive to the changes in early pregnancy environment and P4-PR signaling. Therefore, the contribution of GE in preimplantation uterine fluid absorption is minimal.

3.4.8 Expression of ATP1A1 in preimplantation uterus

Because of the expected role of ENaC in Na^+ absorption from the uterine lumen to generate an osmotic gradient for uterine fluid absorption [46, 51, 207], and the expected role of aquaporins to facilitate water absorption in response to the osmotic gradient generated by Na^+ absorption, we attempted to immunodetect ENaCα, ENaCβ, and ENaCγ, the three subunits for ENaC, as well as AQP4 and AQP5, the two aquaporins that were convincingly detected using *in situ* hybridization in the preimplantation mouse uterine epithelium [231], in the uterine tissues from all 7 groups to correlate their localizations in the uterine epithelium with uterine fluid volumes and uterine fluid absorption. After testing multiple commercially available antibodies for ENaC subunits, only one anti-ENaCγ antibody gave seemingly specific signals, which showed largely similar uterine expression patterns to those revealed by anti-AQP4 and anti-AQP5 antibodies in serial uterine sections from the 7 groups (data not shown). However, based on the limited reliable information of uterine expression and regulation of these three genes (mRNA/protein) in the literature and our unpublished mRNA profiling data, ENaCγ, AQP4, and AQP5 are expected to have different spatiotemporal expression patterns in the preimplantation mouse uterus. We are not confident on the immunohistochemistry data of ENaCγ, AQP4, and AQP5, and only present the immunofluorescence data of ATP1A1.

Our microarray data revealed ATP1A1 as the dominant α subunit of Na^+/K^+ ATPase in the LE (GSE44451) [37]. Na^+/K^+ ATPase localized on the basolateral membrane pumps apically absorbed Na^+ ions out of the epithelial cell into subepithelial space to maintain intracellular Na^+ homeostasis [225, 226]. ATP1A1 was mainly detected in the basolateral membrane of LE and GE (Fig. 3.5). There seemed to be no obvious difference in the overall ATP1A1 staining between control and *RhoA*$^{f/f}$*Pgr*$^{Cre/+}$ LE and GE on D0.5 (Fig. 3.5A-5B2). In the D3.5 control uterus, P4

treatment did not have an obvious effect on ATP1A1 staining in the LE and GE (Fig. 3.5C-5C2, 3.5E-5E2). However, RU486 treatment reduced ATP1A1 staining, mainly in the LE, especially the lateral membrane, but not obvious in the GE, of the D3.5 control uterus (Fig. 3.5G-5G2). In the D3.5 *RhoA*$^{f/f}$*Pgr*$^{Cre/+}$ uterus, P4 treatment increased ATP1A1 expression in the LE but not in the GE (Fig. 3.5D-5D2, 5F-5F2), which was consistent with increased bulk absorption in the LE upon P4 treatment (Fig. 3.3G, 3.3G1) and with a report of upregulation of ATP1A1 in the LE of P4-treated ovariectomized rats [247].

3.5 Discussion

We initially intended to use Alexa Fluor™ 488 Hydrazide (AH) for tracing uterine fluid absorption via endocytosis during early pregnancy. However, when we tested AH in a D0.5 mouse uterus, we were surprised to see a bright LE layer with smeared green fluorescence. With more pilot experiments, we concluded that it was not an artifact. Considering AH being a small-sized and water-soluble molecule and the osmotic gradient generated by the absorption of Na^+, the dominant electrolyte in the uterine fluid promoted by P4 treatment [46, 207], it is reasonable to speculate that AH can enter LE cells from the uterine lumen with water through the osmotic gradient. Therefore, AH can be visualized as smeared green fluorescence in the cytoplasm, which is in contrast to AH entry via endocytosis expected to be seen as green fine dots. Although the molecular mechanisms for bulk entry of AH into the LE cells remain to be investigated, mechanisms for water movement through mammalian plasma membrane driven by osmotic gradients could involve: 1) water diffusion through the lipid bilayer with limited capacity,

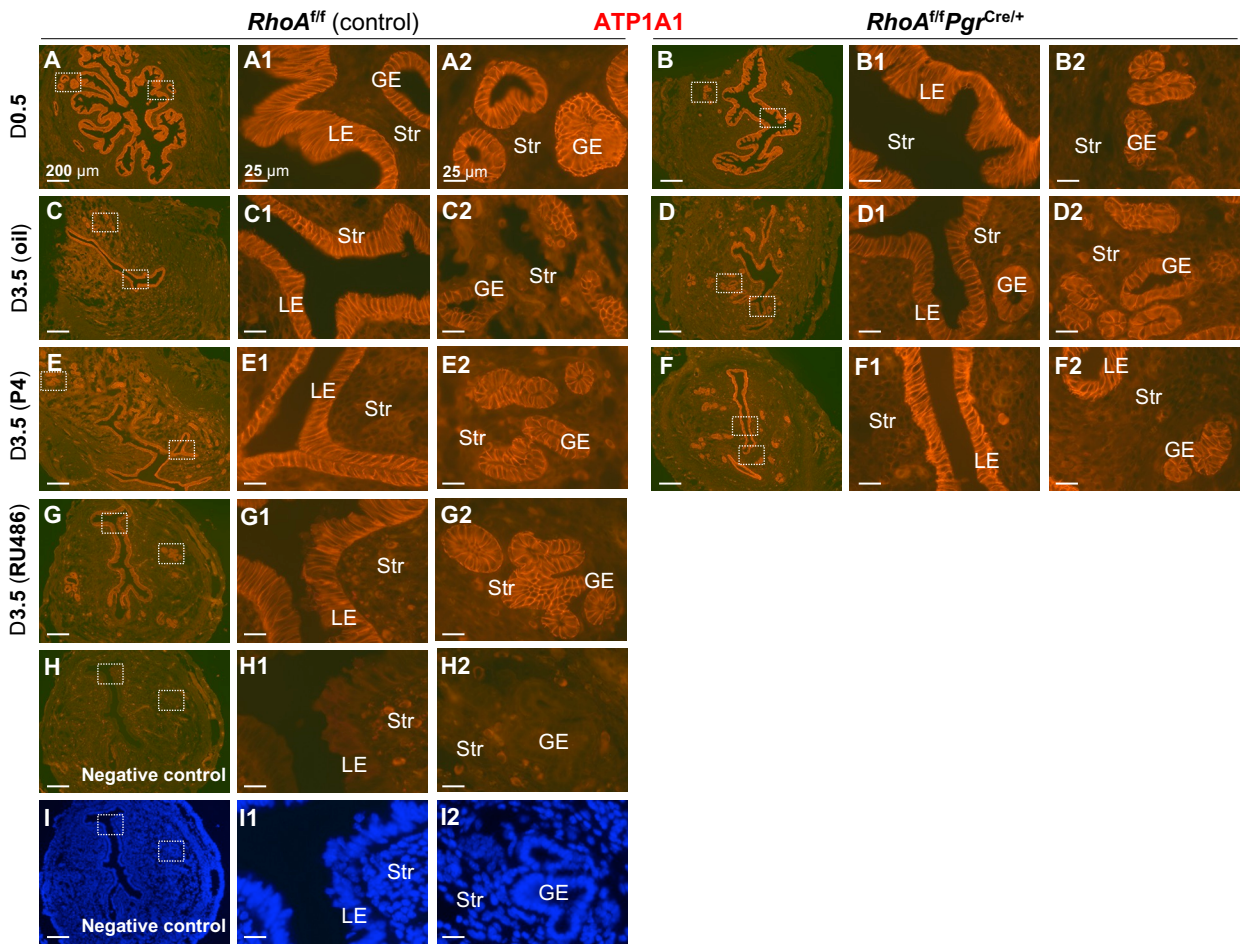

Figure 3.5. Detection of ATP1A1 using immunofluorescence. A. D0.5 *RhoA*$^{f/f}$ (control). B. D0.5 *RhoA*$^{f/f}$*Pgr*$^{Cre/+}$. C. Oil (vehicle)-treated D3.5 *RhoA*$^{f/f}$. D. Oil-treated D3.5 *RhoA*$^{f/f}$*Pgr*$^{Cre/+}$. E. P4-treated D3.5 *RhoA*$^{f/f}$. F. P4-treated D3.5 *RhoA*$^{f/f}$*Pgr*$^{Cre/+}$. G. RU486-treated D3.5 D3.5 *RhoA*$^{f/f}$. H. Negative control, RU486-treated D3.5 *RhoA*$^{f/f}$. I. DAPI staining of the section in H. A1-I1 with focus on LE and A2-I2 with focus on GE, enlarged from the boxed area in A-J, respectively. LE, uterine luminal epithelium; GE, glandular epithelium; Str, stroma; scale bar, 200 µm in A-I, and 25 µm in A1-I2.

2) water passage through AQPs, and 3) passive water transport through cotransporters. In addition, some cotransporters could also conduct active water transport along with their transported solutes independent of the osmotic gradient [248-250].

Since the first report of dynamic uterine fluid volume during estrous cycle in rats [206], seminal studies have established the dominant roles of E2 in promoting uterine fluid accumulation and P4 in promoting uterine fluid absorption [46, 51, 207-211]. There were controversial reports about how uterine fluid disappeared upon P4 treatment, via leakage through the cervix or absorption through the uterine epithelium (reviewed in [46]). One well-controlled study firmly established uterine epithelium as the surface for uterine fluid absorption, in which the ligated (at both the ovarian and cervical ends to prevent uterine fluid leakage) and non-ligated uterine horns in the same ovariectomized rats had similar reduction of uterine fluid upon P4 treatment [46].

Uterine epithelium includes luminal epithelium (LE) and glandular epithelium (GE), which extends from LE into the underlying stromal layer. Because of the secretory nature of a gland, it is generally expected that GE may have a preferred role in uterine fluid secretion and LE may play a more important role in uterine fluid absorption. Studies from cultured mouse uterine epithelium (most likely dominated by LE based on the isolation procedure) demonstrated the ability of these epithelial cells in absorption of Na^+ and secretion of Cl^- [251, 252]. Studies from cultured human glandular epithelial cells demonstrated the abilities of ion transport and amiloride-sensitive Na^+ conductance in these cells [49, 253, 254]. Avian uterine (shell gland) epithelium is also capable of transporting Na^+ and anions and amiloride could inhibit Na^+ absorption, indicating the involvement of ENaC [255]. These *in vitro* and *ex vivo* studies support uterine epithelium as the uterine fluid absorption surface involving the movements of

electrolytes. However, the contributions of LE and GE in uterine fluid absorption *in vivo* during early pregnancy remain unclear.

Our study using intraluminally injected AH clearly demonstrates that, in the control mice, the LE layer plays a dominant role in bulk absorption of uterine fluid, which is reflected by bright smeared AH fluorescence in the LE cells 5 min post AH injection. On D0.5, the uterine fluid volume is maximum under the influence of preovulatory E2. The uterine fluid volume reduces dramatically from D0.5 to D1.5 based on the reduction of LE folding and drops to minimum approaching embryo attachment on ~D4.0 [193]. On D0.5, LE cells have extensive bulk absorption 5 min post AH injection, which is reduced on D3.5. Interestingly, intense bulk absorption on D3.5 is only observed in a segment of LE cells or scattered LE cells. One possible explanation is that different LE cells have different expression levels of the genes critical for bulk absorption, such as ENaC subunits and aquaporins, and the LE cells with stronger molecular equipment for generating an osmotic gradient will be selected for taking the role of bulk absorption when the demand for bulk absorption is limited due to the minimal uterine fluid on D3.5.

Since we evaluate bulk absorption based on the intensity of smeared AH green fluorescence relative to its surrounding, we can be sure of bulk absorption when LE cells have bright smeared AH fluorescence. However, we cannot be sure of lack of bulk absorption if the LE cells do not have bright smeared AH fluorescence 5 min post AH injection, because it is most likely that bulk absorption in the LE is not strong or efficient enough to take up sufficient AH dye to make it much brighter than the surrounding. If there is a significant reduction of LE cells with bright smeared AH fluorescence 1 h post AH injection compared to 5 min post AH injection in the same mouse, one possible explanation is that bulk absorption via LE cells is still strong but

there is insufficient AH dye available in the uterine lumen to be absorbed and to subsequently fluoresce the LE cells. However, this might not be a main contributing factor because strong bulk absorption remains detectable at 1 h in a few D0.5 control uteri. Another potential explanation is that amiloride-sensitive ENaC, which is shown to be essential for P4-induced uterine fluid absorption in a uterine perfusion study [51], can be activated by shear flow [256-258], which is expected to be enhanced by intraluminal AH injection and diminishes with time, e.g., stronger at 5 min than 1 h post AH injection.

In preimplantation mice, P4 levels rise shortly after copulation [236-238]. Two studies reported that plasma P4 levels quickly reached the early pregnancy plateau level ~D2.5 [236, 237], one study indicated plateauing time at ~D3.5 [238], and another study showed it at ~D4.5 [259]. This last report was questionable because plasm P4 levels was shown a trend of decreasing from D0.5 to D1.5 before increasing thereafter [259]. Our study demonstrates that P4 signaling promotes bulk absorption in the preimplantation LE even though the extent of bulk absorption in the LE in the control mice is seemingly inversely correlated with the rising of preimplantation P4 levels. We previously demonstrated that $RhoA^{f/f}Pgr^{Cre/+}$ mice were infertile with P4 deficiency [21]. Reduced bulk absorption is observed in the $RhoA^{f/f}Pgr^{Cre/+}$ mice both on D0.5 and D3.5. RhoA could activate ENaC [260, 261]. The reduced bulk absorption in the $RhoA^{f/f}Pgr^{Cre/+}$ LE might be contributed by RhoA deficiency in the LE and impaired corpus luteum function in P4 synthesis in the $RhoA^{f/f}Pgr^{Cre/+}$ mice. The role of P4 signaling in promoting bulk absorption of uterine fluid is confirmed in P4-treated $RhoA^{f/f}Pgr^{Cre/+}$ mice, which have increased LE cells with bright smeared AH fluorescence compared to oil-treated $RhoA^{f/f}Pgr^{Cre/+}$ mice. On the other hand, since P4 function is mainly mediated by PR, PR antagonist RU486 inhibits bulk absorption of uterine fluid in the LE of D3.5 control mice,

further supporting a positive role of P4 signaling in promoting uterine fluid absorption. However, bulk absorption is decreased from D0.5 to D3.5. This finding seemingly contradicts the observations that P4 levels increase from D0.5 to D3.5 and P4 induces uterine fluid absorption. The difference between D0.5 and D3.5 in bulk absorption via LE may reflect the need for bulk absorption because the D0.5 uterus is filled up with uterine fluid while the D3.5 uterus has minimal uterine fluid. On the other hand, the large volume of uterine fluid on D0.5 will create a hydraulic pressure on the apical membrane of the LE. Hydraulic pressure and osmotic pressure are driving forces for water movement in the cell [262]. The flow of uterine fluid can induce shear flow to activate ENaC on epithelial apical membrane [256-258]. Therefore, it is reasonable to speculate that the hydraulic pressure and osmotic pressure could both contribute to the extensive bulk entry of uterine fluid on D0.5. Our AH tracking approach in this study could not trace the exit mechanisms of the absorbed uterine fluid in the LE. Based on bulk absorption of water along the osmotic gradient from the uterine lumen, and the expected exit of Na^+ to the subepithelial area via Na^+/K^+ ATPase will generate an osmotic gradient across LE basal membrane to facilitate water exit to the subepithelial area.

Our study using intraluminally injected AH seemingly reveals endocytosis in D3.5 LE, visualized as green fine dots in the apical LE. However, our further study demonstrates that these green fine dots in the apical LE are autofluorescent. Therefore, the intraluminally-injected AH dye could not specifically trace active apical endocytic activity in the LE. One study used intraluminally injected horseradish peroxidase (HRP) to trace apical endocytosis in the D0.5 mouse uterus but failed to detect any endocytosis of HRP [101]. We could detect scattered green fine dots in the apical side of a few LE cells of some D0.5 uterine samples but not all, however, we could not be sure if they were vesicles with active endocytic activity. In the D3.5 LE, there is

a trend of more dots from 5 min to 1 h post AH injection, which is opposite of bulk absorption. Based on the literature that rat LE cells approaching embryo implantation time are active in apical endocytosis (but not apocrine secretion) that channels into lysosomes [245, 246] and our detection of LAMP2, a marker of lysosome-associated membranes, as a string of apical punctae in the D3.5 LE right prior to embryo implantation initiation in mice [193], we are confident that the strings of green fine dots in the D3.5 apical LE are reflecting increased LE apical endocytic activity from that on D0.5.

LE apical endocytosis is minimal on D0.5 when the maximal uterine fluid reduction occurs accompanied with maximal bulk absorption, this unequivocally places bulk absorption via LE as the dominant mechanism for uterine fluid reduction on D0.5. Endocytosis in LE is increased from D0.5 to D3.5. This change may reflect the functional needs on these respective early pregnancy days. On early D0.5 (shortly post coitum), the uterine fluid serves as a passage to facilitate sperm transport to the oviduct for fertilization. On D3.5, there is minimal uterine fluid, therefore, the requirement for bulk absorption of uterine fluid is reduced; on the other hand, the embryo in the D3.5 uterus is preparing for embryo implantation, which initiates ~D4.0 in mice. One prerequisite for embryo implantation is the mutual communications between the embryo and the uterus to ensure the synchronized readiness of both the embryo and the uterus for embryo implantation [8, 193]. Endocytosis can internalize various molecules, including messenger molecules, which are expected to facilitate embryo-uterus communications for embryo implantation. Prior to embryo attachment (~D4.0 in mice) [239], there are protrusions (pinopods/uterodomes) appearing on apical LE, coincident with a brief period of intense endocytic activity at the time of embryo implantation [232, 246, 263]. In ovariectomized rats, P4 promotes uterine lumen closure and endocytosis [264]. These previous reports consistently

demonstrated the critical role of P4 in apical LE endocytosis. Our study using intraluminally injected AH shows that LE apical endocytosis is increased from D0.5 to D3.5, which is correlated with the increased P4 levels during preimplantation. However, P4 treatment and RU486 treatment (on D1.5 and D2.5) do not seem to have obvious and consistent effects on the LE apical endocytosis detected on D3.5. It is unclear if it is because of the 24+ h between the last treatment and AH detection that missed the best time for detecting the effect on endocytosis, or unlike ovariectomy, our experimental setting with intact ovaries during early pregnancy was not sensitive enough to detect the effects of exogenous P4 treatment and RU486 treatment on LE apical endocytosis.

Based on our observations, the contribution of GE on uterine fluid absorption is minimal for the following reasons: First, the GEs are folds from LE into the stromal layer. Unless there is a suction system to draw the uterine fluid from the uterine lumen to the glandular lumen, the direct contact surface of GE to the bulk of uterine fluid is limited. Second, bulk absorption of uterine fluid in GE is rare on both D0.5 and D3.5. One potential reason could be that the volume of uterine fluid in the lumen of the uterine gland is insufficient for a need of bulk absorption. Third, although the presence of green dots varies greatly among different GEs in the same uterine sections or in the uterine sections from different mice in the same treatment groups, the green dots are present in some GEs of all the uterine samples examined. Since both mitochondria and lysosomes are autofluorescent [241], and the green dots in the GEs vary in sizes and cellular localization, we could not differentiate any of the green dots in GE cells to be endocytic vesicle. However, there is no obvious and consistent effect/evidence of P4 signaling on the abundance and cellular distribution of the green dots in the GEs despite the observations of P4-induced uterine fluid absorption in the *RhoA*$^{f/f}$*Pgr*$^{Cre/+}$ mice with P4 deficiency and RU486-induced

uterine fluid accumulation in the *RhoA*$^{f/f}$ control mice. Interestingly, it was reported that in ovariectomized rat GE cells, the number of basal pinocytotic invaginations was relatively small and unresponsive to P4 stimulation [208]. These observations suggest that apical and basal endocytosis (including pinocytosis) in GE cells might be not regulated by P4 signaling, further demonstrating that LE and GE have different functions and regulatory mechanisms in uterine fluid absorption.

In summary, this study establishes a straightforward approach to simultaneously visualize bulk entry (directly) and endocytosis (somewhat indirectly) of uterine fluid absorption during early pregnancy. It reveals the temporal mechanisms of preimplantation uterine fluid absorption, with bulk absorption in the LE reduces from D0.5 to D3.5 while endocytosis in the LE increases from D0.5 to D3.5, as well as the suppressive effects of P4 deficiency and RU486 on bulk absorption in the LE during early pregnancy. This study also demonstrates the dominant role of LE but not GE in preimplantation uterine fluid absorption. The molecular mechanisms for preimplantation uterine fluid absorption remain to be elucidated.

Acknowledgements

The authors thank the Office of the Vice President for Research, Interdisciplinary Toxicology Program, and Department of Physiology and Pharmacology at the University of Georgia, the National Institutes of Health (NIH R03 HD100652 and R03HD097384 to XY), and Ferring Pharmaceuticals (via a Ferring Innovation Grant) for financial support.

CHAPTER 4

THE EFFECTS OF INFLUENZA A INFECTION ON CYCLING FEMALE MICE[3]

[3]Li, Y., Hancock, J.M., Martin, T.E., Latha, K., Fahey, D., Zhan, T., Xiao, S., Watford, W., and Ye, X. To be submitted to *Biology of Reproduction*.

4.1 Abstract

Influenza (flu) is a contagious respiratory disease caused by influenza viruses which every year can results in about 1 billion infection cases with 3 to 5 million severe cases and ~0.6 million related deaths globally. Influenza A virus (IAV) is the only type of influenza can cause flu pandemic, and its subtypes H1N1 and H3N2 are the most circulating IAVs in human. Women in reproductive ages are at higher risks of developing severe complications after IAV infection. The effects of IAV infection in female reproduction have been mostly studied during the pregnancy, which can cause more severe diseases in pregnant women associated with increasing chances of adverse pregnancy outcomes. The current knowledge gap is how IAV can affect female in the reproductive cycle. In this study, we used mouse as our model to study the effects of mouse-adapted H3N2 IAV in female reproductive system of cycling female mice. Female mice suffered with body weight decrease and lung inflammation after IAV infection. They also had arrested estrous cycle in the quiescent stage, diestrus, coupled with a trend of increased number of ovarian follicles in early developmental stages. The overall histology and cellular activities in ovary and uterus from infected mice were comparable to the uninfected mice in the diestrus stage.

4.2 Introduction

Influenza (flu) is a contagious respiratory disease caused by influenza viruses with characteristic symptoms including cough, fever/chills, headache, sore throat, runny nose, fatigue, muscle pain and etc [124]. According to the World Health Organization (WHO), it is estimated that influenza outbreaks can affect about 1 billion people, with 3 to 5 million severe cases and ~0.6 million related deaths annually [124]. Especially as the relaxation of COVID-19 restrictions have

implemented globally, the modelling studies predict the upcoming increase of influenza burden across the globe in the post COVID-19 pandemic era [265-267]. Among the 4 types of influenza viruses (A, B, C, and D), influenza A viruses (IAV) is the only know type can cause pandemic [268, 269]. The IAV can be categorized, based on its surface antigen glycoproteins haemagglutinin (HA) and neuraminidase (NA), into 16 HA and 9 NA subtypes with the nomenclature of H(x)N(y) [270]. The H3N2 and H1N1 are currently the two most circulating IAV in human for seasonal and pandemic influenza, respectively [268]. Although the emergence of H3N2 pandemic in human was five decades later than H1N1, the cumulative impact of H3N2 over the past 50 years, made it the predominant cause for influenza burden in the 21st century [271, 272]. The vaccination can reduce the chances of severe diseases after IAV infection, however, the effectiveness against H3N2 is suboptimal compared to other IAV subtypes, due to its fast antigenic drift, egg-adaptive mutations, and immunological imprints on middle-aged generations [271, 273-277]. The current golden standard treatments for IAV infection, adamantanes and NA inhibitors (NAI), are targeting the surface protein M2 and NA on IAV to inhibit the viral entry and release [129, 130, 278]. However, the high mutation rates of H3N2 has developed the resistant to over 90% of adamantanes treatments, with a growing concern for the efficiency of NAI treatments [278].

Compared to males, females in reproductive ages (18-49 years of ages in human) have greater risks for developing severe outcomes after IAV infection [148, 149, 154, 279]. However, at younger ages prior to puberty and older ages after 50s, the trend is reversed in which men are more vulnerable to IAV infection [280]. Although pregnancy is a well-distinguished risk factor, identified by WHO, for severe complications from IAV infection [164, 165], itself cannot explain the female preponderance of severe IAV outcomes [149, 154]. Except pregnancy, the major reproductive status for women in reproductive ages is in the menstrual cycle. A regular menstrual

cyclicity in women increases the chance of successful pregnancy outcomes [281-283]. Similar to menstrual cycle in women, female mice have estrous cycle which contains 4 stages: proestrus, estrus, metestrus, and diestrus, and the total length of estrous cycle is around 4-7 days [284, 285]. Even though many researches from both human and mouse models studying IAV infection during pregnancy, especially the infection during mid-late gestation [162-175], only one study briefly mentioned the disrupted estrous cycle in mice after mouse-adapted H1N1 infection without further investigation into the effects in the female reproductive system or extension of the study into other subtypes of IAV like H3N2 [286]. Concerning evidence from the COVID-19 pandemic detected prolonged menstrual cycles after COVID-19 infection and vaccination [287-290], which indicates a global pattern of the disrupted female cyclicity after severe respiratory viral infection. Th current knowledge gap and the growing concern is whether and how the female cyclicity can be affected after IAV infection.

To understand the effects of IAV infection, especially the profound H3N2 IAV, on female cyclicity, we nasally infected virgin C57BL/6J female mice with mouse-adapted H3N2 IAV (x31, at the dose of 10^4 pfu) and compared their estrous cyclicity to their vehicle-treated littermate females. Body weight changes and pathogenesis in the lung were compared and analyzed to confirm the effectiveness of our nasal infection. As for the IAV effects on reproductive system, ovarian and uterine samples from the same estrous stages of infected and non-infected females were analyzed for investigation.

4.3 Materials and Methods

Mice and Viruses. C57BL/6J mice were purchased from the Jackson Laboratory, maintained, and bred in the Coverdell animal facility at the University of Georgia. Coverdell

animal facility is on a 12-hour light/dark cycle (6:00 to 18:00) at 23°C ± 1°C with 50% relative humidity. All mice had free access to regular chow 5053 (Labdiet, St. Louis, MO, USA) and water. All methods used in this study were approved by the University of Georgia IACUC Committee (Institutional Animal Care and Use Committee) and conform to National Institutes of Health guidelines and public law. Influenza virus A/HKx31 (H3N2; hereafter x31) stocks were prepared from Dr. Watford's lab at the University of Georgia as previously described [291].

Influenza infection and tissue collection. Virgin female littermates at ~6 weeks old were checked for estrous cyclicity by vaginal smear for 7 days prior to the treatment. All the mice in this study had normal cyclicity before the infection. At ~7 weeks old, female littermates were randomly assigned into vehicle control group (PBS treatment) or infection group (x31 infection), N=15/group. They were anesthetized with 250 mg/kg of 2% weight/volume Avertin (2,2,2-Tribromoethanol, Sigma) followed by intranasal instillation of 50 µl PBS or 10^4 pfu of x31 at ~10:00AM as previously used [291]. The infection day is designated as 0 days post infection (0 dpi). We continuously recorded their estrous cyclicity and body weight changes from 0 dpi to 7 dpi. At 7 dpi, mice were anesthetized with isoflurane (Patterson Veterinary Supply, 07-893-1389) inhalation at ~10:00AM for blood collection via orbital sinus. The mice were then euthanized by cervical dislocation. Left side of lung, ovary, oviduct, and ~1/3 of the uterotubal side of the uterine horn were fixed in 10% formalin (VWR, 16004-126); the other side of the lung, ovary, oviduct, and the rest of the uterine horn were flash frozen. Since the majority of the infected mice stayed in the diestrus stage at 7 dpi, we collected another set of mice from the diestrus stage after PBS treatment (N=6) to dissect the IAV effects on reproductive system from the sexual hormonal effects. Another set of x31-infected mice (N=6) were dissected at 28 dpi to study the estrous cyclicity change after body weight recovery.

Vaginal smear for mouse estrous cycle staging. Estrus cycle was monitored daily by flushing the vagina of mice with 50 µl sterile PBS and checking the flushed vaginal cell types under the microscope for estrous cycle staging as previously described [197, 285].

H&E staining. Lung, ovary, and uterus samples were fixed in 10% neutral buffered formalin for 48 hours and then kept in 70% ethanol at 4°C until dehydration. Samples were dehydrated and embedded in paraffin. 5 µm paraffin sections from each sample were collected, processed, and stained with Hematoxylin (Sigma, SLCC1853) and Eosin (Sigma, SLCC5587) as previously described [292].

Immunohistochemistry. Paraffin sections (5 µm) of lung, ovary and uterus samples from vehicle control (PBS) and x31 groups were incubated with PCNA (1:200, Cell Signaling, D3H8P), CD45 (1:400, Cell Signaling, D3F8Q), and cleaved caspase 3 (1:200, Cell Signaling, 9661) respectively at 4°C overnight. On the second day, the slides were incubated with biotinylated goat anti-rabbit IgG antibody (1:1000, Vector lab, BA-1000) for 1h at room temperature, and the signals were developed by DAB substrate kit (Vector lab, SK-4100). The nuclei were counter-stained by Hematoxylin solution. Negative controls were processed together without the primary antibody. Images were captured by Carl Zeiss imaging system with an AxioCam MRc5 digital camera. The CD45 immunohistochemistry staining in the lung were quantified using ImageJ (Java 8) [293]. The immunohistochemistry staining in the ovary were quantified as the percentage of follicles with positive staining in each sample and compared between the treatments.

Ovarian follicle and corpus luteum (CL) counts. Ovarian sections from H&E staining and immunohistochemistry from uninfected diestrus control (N=6) and x31-infected diestrus females (N=7) were independently examined by two individuals for the numbers of different

developmental stages of follicles and CLs on each section (sections N>2/sample). The counts were averaged for the number of follicles and CLs of each sample and treatment group.

Statistical analysis. Data are presented as mean ± SD where applicable. Chi-square test was used to compare the estrous cyclicity between the treatment groups. Two-tail unequal variance student's t-test was used to compare the body weight at the same dpi and the positive staining from immunohistochemistry. Two-way ANOVA with replication was used to compare the body weight changes from 0 to 7 dpi between different treatments.

4.4 Results

4.4.1 H3N2 IAV infection results in body weight loss in C57BL6/J female mice

To study the effects of IAV infection on female estrous cyclicity, we nasally infected C57BL6/J with normal reproductive cyclicity (monitored by daily vaginal smear for at least 1 week before the infection, data not shown & Fig. 4.2B) with a low pathogenic mouse-adapted H3N2 IAV strain (x31) and compared them with vehicle-treated (PBS) littermates control mice for 7 days post infection (7 dpi, N=15/group). C57BL6/J mice used in this study were all between 6.8-7.8 weeks of age at the time of infection (0 dpi) and they had comparable body weights before the treatment (Figure 4.1A): the control mice had an average weight of 18.1±1.3 g and infected mice had an average weight of 18.0±0.8 g ($p=0.81$) at 0 dpi. However, mice from x31 IAV infection showed a significantly body weight reduction from 2 dpi ($p<0.001$) and showed a continuous body weight loss up to 25.6% at the dissection time (7 dpi) (Figure 4.1 A&B). The pattern of body

weight loss in x31-infected females is consistent with previous data, which indicates the efficiency of our nasal infection [291].

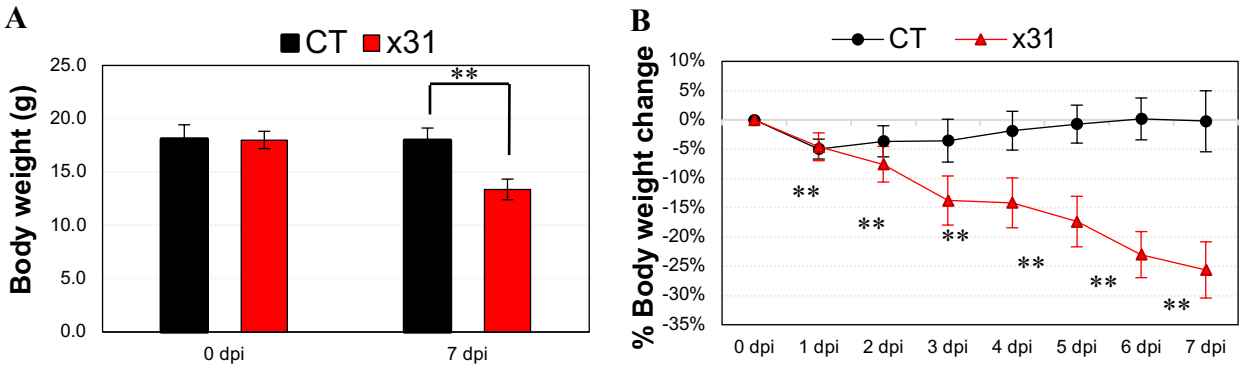

Figure 4.1. Body weight change before (0 dpi) and after (7 dpi) IAV infection. A. Body weight before infection (0 dpi) and at dissection (7 dpi). **p<0.001 two-tail unequal variance t-test. B. Percentage body weight change from 0 dpi to 7 dpi. **p<0.001 two-tail unequal variance t-test at each dpi; **p<0.001 Two-way ANOVA with replication for overall comparison on body weight change after infection between the two treatments; Error bar: standard deviation. dpi: days post infection; CT: vehicle control treated female mice; x31: mouse-adapted H3N2 influenza-infected female mice. N=15/group.

4.4.2 H3N2-infected female mice have disrupted estrous cycle

Estrous cyclicity is established after puberty onset, which is before ~5 weeks old in C57BL6/J female mice [197]. The 4 different stages of estrous cycle are corresponding to the 2 out of the 3 menstrual stages in women: the proestrus and estrus stages are similar to human follicular stage, which featured with a rise in circulating estrogen level (E2) and ovulation as active reproductive phases; and the metestrus and diestrus stages are homologous to early and late secretory stages in women which featured with the high progesterone level (P4) as the non-active reproductive phases [284, 285].

The mice used in this study had normal estrous cyclicity (checked for a least 1 week before the infection, data not shown & Fig. 4.2B) before the infection. At the 0 dpi, the percentage of mice in diestrus stage (quiescent stage of estrous cycle) was comparable between the two treatment groups before the infection (Fig. 4.2A). However, at 7 dpi, all the mice with x31 infection stayed in the diestrus, which suggests suppressed estrous cyclicity after IAV infection (Fig. 4.2A&B).

Decreased body weight from fasting can result in disrupted estrous cyclicity [294]. To further study the disruption on estrous cycle and its correlation with the body weight decrease, we compared the daily body weight change after IAV infection with the estrous cyclicity from -7 dpi (7 days before infection) to 28 dpi in 6 female mice, in which 4 mice showed body weight gain from ~7 dpi and recovered estrous cyclicity at ~12 dpi (average body weight loss ~12%, part of data not shown, Fig. 4.2B), while 2 mice never recovered from decreased body weight or escaped from diestrus after IAV infection (part of data not shown, Fig. 4.2B). These data indicate that the arrested estrous cycle in diestrus is more likely correlated with decreased body weight after IAV infection.

4.4.3 Histopathology in lung after IAV infection

The respiratory tract is the main target for IAV infection, and we found pulmonary inflammation in x31-infected females at 7 dpi as an expected result from IAV infection, which further confirms the efficiency of our infection methods (Fig. 4.3A-B1) [171, 295]. The inflammation in infected lung was coincided with heavily infiltrated immune cells with CD45-positive staining,

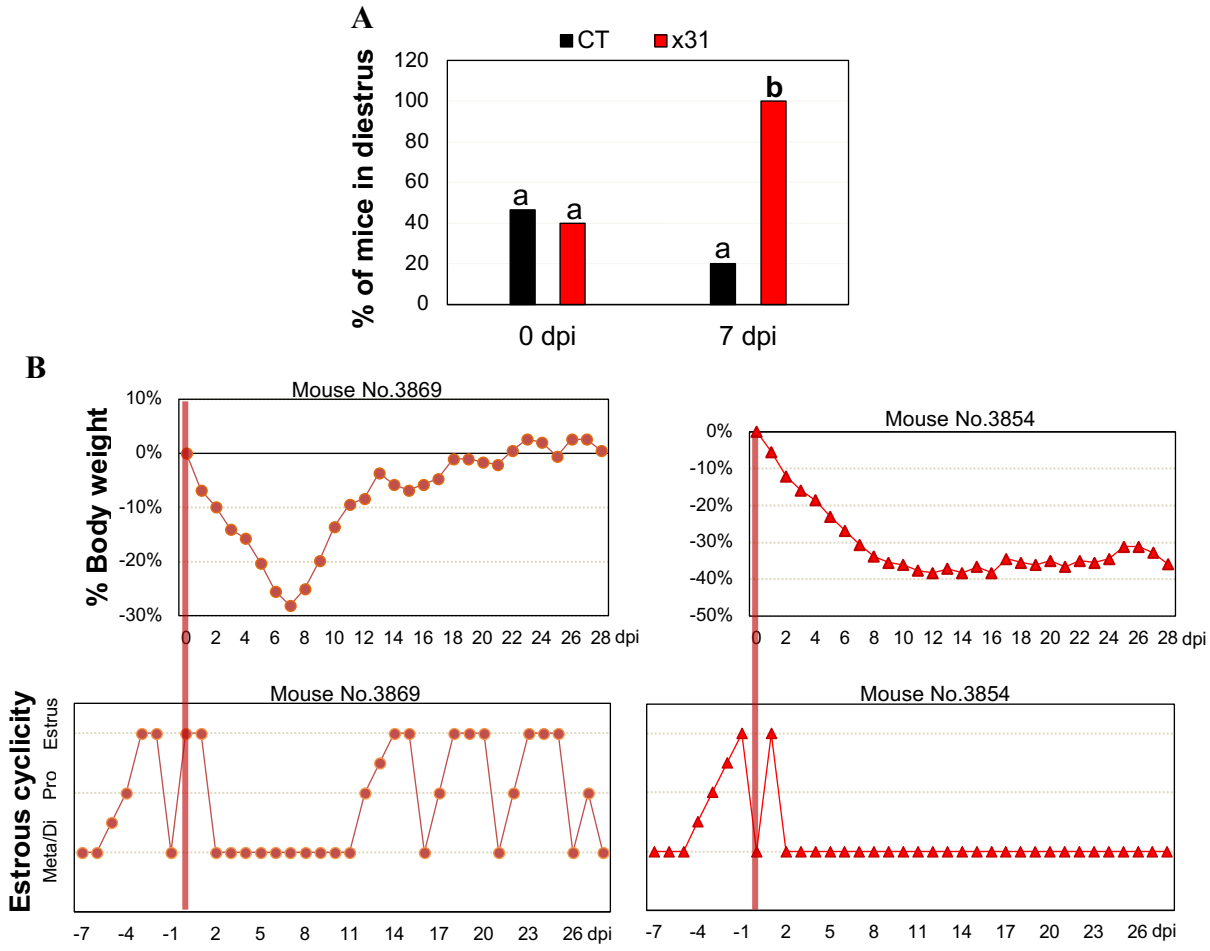

Figure 4.2. Female estrous cyclicity before (0 dpi) and after (7 dpi and 28 dpi) IAV infection. A. Percentage of mice in diestrus at 0 dpi and 7 dpi. a&b are $p<0.001$ from Chi-square test. N=15/group. CT: vehicle control treated female mice; x31: mouse-adapted H3N2 influenza-infected female mice. B. Correlation between body weight recovery and estrous cyclicity. Left two panels: one mouse as an example with recovered body weight and estrous cyclicity (N=4); Right two panels: one mouse as an example with non-recovered body weight and arrested estrous cycle (N=2). Estrous stages are defined as Meta/Di for metestrus and diestrus; Pro as proestrus; and estrus. Dark red lines: highlighted the infection day. dpi: days post infection.

while the uninfected lung had only few CD45 staining from immunohistochemistry (Fig. 4.3C-E, N=8-9/group, p<0.001).

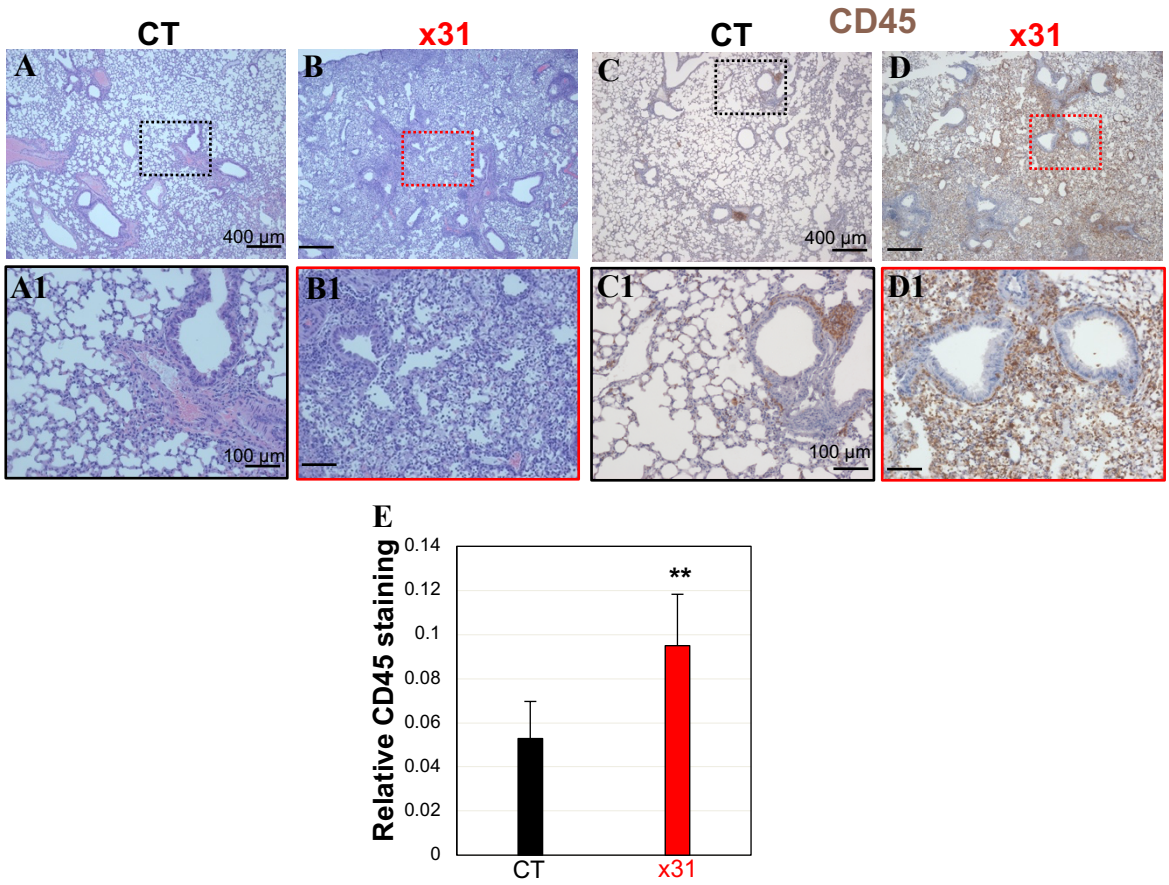

Figure 4.3. Histopathology in lung after x31-IAV infection. A-B1. Histology with H&E staining of uninfected (CT) and infected (x31) lung at 7 dpi. A1&B1: enlarged lung from boxed area in A&B respectively. C-D1: Immunohistochemistry of CD45 in uninfected (CT) and infected (x31) lung at 7 dpi. C1&D1: enlarged lung from boxed area in C&D respectively. E: Relative level of CD45 immunohistochemistry staining of 5x images. N=8-9/group. **p<0.001 from two-tail unequal variance t-test; error bar: standard deviation. Scale bar: 400μm for A-D; 100μm for A1-D1. CT: vehicle-treated control mice; x31: mouse-adapted H3N2 influenza-infected female mice. Brown staining: immunostaining of CD45; purple-blue staining: counter nuclei staining with hematoxylin. No specific immunostaining in negative controls (data not shown).

4.4.4 Comparable ovarian histology but increased follicles in preantral stages after IAV infection

To eliminate hormone as a contributing factor for regulating female reproductive system, we need to compare the uninfected and infected females from the same estrous stage with relatively comparable P4 and E2 levels. Since all the x31-infected females stayed in the diestrus stage, we collected another set of control mice in diestrus after vehicle control treatment (PBS, N=6, mice collected from 2-7 dpi).

We compared the ovarian histology, and the numbers of corpora lutea (CLs) and follicles from different development stages in x31-infected and uninfected diestrus ovaries (Fig. 4.4A-C).

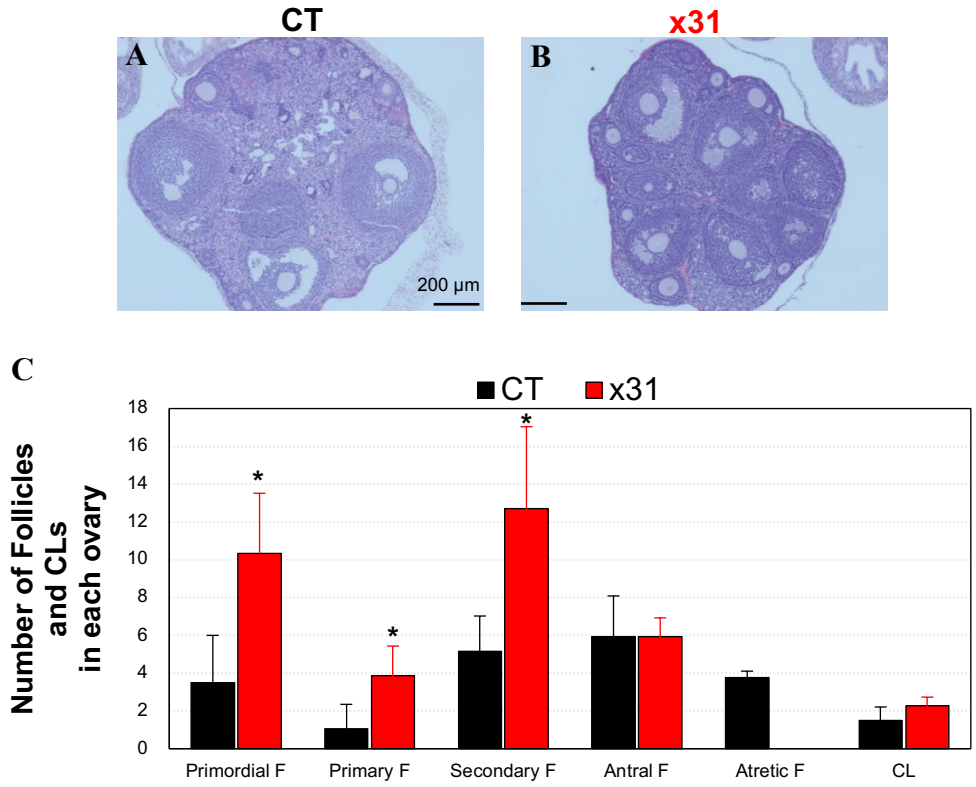

Figure 4.4. Comparable ovarian histology after IAV infection. A. A representative image of ovarian histology from control (CT) female in diestrus. Scale bar: 200µm. B. A representative image of ovarian histology from x31-infected female in diestrus from 7 dpi. C. Number of follicles and corpora lutea in control (CT) and infected (x31) diestrus ovaries. N=6-7/group. F: follicles; CL: corpus luteum. *$p<0.05$ compared to CT from two-tail unequal variance t-test; error bar: standard deviation.

The overall histology from diestrus ovaries of two treatment groups were comparable (Fig 4.4 A&B). To further analyze the ovarian activity, we counted the numbers of follicles and CLs, as they are the major developing units in the ovary, from ovarian histology and immunohistochemistry images (Fig. 4.4C, N=6-7/group). The x31-infected diestrus ovaries had more follicles in primordial, primary, and secondary developmental stages compared to the non-infected diestrus ovaries (Fig. 4.4C). However, due to the limited sections we collected per ovarian sample (N=2-10/sample), this increased number of follicles in infected group maybe biased by the small sample sizes. In order to get accurate numbers of follicles and CLs in each ovary, we need to collect serial sections of the entire ovary in future studies.

4.4.5 No significant adverse effects in ovaries from IAV infection

To further confirmed the ovarian status after IAV infection, we examined the cell proliferation (PCNA staining), cell death (cleaved caspase 3 staining), and immune cell population (CD45 staining) in the infected diestrus ovaries (Fig. 4.5A-G, N=4-6/group). The overall staining pattern for the three cell markers we examined looked comparable between the two treatments, and we also quantified the percentage of follicles with positive staining of each marker which also seemed to be comparable (Fig. 4.5G). Due to limited number of CLs we found, the staining in the CL was not quantified. The results suggested that cell proliferation, cell death, and the distribution of immune cells in the infected ovaries was not disrupted. Collectively, the immunohistochemistry data in the ovary indicated a normal ovarian activity after IAV infection.

4.4.6 Comparable uterine histology after IAV infection

We also examined the histology and immunohistochemistry staining of PCNA, cleaved caspase 3, and CD45 in infected and uninfected diestrus uterus, and both groups seemed to have comparable morphology and staining (Fig. 4.6 A-H1, N=6-9/group) which indicate no significant

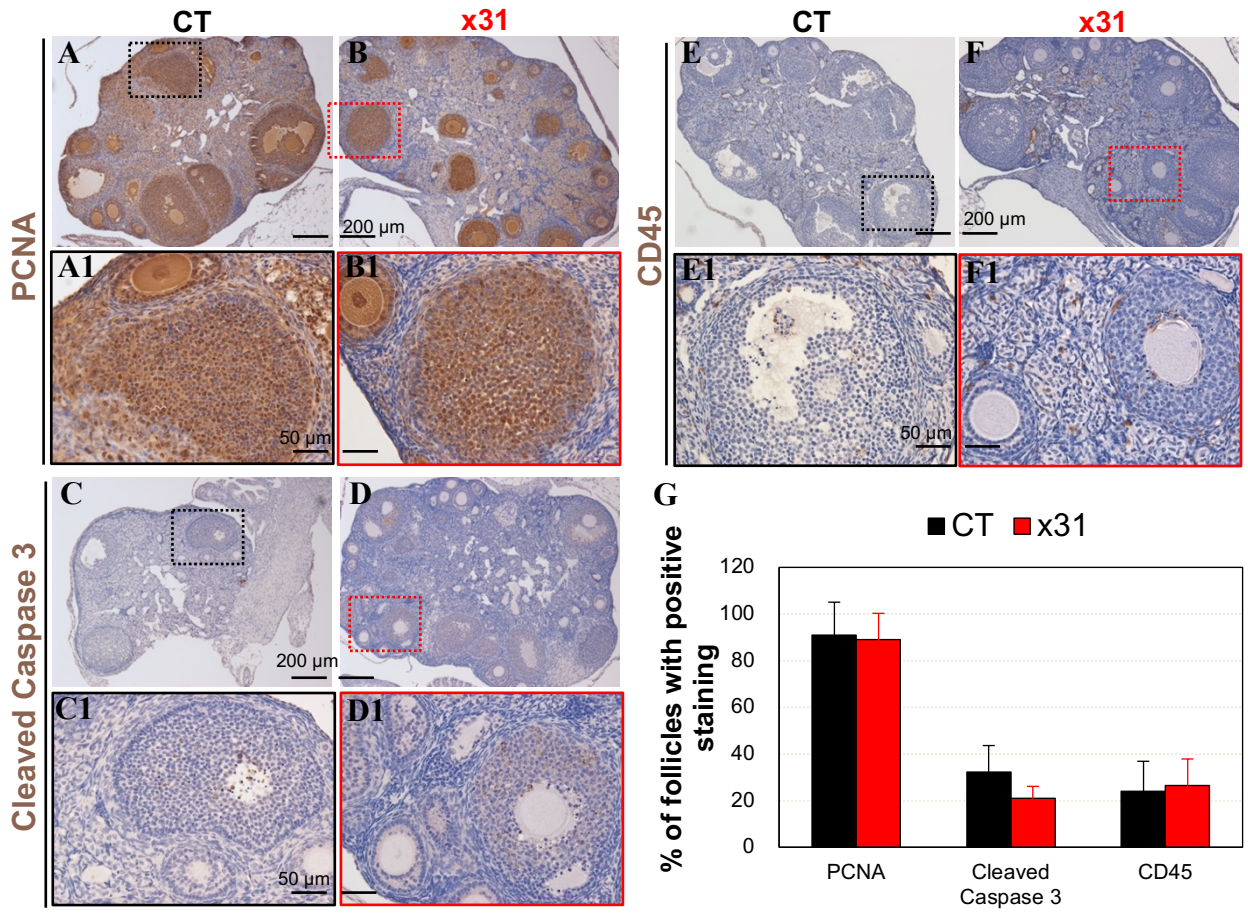

Figure 4.5. Immunohistochemistry staining of PCNA, Cleaved Caspase 3, and CD45 in diestrus ovary after IAV infection at 7 dpi. N=4-6/group. A-B1: PCNA staining as cell proliferation marker. C-D1: Cleaved Caspase 3 staining as cell death marker. E-F1: CD45 staining for immune cells distribution. G: Quantification of percentage of follicles with positive staining of the three cell markers. Error bar: standard deviation. A1-F1 are enlarged from boxed area in A-F respectively. Scale bar: 200µm for A- F; 50µm for A1-F1. CT: vehicle-treated control mice; x31: mouse-adapted H3N2 influenza-infected female mice at 7 dpi. Brown staining: positive staining of indicated cell markers; purple-blue staining: counter nuclei staining with hematoxylin. No specific immunostaining in negative controls (data not shown).

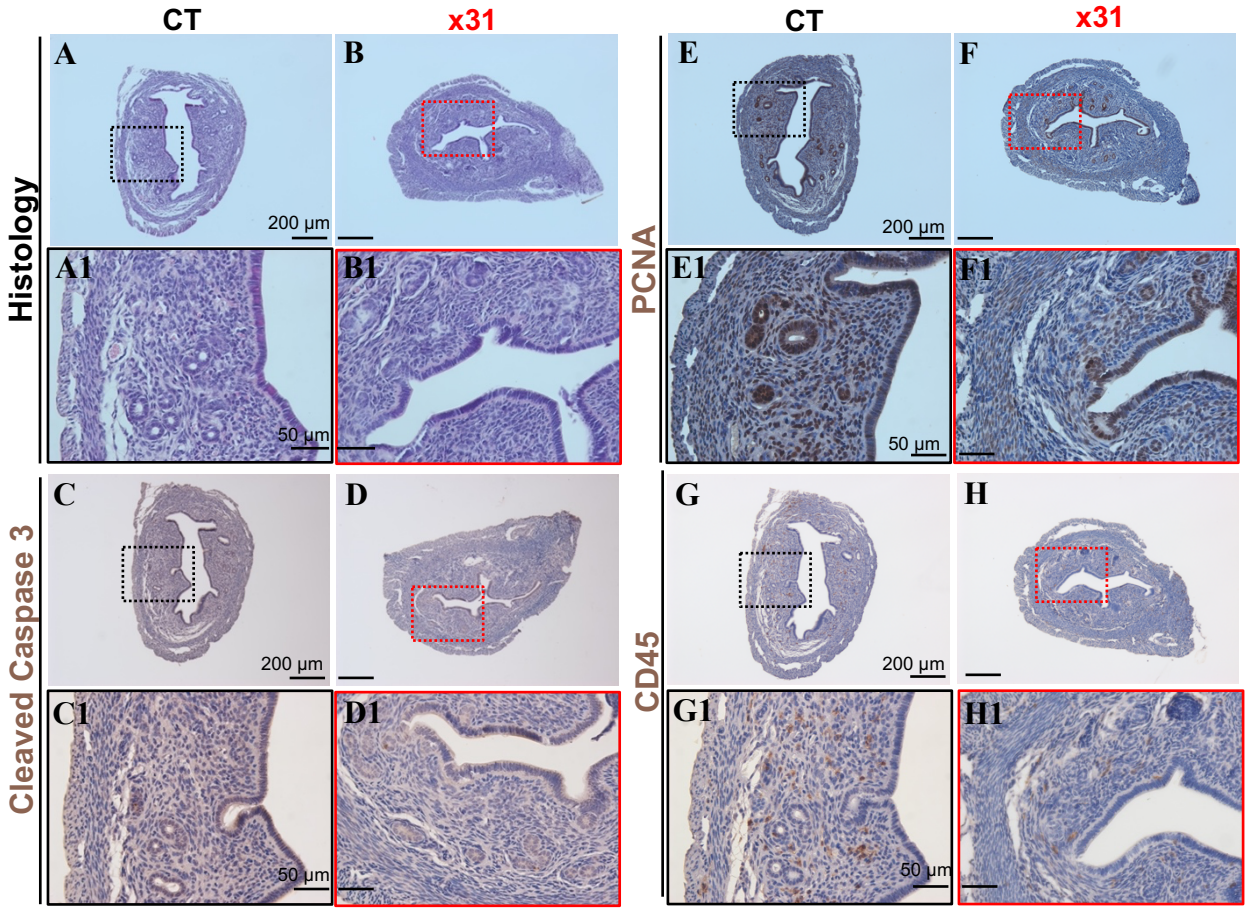

Figure 4.6. Histology and immunohistochemistry staining of PCNA, Cleaved Caspase 3, and CD45 in diestrus uterus after IAV infection at 7 dpi. N=6-9/group. A-B1: H&E staining of diestrus uterus from vehicle control and x31-infected mice at 7 dpi. C-D1: Cleaved Caspase 3 staining as cell death marker. E-F1: PCNA staining as cell proliferation marker. G-H1: CD45 staining for immune cells distribution. A1-H1 are enlarged from boxed area in A-H respectively. Scale bar: 200µm for A- H; 50µm for A1-H1. CT: vehicle-treated control mice; x31: mouse-adapted H3N2 influenza-infected female mice at 7 dpi. Brown staining in C-H1: positive staining of indicated cell markers; purple-blue staining: counter nuclei staining with hematoxylin. No specific immunostaining in negative controls (data not shown).

adverse effects in uterus after IAV infection. Together, the data from diestrus ovary and uterus suggested an overall normal reproductive morphology and cellular activities after IAV infection.

4.5 Discussion

This study investigated the effects of mouse-adapted H3N2 IAV (x31) infection on the female reproductive system of cycling female C57BL/6J mice. Nasal infection of 10^4 pfu of x31 significantly induced the body weight loss and lung injury with arrested estrous cycle in female mice, while the general histology and cellular activity in ovary and uterus remains comparable to the uninfected female in the same diestrus stage.

Body weight loss is a typical result from IAV infection and can be used as an indicator to reflect the severity of IAV infection. For x31 infection in mice, the body weight loss peaked at 7 dpi, and then started to recover (Fig. 4.2B) [291, 296-301]. The changes on mouse body weight confirmed our efficiency of nasal IAV infection, and suggested the trend of recovery started from 7 dpi followed with a full recovery at ~2 weeks after, which is similar to the trend of IAV progression in human [271]. The trend of weight loss is also associated with the severity of lung damage and immune responses [291, 295, 302, 303]. Indeed, at 7 dpi when the weight loss peaked, we observed lung injury with intensive immune cell infiltration (Fig. 4.3). Since lung is the primary target of IAV infection and the site for IAV replication, the lung injury is an expected result from IAV infection. As the first line of defense against IAV, the epithelial cells in the airway and alveola initiate innate responses by recruiting immune cells like macrophages, neutrophils, natural killer cells, and dendric cells, as well as secreting the inflammatory cytokines and interferons [132-134]. While in the later time points, the adaptive immune responses will be activated and help with the clearance of IAV [132, 135, 136], which responses to the body weight recovery we have seen after

7 dpi [291, 295, 300]. Together the pulmonary cell damage resulted from IAV infection and the immune responses caused the lung injury we seen and the pulmonary infiltration of CD45-positive immune cells.

The effects of IAV infection in female reproduction have been mostly focusing on the infection during pregnancy. Epidemiology data collected from seasonal and pandemic flu suggests that IAV infection can cause adverse maternal outcomes which put pregnancy women at higher risks to develop severe consequences like acute respiratory disease and death; it can also cause neonatal complications like miscarriage, preterm birth, stillbirths, and several birth defects [162-168]. Studies from rodents' models are mostly about the IAV infection during mid-late pregnancy and their associated complications. They recapitalized the findings in women which most IAV infections can cause higher mortality and morbidity in pregnancy mice than non-pregnant females, which related to the up-regulated inflammatory responses against IAV [169, 170, 173]. The mouse studies also found adverse effects of IAV infection in the placenta, fetus, and overall pregnancy outcomes which confirmed the data in pregnant women [171, 174, 175, 178].

What remain to be addressed is the effect of IAV infection in the non-pregnant status-- the female reproductive cycle. One study infected C57BL/6J female mice with mouse-adapted H1N1 IAV and also found increased duration of diestrus associated with a slight trend of decreasing E2 level after 3 dpi [286]. However, only the E2 level from 7 dpi showed a slight decrease compared to 0 dpi, and the E2 level fluctuates during the estrous cycles, therefore, the accuracy of their serum E2 measurement cannot be guaranteed [286]. Due to the same issue with our hormonal measurement accuracy, when we try to compare the serum E2 and P4 level from infected and uninfected females from diestrus stage using ELISA, we also cannot find consistent changes, which makes it hard to explain the arrested estrous cyclicity from IAV-infected females. One

explanation is the decreased the body weight, which seems to be correlated with the estrous cyclicity. Although we didn't monitor the changes of food and water intake in this IAV study, one recent study showed the correlation of body weight losses after IAV infection with decreased appetite regulated in brain [304]. And studies from food-restricted mice showed the decreased boy weight is associated with the cessation of estrous cycle and preserved follicles numbers, which can be restored after the lift of food restriction and regained body weight [294, 305]. Even though we did not find significant changes in histology or cellular activity of ovaries and uteri from IAV-infected females, there's a similar trend of increased number of follicles in the pre-antral stages from infected ovary. Although our follicular counts may not be accurate due to the limited sections per ovary we counted, the aberrant follicular development after IAV infection indicated a potential disruption of the fluctuate gonadotropins levels from the brain [306].

In summary, the mouse-adapted H3N2 infection have decreased body weights, lung injury, and disrupted mouse estrous cyclicity with a trend of arrested follicular development. The overall histology and cellular responses in ovary and uterus are not disrupted after IAV infection.

CHAPTER 5

CONCLUSION AND FUTURE DIRECTIONS

Human reproduction is not only designed for the continuance of human species, but also a form of life-long happiness. With the fertility rate in women have been declining in most countries over the past decades, infertility, which accounts for about 13% in women and 10% among man, is a growing concern in the modern world [307, 308]. Infertility in women is a complicated problem and can be caused by multiple factors like genetic, age, body weight, environmental exposures, endocrine, immunology, psychology, local disorders in the female reproductive system and so on [308-310]. The ultimate goal of our study is to explore these factors and their underlying mechanisms contributing to the increased infertility and impaired fecundity in women.

For women who made to successful conception, pregnancy loss is still a common problem that can affect up to 26% of pregnant women with 80% of them occurring during the first trimester (early pregnancy) [311-313]. Our focus of study is the embryo implantation, a critical step during early pregnancy, in which the delayed timing of implantation is highly associated with early pregnancy loss [314]. It is also the decisive step for patients undergoing *in vitro* fertilization and embryo transfer as only ~30% of the transferred embryos can successfully implant to the uterus [315]. The etiology of implantation failure is also complex and multifactorial, in which the proper P4 level and signaling is one of the crucial factors for the establishment of uterine receptivity for embryo implantation [31, 308, 310, 316-320]. Our topics in Chapter 2 and Chapter 3 are all related to the P4, with Chapter 2 focusing on lysosomal

functions in P4 production in the ovary during early pregnancy, and Chapter 3 studying regulatory effects of P4 in uterine preparation for embryo implantation.

The idea of the our study in Chapter 2 originated from our microarray analysis in uterine LE during embryo implantation time, which led us to study the function of *Atp6v0d2* (encoding V0D2 subunit of V-ATPase) in female reproduction and found its correlation to the acidification of LE and GE during implantation time [37, 42]. To further study the molecular mechanisms behind uterine acidification, which is most likely from the lysosomal acidification in the uterus, we further analyzed the expressions of lysosomal ion channels and found the *Mcoln1* has the highest mRNA expression during peri-implantation LE [37]. When we studied the functions of *Mcoln1* in female reproduction, we found the impaired fertility in *Mcoln1*$^{-/-}$ females was actually from the complications in the ovary, which led us to switch our study from uterine lysosomes to the lysosomes in the ovary with a special focus on the CL and P4 steroidogenesis [196]. The proper lysosomal function relies on its acidic luminal pH maintained by V-ATPase pumping H^+ into the lysosomal lumen and counter ion channels like TRPML1 (encodes by *Mcoln1*) to dissipate the transmembrane potential built up by V-ATPase via pumping cations out of lysosomal lumen [41, 85, 182, 183]. Chapter 2 is aiming to study the functions of these two ion channels on lysosomes and thus further the lysosomal functions in the ovary and P4 steroidogenesis. By using the *Atp6v0d2*$^{-/-}$*Mcoln1*$^{-/-}$ double knockout female mice and comparing their fertility and ovarian phenotypes in the *Mcoln1*$^{-/-}$ females, we summarized the interplay of these two genes on the female reproductive scale: 1) both genes are expressed in CLs during early pregnancy; 2) the knockout of both genes can partially rescue the female fertility and CL morphology and steroidogenesis deficiencies in *Mcoln1*$^{-/-}$ females. The conclusions drawn from Chapter 2 suggest that proteins ATP6V0D2 and TRPML1 have opposite roles in regulating

lysosomes, while the V0D2 subunit of V-ATPase alone is not powerful enough to counterplay the deficiency from the loss of function of TRPML1 in CLs and female fertility. The molecular mechanisms and lysosomal activity in the ovaries of these two mouse models remain to be investigated. With the global deletion of *Mcoln1* in mouse, to what extent the lysosomal pH and transmembrane potential are disrupted, what lysosomal enzymes and functions are affected in the cellular level, and to what extent they can be restored after the double deletion of *Atp6v0d2* and *Mcoln1*, need further examination. Beyond the effects we have seen in the ovary, the high expression levels of *Atp6v0d2* and *Mcoln1* in the uterine LE during implantation indicates their critical functions in the uterus and embryo implantation, in which they may have stronger interconnection and are possibly related to the process of uterine epithelial acidification and so much more. In order to study their functions in the uterus, further studies with exogenous P4 treatment are needed to compensate the P4 deficiencies in these two mouse models, thereby allowing us to fill in additional knowledge gaps related to lysosomal functions in embryo implantation. Besides the interesting findings in female reproductive system, our novel *Atp6v0d2*$^{-/-}$*Mcoln1*$^{-/-}$ mouse model, along with other mouse models with lysosomal deficiencies, are also valuable tools to study the functions of lysosomal ion channels in other critical organs and systems where these two genes are highly expressed like kidney, lung, and liver. Despite the fact that lysosomes are ubiquitously expressed organelles with household functions, there remain unknowns regarding their functions from molecular level to systemic level. Furthermore, lysosomal storage diseases (LSDs) in human, which cumulatively happen in 1 in 5000-8000 births, even though mostly related to single-gene mutation, has tremendous effects in multiple organs and systems of patients [321]. With the late onset of some LSDs, like Fabry disease, and the promise in improving lifespan and quality of LSDs patients advanced by modern therapies,

reproduction will be a pressing need for patients with good quality of life [321, 322]. Our research in Chapter 2 offers novel evidence of the functions and interactions of two lysosomal ion channels in the CL during early pregnancy, which provides vital insights into potential therapeutic strategies for the female fertility in LSDs patients in the future.

Chapter 3 focuses on the regulation of P4 in uterine fluid absorption during early pregnancy. Uterine fluid supports multiple early pregnancy events including semen liquefaction for fertilization, uterine lumen closure, and embryo-maternal communications for embryo implantation [29, 45, 56, 57, 212, 213]. Although the importance of uterine fluid absorption in implantation has not been confirmed in natural pregnancies, for patients undergoing *in vitro* fertilization and embryo transfer, the excess uterine fluid significantly reduces the successful rate of implantation for transferred embryos [43]. Studies from ovariectomized rats found that exogenous P4 can induce uterine fluid absorption through amiloride-sensitive channels (most likely ENaC) on uterine LE, while the detailed mechanisms during early pregnancy remain to be studied [46, 51, 207, 224]. By injecting a fluorescent dye (Alexa Hydrazide 488, AH) into mouse preimplantation uterus, we traced the uterine fluid absorption in the P4-deficient mouse model ($RhoA^{f/f}Pgr^{Cre/+}$) and control mice with the combination of exogenous P4 and PR-antagonist (RU486) treatments. We made two main conclusions regarding the P4 regulation in uterine fluid absorption during preimplantation: 1) P4 is critical for the bulk absorption of uterine fluid, which decreases from D0.5 to D3.5 preimplantation times; 2) autofluorescent dots on apical LE are most likely endocytosis of uterine fluid, which increases from D0.5 to D3.5 with minimal association with P4 regulation. Due to the lack of functional antibodies we've tested, we didn't have the chance to study the functions of apical LE ion channels (like ENaC) and water channels (aquaporins) in uterine fluid absorption, while the expression of ATP1A1 (major subunit of

Na^+/K^+ ATPase) on the basolateral LE suggests the release of Na^+ from LE to sub-LE spaces after it's been taken up by apical ion channels (like ENaC). However, we plan to try and test more antibodies targeting those LE channels, and with the help of them, we can further study the detailed mechanisms of P4 regulation in bulk absorption of uterine fluid during preimplantation. We've also collected preliminary data from Amiloride-treated mice with the intrauterine injection of AH, and the results we gathered so far indicated that intensive bulk absorption on D0.5 is Amiloride-sensitive, which suggests the involvements of Amiloride-sensitive channel, ENaC, in uterine fluid absorption. In order to have direct evidence of the mechanisms behind uterine fluid absorption, further studies using electrophysiology to trace the ion and water transport from uterine lumen to LE during early pregnancy are needed. We've also been planning to use cultured organoids of LE to study the hormonal regulation and mechanisms in uterine fluid movements *in vitro*, in which this simplified model should be easier to be monitored for molecular movements across the LE. Collectively, our published research in Chapter 3 was the first of its kind to visualize uterine fluid absorption *in vivo* and confirmed the P4 regulation in uterine fluid during early pregnancy. With the decreasing fertility in women over the past decades, the pressing demands for fertility support and assisted reproductive technology are increasing [307, 308]. Our research in Chapter 3 emphasizes the importance of P4 in early pregnancy, supports the demand of P4 supplementation in patients undergoing embryo transfer [323-325], and highlights the uterine fluid retention as a risk factor for implantation failure.

In order to have successful pregnancy, a regular menstrual cyclicity is required for women who wish to have natural conceptions [281-283]. In Chapter 4, we studied the exogenous disruption from IAV infection in female reproductive cyclicity, which is another contributing factor to female fertility. The present studies from human meta-analysis and mouse IAV

infection models are mostly focusing on the aspect of IAV infection in mid-late gestation, which is associated with increased risks of severe diseases and adverse pregnancy outcomes [162-175], while little is known about how IAV affects female cycles [286]. By infecting cycling mice with mouse-adapted H3N2 IAV (x31) and vehicle control, we targeted effects of IAV infection on female cyclicity and the reproductive system. Several conclusions are drawn from Chapter 4: 1) IAV infection causes body weight decrease and lung injury as expected; 2) arrested estrous cycle in quiescent diestrus stage after IAV infection may be a side effect from body weight loss; 3) ovarian and uterine histology and cellular activities are not disrupted by IAV infection, but there is a trend of increased ovarian follicles in early developmental stages. The reproductive phenotypes we collected from IAV infection are all expected results from severe body weight loss. Due to our study model used here, we cannot differentiate the direct reproductive effects of IAV infection from the side effects of body weight losses. Future studies comparing mice with IAV infection to those with only body weight losses are needed in order to study the direct effects from the infection only. However, a recent study from IAV infection revealed the cross-talk between respiratory system and the brain [304], which suggests another possibility of the communication network among respiratory system-central nervous system-reproductive system, since the female reproductive system is highly regulated by the brain through HPO axis [10]. To address this idea, further studies on these three systems after IAV infection, together with their potential communication carriers like chemokines, cytokines, hormones, and immune responses are needed. Although there is still a lot unknown regarding IAV infection in female fertility, this study expands our knowledge on IAV disruption in female cyclicity. Especially during our post-pandemic time, there's an increasing concern of the side-effects of viral infection outside the targeted organ, and our study in Chapter 4 provides novel findings of the effects from respiratory

viruses in the reproductive health of non-pregnant women, and emphasizes the need of choosing the conceiving time free from viral infections for successful natural conceptions.

In summary, the research in the present dissertation investigated how endogenous factors like ion channels on lysosomes and LE, and exogenous factors like IAV infection, can influence female fertility during early pregnancy and the female reproductive cycle. Our studies contribute to the reproductive field to have better understandings of lysosomal functions in the CL, P4 regulations in uterine fluid absorption during preimplantation, and IAV disruptions in cycling female mice. We continue to investigate the contributing factors involved in female fertility and provide advancements to improve clinical solutions for women suffering from reproductive problems.

References:

1. Jones RE, Lopez KH. Human reproductive biology. Amsterdam: Elsevier Academic Press; 2014.
2. Blanco LZ, Jr., Kuhn E, Morrison JC, Bahadirli-Talbott A, Smith-Sehdev A, Kurman RJ. Steroid hormone synthesis by the ovarian stroma surrounding epithelial ovarian tumors: a potential mechanism in ovarian tumorigenesis. Mod Pathol 2017; 30:563-576.
3. Matsumoto H. Molecular and cellular events during blastocyst implantation in the receptive uterus: clues from mouse models. J Reprod Dev 2017; 63:445-454.
4. Croy BA, Yamada AT, DeMayo FJ, Adamson SL, Elsevier. The guide to investigation of mouse pregnancy. Amsterdam: Elsevier/Academic Press; 2014.
5. OBSTETRICS. Implantation and Placental Development. In. Obgyn Key; 2017.
6. Li Y, Wang Z, Andersen CL, Ye X. Functions of Lysosomes in Mammalian Female Reproductive System. . Reproductive and Developmental Medicine 2020; 4(2):p109-122.
7. Ali S.H. Alchalabi, Hasliza Rahim, Erkihun Aklilu, Imad I. Al-Sultan, Abd Rahman Aziz, Mohd F. Malek, Suzanna H. Ronald, Khan MA. Histopathological changes associated with oxidative stress induced by electromagnetic waves in rats' ovarian and uterine tissues. Asian Pacific Journal of Reproduction 2016; 5:301-310.
8. Wang H, Dey SK. Roadmap to embryo implantation: clues from mouse models. Nat Rev Genet 2006; 7:185-199.
9. Medina RA, Garcia-Sastre A. Influenza A viruses: new research developments. Nat Rev Microbiol 2011; 9:590-603.
10. Sperling M, Majzoub JA, Menon RK, Stratakis CA, Elsevier. Sperling pediatric endocrinology. Philadelphia, PA: Elsevier; 2021.

11. Herbison AE. Control of puberty onset and fertility by gonadotropin-releasing hormone neurons. Nat Rev Endocrinol 2016; 12:452-466.

12. Eppig JJ, O'Brien MJ. Development in vitro of mouse oocytes from primordial follicles. Biol Reprod 1996; 54:197-207.

13. Zhou J, Peng X, Mei S. Autophagy in Ovarian Follicular Development and Atresia. Int J Biol Sci 2019; 15:726-737.

14. Jones ASK, Shikanov A. Follicle development as an orchestrated signaling network in a 3D organoid. Journal of Biological Engineering 2019; 13.

15. Li L, Shi X, Shi Y, Wang Z. The Signaling Pathways Involved in Ovarian Follicle Development. Front Physiol 2021; 12:730196.

16. Hattori K, Orisaka M, Fukuda S, Tajima K, Yamazaki Y, Mizutani T, Yoshida Y. Luteinizing Hormone Facilitates Antral Follicular Maturation and Survival via Thecal Paracrine Signaling in Cattle. Endocrinology 2018; 159:2337-2347.

17. Jameson JL, ScienceDirect. Endocrinology : adult & pediatric. Philadelphia, Pennsylvania: Saunders/Elsevier; 2016.

18. Caplan MJ. Reference Module in Biomedical Sciences. Amsterdam?: Elsevier; 2014.

19. Stocco C, Telleria C, Gibori G. The molecular control of corpus luteum formation, function, and regression. Endocr Rev 2007; 28:117-149.

20. Plant TM, Zeleznik AJ. Knobil and Neill's physiology of reproduction. Amsterdam: Elsevier/Academic Press; 2015.

21. El Zowalaty AE, Li R, Zheng Y, Lydon JP, DeMayo FJ, Ye X. Deletion of RhoA in Progesterone Receptor-Expressing Cells Leads to Luteal Insufficiency and Infertility in Female Mice. Endocrinology 2017; 158:2168-2178.

22. Robinson RS, Woad KJ, Hammond AJ, Laird M, Hunter MG, Mann GE. Angiogenesis and vascular function in the ovary. Reproduction 2009; 138:869-881.

23. Aboelenain M, Kawahara M, Balboula AZ, Montasser Ael M, Zaabel SM, Okuda K, Takahashi M. Status of autophagy, lysosome activity and apoptosis during corpus luteum regression in cattle. J Reprod Dev 2015; 61:229-236.

24. Choi J, Jo M, Lee E, Choi D. The role of autophagy in corpus luteum regression in the rat. Biol Reprod 2011; 85:465-472.

25. Yazawa T, Imamichi Y, Sekiguchi T, Miyamoto K, Uwada J, Khan MRI, Suzuki N, Umezawa A, Taniguchi T. Transcriptional Regulation of Ovarian Steroidogenic Genes: Recent Findings Obtained from Stem Cell-Derived Steroidogenic Cells. Biomed Res Int 2019; 2019:8973076.

26. Miller WL, Bose HS. Early steps in steroidogenesis: intracellular cholesterol trafficking. J Lipid Res 2011; 52:2111-2135.

27. Christenson LK, Devoto L. Cholesterol transport and steroidogenesis by the corpus luteum. Reprod Biol Endocrinol 2003; 1:90.

28. Manna PR, Dyson MT, Stocco DM. Regulation of the steroidogenic acute regulatory protein gene expression: present and future perspectives. Mol Hum Reprod 2009; 15:321-333.

29. Ye XQ. Uterine Luminal Epithelium as the Transient Gateway for Embryo Implantation. Trends in Endocrinology and Metabolism 2020; 31:165-180.

30. Yoshinaga K. A sequence of events in the uterus prior to implantation in the mouse. J Assist Reprod Genet 2013; 30:1017-1022.

31. Maurya VK, DeMayo FJ, Lydon JP. Illuminating the "Black Box" of Progesterone-Dependent Embryo Implantation Using Engineered Mice. Frontiers in Cell and Developmental Biology 2021; 9.

32. Ashary N, Tiwari A, Modi D. Embryo Implantation: War in Times of Love. Endocrinology 2018; 159:1188-1198.

33. Kim SM, Kim JS. A Review of Mechanisms of Implantation. Dev Reprod 2017; 21:351-359.

34. Ochoa-Bernal MA, Fazleabas AT. Physiologic Events of Embryo Implantation and Decidualization in Human and Non-Human Primates. Int J Mol Sci 2020; 21.

35. Okada H, Tsuzuki T, Murata H. Decidualization of the human endometrium. Reprod Med Biol 2018; 17:220-227.

36. Chen Y, Ni H, Ma XH, Hu SJ, Luan LM, Ren G, Zhao YC, Li SJ, Diao HL, Xu X, Zhao ZA, Yang ZM. Global analysis of differential luminal epithelial gene expression at mouse implantation sites. Journal of Molecular Endocrinology 2006; 37:147-161.

37. Xiao S, Diao H, Zhao F, Li R, He N, Ye X. Differential gene expression profiling of mouse uterine luminal epithelium during periimplantation. Reprod Sci 2014; 21:351-362.

38. Aikawa S, Hirota Y, Fukui Y, Ishizawa C, R II, Kaku T, Hirata T, Akaeda S, Hiraoka T, Matsuo M, Osuga Y. A gene network of uterine luminal epithelium organizes mouse blastocyst implantation. Reprod Med Biol 2022; 21:e12435.

39. Wu SP, Emery OM, DeMayo FJ. Molecular Studies on Pregnancy with Mouse Models. Curr Opin Physiol 2020; 13:123-127.

40. Toei M, Saum R, Forgac M. Regulation and isoform function of the V-ATPases. Biochemistry 2010; 49:4715-4723.

41. Mindell JA. Lysosomal acidification mechanisms. Annu Rev Physiol 2012; 74:69-86.

42. Xiao S, Li R, El Zowalaty AE, Diao H, Zhao F, Choi Y, Ye X. Acidification of uterine epithelium during embryo implantation in mice. Biol Reprod 2017; 96:232-243.

43. Chien LW, Au HK, Xiao J, Tzeng CR. Fluid accumulation within the uterine cavity reduces pregnancy rates in women undergoing IVF. Human Reproduction 2002; 17:351-356.

44. He RH, Gao HJ, Li YQ, Zhu XM. The associated factors to endometrial cavity fluid and the relevant impact on the IVF-ET outcome. Reprod Biol Endocrinol 2010; 8:46.

45. Zhang Y, Wang Q, Wang H, Duan E. Uterine Fluid in Pregnancy: A Biological and Clinical Outlook. Trends Mol Med 2017; 23:604-614.

46. Clemetson CA, Verma UL, De Carlo SJ. Secretion and reabsorption of uterine luminal fluid in rats. J Reprod Fertil 1977; 49:183-187.

47. Parr MB. Effects of Ovarian Hormones on Endocytosis at the Basal Membranes of Rat Uterine Epithelial-Cells. Biology of Reproduction 1982; 26:909-913.

48. Parr MB, Parr EL. Endocytosis in the Rat Uterine Epithelium at Implantation. Annals of the New York Academy of Sciences 1986; 476:110-121.

49. Matthews CJ, Thomas EJ, Redfern CP, Hirst BH. Ion transport by human endometrial epithelia in vitro. Hum Reprod 1993; 8:1570-1575.

50. Naftalin RJ, Thiagarajah JR, Pedley KC, Pocock VJ, Milligan SR. Progesterone stimulation of fluid absorption by the rat uterine gland. Reproduction 2002; 123:633-638.

51. Salleh N, Baines DL, Naftalin RJ, Milligan SR. The hormonal control of uterine luminal fluid secretion and absorption. J Membr Biol 2005; 206:17-28.

52. Liu XM, Zhang D, Wang TT, Sheng JZ, Huang HF. Ion/water channels for embryo implantation barrier. Physiology (Bethesda) 2014; 29:186-195.

53. Ruan YC, Chen H, Chan HC. Ion channels in the endometrium: regulation of endometrial receptivity and embryo implantation. Hum Reprod Update 2014; 20:517-529.

54. Floyd RV, Mobasheri A, Wray S. Gestation changes sodium pump isoform expression, leading to changes in ouabain sensitivity, contractility, and intracellular calcium in rat uterus. Physiol Rep 2017; 5.

55. Richard C, Gao J, Brown N, Reese J. Aquaporin water channel genes are differentially expressed and regulated by ovarian steroids during the periimplantation period in the mouse. Endocrinology 2003; 144:1533-1541.

56. Zhang Y, Chen Q, Zhang H, Wang Q, Li R, Jin YP, Wang HB, Ma TH, Qiao J, Duan EK. Aquaporin-dependent excessive intrauterine fluid accumulation is a major contributor in hyper-estrogen induced aberrant embryo implantation. Cell Research 2015; 25:139-142.

57. Ribeiro JC, Alves MG, Yeste M, Cho YS, Calamita G, Oliveira PF. Aquaporins and (in)fertility: More than just water transport. Biochimica Et Biophysica Acta-Molecular Basis of Disease 2021; 1867.

58. Zhang Z, Yue P, Lu T, Wang Y, Wei Y, Wei X. Role of lysosomes in physiological activities, diseases, and therapy. J Hematol Oncol 2021; 14:79.

59. Maxfield FR, Willard JM, Lu S, ProQuest. Lysosomes : biology, diseases, and therapeutics. Hoboken, New Jersey: Wiley; 2016.

60. Li P, Gu M, Xu H. Lysosomal Ion Channels as Decoders of Cellular Signals. Trends Biochem Sci 2019; 44:110-124.

61. Li P, Gu MX, Xu HX. Lysosomal Ion Channels as Decoders of Cellular Signals. Trends in Biochemical Sciences 2019; 44:110-124.

62. Trivedi PC, Bartlett JJ, Pulinilkunnil T. Lysosomal Biology and Function: Modern View of Cellular Debris Bin. Cells 2020; 9.

63. Kaksonen M, Roux A. Mechanisms of clathrin-mediated endocytosis. Nat Rev Mol Cell Biol 2018; 19:313-326.

64. Doherty GJ, McMahon HT. Mechanisms of endocytosis. Annu Rev Biochem 2009; 78:857-902.

65. Mayor S, Parton, R. G., & Donaldson, J. G. Clathrin-independent pathways of endocytosis. Cold Spring Harbor perspectives in biology 2014; 6:a016758.

66. Stillwell W. Membrane Transport. In: An Introduction to Biological Membranes, Second Edition ed: Elsevier; 2016: 423-451.

67. Lancaster CE, Ho CY, Hipolito VEB, Botelho RJ, Terebiznik MR. Phagocytosis: what's on the menu? (1). Biochem Cell Biol 2019; 97:21-29.

68. Maxfield FR, Willard, J. M., & Lu, S. . Lysosomes: biology, diseases, and therapeutics. . Hoboken, New Jersey: John Wiley & Sons; 2016.

69. Denton D, Kumar S. Autophagy-dependent cell death. Cell Death Differ 2019; 26:605-616.

70. van Beek N, Klionsky DJ, Reggiori F. Genetic aberrations in macroautophagy genes leading to diseases. Biochim Biophys Acta Mol Cell Res 2018; 1865:803-816.

71. Li W, Nie T, Xu H, Yang J, Yang Q, Mao Z. Chaperone-mediated autophagy: Advances from bench to bedside. Neurobiol Dis 2019; 122:41-48.

72. Oku M, Sakai Y. Three Distinct Types of Microautophagy Based on Membrane Dynamics and Molecular Machineries. Bioessays 2018; 40:e1800008.

73. Cao B, Camden AJ, Parnell LA, Mysorekar IU. Autophagy regulation of physiological and pathological processes in the female reproductive tract. Am J Reprod Immunol 2017; 77.

74. Wang F, Gomez-Sintes R, Boya P. Lysosomal membrane permeabilization and cell death. Traffic 2018; 19:918-931.

75. Overholtzer M, Mailleux AA, Mouneimne G, Normand G, Schnitt SJ, King RW, Cibas ES, Brugge JS. A nonapoptotic cell death process, entosis, that occurs by cell-in-cell invasion. Cell 2007; 131:966-979.

76. Dhanasekaran N, Sheela Rani CS, Moudgal NR. Studies on follicular atresia: lysosomal enzyme activity and gonadotropin receptors of granulosa cells following administration or withdrawal of gonadotropins in the rat. Mol Cell Endocrinol 1983; 33:97-112.

77. Rosales-Torres AM, Avalos-Rodriguez A, Vergara-Onofre M, Hernandez-Perez O, Ballesteros LM, Garcia-Macedo R, Ortiz-Navarrete V, Rosado A. Multiparametric study of atresia in ewe antral follicles: histology, flow cytometry, internucleosomal DNA fragmentation, and lysosomal enzyme activities in granulosa cells and follicular fluid. Mol Reprod Dev 2000; 55:270-281.

78. Alonso-Pozos I, Rosales-Torres AM, Avalos-Rodriguez A, Vergara-Onofre M, Rosado-Garcia A. Mechanism of granulosa cell death during follicular atresia depends on follicular size. Theriogenology 2003; 60:1071-1081.

79. Miyake Y, Matsumoto, H., et al. Expression and glycosylation with polylactosamine of CD44 antigen on macrophages during follicular atresia in pig ovaries. Biology of reproduction 2006; 74:501-510.

80. Eykelbosh AJ, Van Der Kraak G. A role for the lysosomal protease cathepsin B in zebrafish follicular apoptosis. Comp Biochem Physiol A Mol Integr Physiol 2010; 156:218-223.

81. Escobar ML, Echeverria OM, Ortiz R, Vazquez-Nin GH. Combined apoptosis and autophagy, the process that eliminates the oocytes of atretic follicles in immature rats. Apoptosis 2008; 13:1253-1266.

82. Rodrigues P, Limback D, McGinnis LK, Plancha CE, Albertini DF. Multiple mechanisms of germ cell loss in the perinatal mouse ovary. Reproduction 2009; 137:709-720.

83. Parr EL. Beta-galactosidase in rat ovarian bursa fluid at ovulation. Biol Reprod 1974; 11:504-508.

84. Cajander S, Bjersing L. Further-Studies of Surface Epithelium Covering Preovulatory Rabbit Follicles with Special Reference to Lysosomal Alterations. Cell and Tissue Research 1976; 169:129-141.

85. Xu H, Ren D. Lysosomal physiology. Annu Rev Physiol 2015; 77:57-80.

86. Aboelenain M, Kawahara M, Balboula AZ, Montasser A, Zaabel SM, Okuda K, Takahashi M. Status of autophagy, lysosome activity and apoptosis during corpus luteum regression in cattle. Journal of Reproduction and Development 2015; 61:229-236.

87. Choi J, Jo M, Lee E, Choi D. The Role of Autophagy in Corpus Luteum Regression in the Rat (vol 85, pg 465, 2011). Biology of Reproduction 2012; 86.

88. Gregoraszczuk EL, Sadowska J. Lysosomal acid phosphatase activity and progesterone secretion by porcine corpora lutea at various periods of the luteal phase. Folia Histochemica Et Cytobiologica 1997; 35:35-39.

89. Savion N, Laherty R, Lui GM, Gospodarowicz D. Modulation of low density lipoprotein metabolism in bovine granulosa cells as a function of their steroidogenic activity. J Biol Chem 1981; 256:12817-12822.

90. Krishnamurthy H, Kishi H, Shi M, Galet C, Bhaskaran RS, Hirakawa T, Ascoli M. Postendocytotic trafficking of the follicle-stimulating hormone (FSH)-FSH receptor complex. Mol Endocrinol 2003; 17:2162-2176.

91. Mitra S, Rao CV. Receptors for gonadotropins and prostaglandins in lysosomes of bovine corpora lutea. Arch Biochem Biophys 1978; 185:126-133.

92. Niswender GD. Response of the corpus luteum to luteinizing hormone. Environ Health Perspect 1981; 38:47-50.

93. Parr EL, Parr MB. Uptake of immunoglobulins and other proteins from serum into epithelial cells of the mouse uterus and oviduct. J Reprod Immunol 1986; 9:339-354.

94. Parr EL, Tung HN, Parr MB. Endocytosis in the epithelium of the mouse oviduct. Am J Anat 1988; 181:393-400.

95. Pillai VV, Weber DM, Phinney BS, Selvaraj V. Profiling of proteins secreted in the bovine oviduct reveals diverse functions of this luminal microenvironment. PLoS One 2017; 12:e0188105.

96. Abe H, Onodera M, Sugawara S, Satoh T, Hoshi H. Ultrastructural features of goat oviductal secretory cells at follicular and luteal phases of the oestrous cycle. J Anat 1999; 195 (Pt 4):515-521.

97. Murray MK. Morphological features of epithelial cells in the sheep isthmus oviduct during early pregnancy. Anat Rec 1997; 247:368-378.

98. Choi J, Jo M, Lee E, Oh YK, Choi D. The role of autophagy in human endometrium. Biol Reprod 2012; 86:70.

99. Salamonsen LA, Kovacs GT, Findlay JK. Current concepts of the mechanisms of menstruation. Baillieres Best Pract Res Clin Obstet Gynaecol 1999; 13:161-179.

100. Wood JC. Lysosomes of the uterus. Adv Reprod Physiol 1973; 6:221-230.

101. Tung HN, Parr EL, Parr MB. Endocytosis in the uterine luminal and glandular epithelial cells of mice during early pregnancy. Am J Anat 1988; 182:120-129.

102. Elangovan S, Moulton BC. Blastocyst implantation in the rat and the immunohistochemical distribution and rate of synthesis of uterine lysosomal cathepsin D. Biol Reprod 1980; 23:663-668.

103. Kirk AT, Murphy CR. Increase in lysosomal numbers and activity in the rat uterine luminal and glandular epithelium during early pregnancy: a histochemical study. Acta Anat (Basel) 1991; 141:63-69.

104. Moulton BC. Ovum implantation and uterine lysosomal enzyme activity. Biol Reprod 1974; 10:543-548.

105. Moulton BC. Progesterone and estrogen control of the response of rat uterine lysosomal cathepsin D activity to a deciduogenic stimulus. Endocrinology 1982; 110:1197-1202.

106. Parr EL, Tung HN, Parr MB. Apoptosis as the mode of uterine epithelial cell death during embryo implantation in mice and rats. Biol Reprod 1987; 36:211-225.

107. Poelmann RE. An ultrastructural study of implanting mouse blastocysts: coated vesicles and epithelium formation. J Anat 1975; 119:421-434.

108. Burns GW, Brooks KE, Spencer TE. Extracellular Vesicles Originate from the Conceptus and Uterus During Early Pregnancy in Sheep. Biol Reprod 2016; 94:56.

109. Tancini B, Buratta S, Sagini K, Costanzi E, Delo F, Urbanelli L, Emiliani C. Insight into the Role of Extracellular Vesicles in Lysosomal Storage Disorders. Genes 2019; 10.

110. Abraham R, Mankes R, Fulfs J, Goldberg L, Coulston F. Effects of intrauterine copper wire on blastocyst and uterine lysosomes of the rabbit: a cytochemical and ultrastructural study. J Reprod Fertil 1974; 36:59-67.

111. Cornillie FJ, Vasquez G, Brosens I. The response of human endometriotic implants to the anti-progesterone steroid R 2323: a histologic and ultrastructural study. Pathol Res Pract 1985; 180:647-655.

112. Mehrotra PK, Nilsson BO. Ultrastructural effects of the nonsteroidal contraceptive centchroman on rat uterine luminal epithelium in early pregnancy. Int J Fertil 1984; 29:44-53.

113. Song G, Bailey DW, Dunlap KA, Burghardt RC, Spencer TE, Bazer FW, Johnson GA. Cathepsin B, cathepsin L, and cystatin C in the porcine uterus and placenta: potential roles in endometrial/placental remodeling and in fluid-phase transport of proteins secreted by uterine epithelia across placental areolae. Biol Reprod 2010; 82:854-864.

114. Song G, Bazer FW, Spencer TE. Differential expression of cathepsins and cystatin C in ovine uteroplacental tissues. Placenta 2007; 28:1091-1098.

115. Varanou A, Withington SL, Lakasing L, Williamson C, Burton GJ, Hemberger M. The importance of cysteine cathepsin proteases for placental development. J Mol Med (Berl) 2006; 84:305-317.

116. Nakashima A, Tsuda S, Kusabiraki T, Aoki A, Ushijima A, Shima T, Cheng SB, Sharma S, Saito S. Current Understanding of Autophagy in Pregnancy. Int J Mol Sci 2019; 20.

117. Dantzer V. An extensive lysosomal system in the maternal epithelium of the porcine placenta. Placenta 1984; 5:117-129.

118. Straatsburg IH, Gossrau R. Enzyme histochemistry of the regressing rat decidua and metrial gland. Acta Histochem 1993; 94:202-219.

119. Agrawal V, Jaiswal MK, Mallers T, Katara GK, Gilman-Sachs A, Beaman KD, Hirsch E. Altered autophagic flux enhances inflammatory responses during inflammation-induced preterm labor. Sci Rep 2015; 5:9410.

120. Sato T, Fukazawa Y, Kojima H, Enari M, Iguchi T, Ohta Y. Apoptotic cell death during the estrous cycle in the rat uterus and vagina. Anatomical Record 1997; 248:76-83.

121. Geist SH, Lullmann-Rauch R. Experimentally induced lipidosis in uterine and vaginal epithelium of rats. Ann Anat 1994; 176:3-9.

122. Shroff A, Sequeira R, Patel V, Reddy KVR. Knockout of autophagy gene, ATG5 in mice vaginal cells abrogates cytokine response and pathogen clearance during vaginal infection of Candida albicans. Cellular Immunology 2018; 324:59-73.

123. Kinlock BL, Wang YD, Turner TM, Wang CL, Liu BD. Transcytosis of HIV-1 through Vaginal Epithelial Cells Is Dependent on Trafficking to the Endocytic Recycling Pathway. Plos One 2014; 9.

124. WHO. Influenza. In: World Health Organization; 2023.

125. Hutchinson EC. Influenza Virus. Trends Microbiol 2018; 26:809-810.

126. Li X, Gu M, Zheng Q, Gao R, Liu X. Packaging signal of influenza A virus. Virol J 2021; 18:36.

127. Taubenberger JK, Kash JC. Influenza virus evolution, host adaptation, and pandemic formation. Cell Host Microbe 2010; 7:440-451.

128. Su WC, Yu WY, Huang SH, Lai MMC. Ubiquitination of the Cytoplasmic Domain of Influenza A Virus M2 Protein Is Crucial for Production of Infectious Virus Particles. Journal of Virology 2018; 92.

129. Swayne DE, Wiley Online L. Animal influenza. Ames, Iowa Chichester, West Sussex: John Wiley & Sons, Inc. Wiley Online Library; 2017.

130. Bouvier NM, Palese P. The biology of influenza viruses. Vaccine 2008; 26:D49-D53.

131. Vahey MD, Fletcher DA. Low-Fidelity Assembly of Influenza A Virus Promotes Escape from Host Cells. Cell 2020; 180:205.

132. Bahadoran A, Lee SH, Wang SM, Manikam R, Rajarajeswaran J, Raju CS, Sekaran SD. Immune Responses to Influenza Virus and Its Correlation to Age and Inherited Factors. Front Microbiol 2016; 7:1841.

133. Chen X, Liu S, Goraya MU, Maarouf M, Huang S, Chen JL. Host Immune Response to Influenza A Virus Infection. Front Immunol 2018; 9:320.

134. Ramos I, Smith G, Ruf-Zamojski F, Martinez-Romero C, Fribourg M, Carbajal EA, Hartmann BM, Nair VD, Marjanovic N, Monteagudo PL, DeJesus VA, Mutetwa T, et al. Innate Immune Response to Influenza Virus at Single-Cell Resolution in Human Epithelial Cells Revealed Paracrine Induction of Interferon Lambda 1. Journal of Virology 2019; 93.

135. Jung HE, Lee HK. Host Protective Immune Responses against Influenza A Virus Infection. Viruses 2020; 12.

136. Varghese PM, Kishore U, Rajkumari R. Innate and adaptive immune responses against Influenza A Virus: Immune evasion and vaccination strategies. Immunobiology 2022; 227.

137. Rajendran M, Krammer F, McMahon M. The Human Antibody Response to the Influenza Virus Neuraminidase Following Infection or Vaccination. Vaccines (Basel) 2021; 9.

138. Doherty DG, Melo AM, Moreno-Olivera A, Solomos AC. Activation and Regulation of B Cell Responses by Invariant Natural Killer T Cells. Front Immunol 2018; 9:1360.

139. de Jong MD, Simmons CP, Thanh TT, Hien VM, Smith GJD, Chau TNB, Hoang DM, Chau NVV, Khanh TH, Dong VC, Qui PT, Van Cam B, et al. Fatal outcome of human influenza A (H5N1) is associated with high viral load and hypercytokinemia. Nature Medicine 2006; 12:1203-1207.

140. Lipatov AS, Andreansky S, Webby RJ, Hulse DJ, Rehg JE, Krauss S, Perez DR, Doherty PC, Webster RG, Sangster MY. Pathogenesis of Hong Kong H5N1 influenza virus NS gene reassortants in mice: the role of cytokines and B- and T-cell responses. J Gen Virol 2005; 86:1121-1130.

141. Yunis J, Short KR, Yu D. Severe respiratory viral infections: T-cell functions diverging from immunity to inflammation. Trends Microbiol 2023.

142. Damjanovic D, Small CL, Jeyanathan M, McCormick S, Xing Z. Immunopathology in influenza virus infection: uncoupling the friend from foe. Clin Immunol 2012; 144:57-69.

143. Tavares LP, Teixeira MM, Garcia CC. The inflammatory response triggered by Influenza virus: a two edged sword. Inflamm Res 2017; 66:283-302.

144. Gorski SA, Hufford MM, Braciale TJ. Recent insights into pulmonary repair following virus-induced inflammation of the respiratory tract. Current Opinion in Virology 2012; 2:233-241.

145. Ong JWJ, Tan KS, Ler SG, Gunaratne J, Choi H, Seet JE, Chow VTK. Insights into Early Recovery from Influenza Pneumonia by Spatial and Temporal Quantification of Putative Lung Regenerating Cells and by Lung Proteomics. Cells 2019; 8.

146. Pociask DA, Scheller EV, Mandalapu S, McHugh KJ, Enelow RI, Fattman CL, Kolls JK, Alcorn JF. IL-22 Is Essential for Lung Epithelial Repair following Influenza Infection. American Journal of Pathology 2013; 182:1286-1296.

147. Hoffmann J, Otte A, Thiele S, Lotter H, Shu YL, Gabriel G. Sex differences in H7N9 influenza A virus pathogenesis. Vaccine 2015; 33:6949-6954.

148. Klein SL, Hodgson A, Robinson DP. Mechanisms of sex disparities in influenza pathogenesis. J Leukoc Biol 2012; 92:67-73.

149. Peretz J, Hall OJ, Klein SL. Sex Differences in Influenza Virus Infection, Vaccination, and Therapies. In: Klein SL, Roberts CW (eds.), Sex and Gender Differences in Infection and Treatments for Infectious Diseases. Cham: Springer International Publishing; 2015: 183-210.

150. Straub RH. The complex role of estrogens in inflammation. Endocr Rev 2007; 28:521-574.

151. Robinson DP, Hall OJ, Nilles TL, Bream JH, Klein SL. 17beta-estradiol protects females against influenza by recruiting neutrophils and increasing virus-specific CD8 T cell responses in the lungs. J Virol 2014; 88:4711-4720.

152. Peretz J, Pekosz A, Lane AP, Klein SL. Estrogenic compounds reduce influenza A virus replication in primary human nasal epithelial cells derived from female, but not male, donors. Am J Physiol Lung Cell Mol Physiol 2016; 310:L415-425.

153. Davis SM, Sweet LM, Oppenheimer KH, Suratt BT, Phillippe M. Estradiol and progesterone influence on influenza infection and immune response in a mouse model. Am J Reprod Immunol 2017; 78.

154. Vom Steeg LG, Klein SL. Sex and sex steroids impact influenza pathogenesis across the life course. Semin Immunopathol 2019; 41:189-194.

155. Vermillion MS, Ursin RL, Attreed SE, Klein SL. Estriol Reduces Pulmonary Immune Cell Recruitment and Inflammation to Protect Female Mice From Severe Influenza. Endocrinology 2018; 159:3306-3320.

156. Hall OJ, Limjunyawong N, Vermillion MS, Robinson DP, Wohlgemuth N, Pekosz A, Mitzner W, Klein SL. Progesterone-Based Therapy Protects Against Influenza by Promoting Lung Repair and Recovery in Females. Plos Pathogens 2016; 12.

157. Hall OJ, Nachbagauer R, Vermillion MS, Fink AL, Phuong V, Krammer F, Klein SL. Progesterone-Based Contraceptives Reduce Adaptive Immune Responses and Protection against Sequential Influenza A Virus Infections. Journal of Virology 2017; 91.

158. Robinson DP, Huber SA, Moussawi M, Roberts B, Teuscher C, Watkins R, Arnold AP, Klein SL. Sex chromosome complement contributes to sex differences in coxsackievirus B3 but not influenza A virus pathogenesis. Biol Sex Differ 2011; 2:8.

159. Krementsov DN, Case LK, Dienz O, Raza A, Fang Q, Ather JL, Poynter ME, Boyson JE, Bunn JY, Teuscher C. Genetic variation in chromosome Y regulates susceptibility to influenza A virus infection. Proc Natl Acad Sci U S A 2017; 114:3491-3496.

160. Bongen E, Lucian H, Khatri A, Fragiadakis GK, Bjornson ZB, Nolan GP, Utz PJ, Khatri P. Sex Differences in the Blood Transcriptome Identify Robust Changes in Immune Cell Proportions with Aging and Influenza Infection. Cell Rep 2019; 29:1961-1973 e1964.

161. Sabikunnahar B, Lahue KG, Asarian L, Fang Q, McGill MM, Haynes L, Teuscher C, Krementsov DN. Sex differences in susceptibility to influenza A virus infection depend on host genotype. PLOS ONE 2022; 17:e0273050.

162. Abdullahi H, Elnahas A, Konje JC. Seasonal influenza during pregnancy. European Journal of Obstetrics & Gynecology and Reproductive Biology 2021; 258:235-239.

163. Jamieson DJ, Honein MA, Rasmussen SA, Williams JL, Swerdlow DL, Biggerstaff MS, Lindstrom S, Louie JK, Christ CM, Bohm SR, Fonseca VP, Ritger KA, et al. H1N1 2009 influenza virus infection during pregnancy in the USA. Lancet 2009; 374:451-458.

164. Mertz D, Geraci J, Winkup J, Gessner BD, Ortiz JR, Loeb M. Pregnancy as a risk factor for severe outcomes from influenza virus infection: A systematic review and meta-analysis of observational studies. Vaccine 2017; 35:521-528.

165. Mertz D, Lo CKF, Lytvyn L, Ortiz JR, Loeb M, Ang LW, Anlikumar MA, Bonmarin I, Borja-Aburto VH, Burgmann H, Carratala J, Chowell G, et al. Pregnancy as a risk factor for severe influenza infection: an individual participant data meta-analysis. Bmc Infectious Diseases 2019; 19.

166. Rasmussen SA, Jamieson DJ. Influenza and Pregnancy: No Time for Complacency. Obstet Gynecol 2019; 133:23-26.

167. Wang RT, Yan WX, Du M, Tao LY, Liu J. The effect of influenza virus infection on pregnancy outcomes: A systematic review and meta-analysis of cohort studies. International Journal of Infectious Diseases 2021; 105:567-578.

168. WHO. Vaccines against influenza: WHO position paper. In: Weekly Epidemiological Record; 2022: 185-208.

169. Chan KH, Zhang AJX, To KKW, Chan CCS, Poon VKM, Guo KY, Ng F, Zhang QW, Leung VHC, Cheung ANY, Lau CCY, Woo PCY, et al. Wild Type and Mutant 2009 Pandemic Influenza A (H1N1) Viruses Cause More Severe Disease and Higher Mortality in Pregnant BALB/c Mice. Plos One 2010; 5.

170. Lauzon-Joset JF, Scott NM, Mincham KT, Stumbles PA, Holt PG, Strickland DH. Pregnancy Induces a Steady-State Shift in Alveolar Macrophage M1/M2 Phenotype That Is Associated With a Heightened Severity of Influenza Virus Infection: Mechanistic Insight Using Mouse Models. Journal of Infectious Diseases 2019; 219:1823-1831.

171. Littauer EQ, Esser ES, Antao OQ, Vassilieva EV, Compans RW, Skountzou I. H1N1 influenza virus infection results in adverse pregnancy outcomes by disrupting tissue-specific hormonal regulation. PLoS Pathog 2017; 13:e1006757.

172. Littauer EQ, Skountzou I. Hormonal Regulation of Physiology, Innate Immunity and Antibody Response to H1N1 Influenza Virus Infection During Pregnancy. Front Immunol 2018; 9:2455.

173. Marcelin G, Aldridge JR, Duan SS, Ghoneim HE, Rehg J, Marjuki H, Boon ACM, McCullers JA, Webby RJ. Fatal Outcome of Pandemic H1N1 2009 Influenza Virus Infection Is Associated with Immunopathology and Impaired Lung Repair, Not Enhanced Viral Burden, in Pregnant Mice. Journal of Virology 2011; 85:11208-11219.

174. Swieboda D, Littauer EQ, Beaver JT, Mills LK, Bricker KM, Esser ES, Antao OQ, Williams DT, Skountzou I. Pregnancy Downregulates Plasmablast Metabolic Gene

Expression Following Influenza Without Altering Long-Term Antibody Function. Frontiers in Immunology 2020; 11.

175. Liong S, Oseghale O, To EE, Brassington K, Erlich JR, Luong R, Liong F, Brooks R, Martin C, O'Toole S, Vinh A, O'Neill LAJ, et al. Influenza A virus causes maternal and fetal pathology via innate and adaptive vascular inflammation in mice. Proc Natl Acad Sci U S A 2020; 117:24964-24973.

176. Vermillion MS, Nelson A, Vom Steeg L, Loube J, Mitzner W, Klein SL. Pregnancy preserves pulmonary function following influenza virus infection in C57BL/6 mice. Am J Physiol Lung Cell Mol Physiol 2018; 315:L517-L525.

177. Engels G, Hierweger AM, Hoffmann J, Thieme R, Thiele S, Bertram S, Dreier C, Resa-Infante P, Jacobsen H, Thiele K, Alawi M, Indenbirken D, et al. Pregnancy-Related Immune Adaptation Promotes the Emergence of Highly Virulent H1N1 Influenza Virus Strains in Allogenically Pregnant Mice. Cell Host Microbe 2017; 21:321-333.

178. Antonson AM, Kenney AD, Chen HJ, Corps KN, Yount JS, Gur TL. Moderately pathogenic maternal influenza A virus infection disrupts placental integrity but spares the fetal brain. Brain Behav Immun 2021; 96:28-39.

179. Lieberman RW, Bagdasarian N, Thomas D, Van De Ven C. Seasonal influenza A (H1N1) infection in early pregnancy and second trimester fetal demise. Emerg Infect Dis 2011; 17:107-109.

180. Matrai A, Teutsch B, Varadi A, Hegyi P, Petho B, Fujisawa A, Vancsa S, Lintner B, Melczer Z, Acs N. First-Trimester Influenza Infection Increases the Odds of Non-Chromosomal Birth Defects: A Systematic Review and Meta-Analysis. Viruses 2022; 14.

181. Prager S, Dalton VK, Allen RH, Bulletins ACP. Early Pregnancy Loss. Obstetrics and Gynecology 2018; 132:E197-E207.

182. Hu M, Zhou N, Cai W, Xu H. Lysosomal solute and water transport. J Cell Biol 2022; 221.

183. DiCiccio JE, Steinberg BE. Lysosomal pH and analysis of the counter ion pathways that support acidification. J Gen Physiol 2011; 137:385-390.

184. Eaton AF, Merkulova M, Brown D. The H(+)-ATPase (V-ATPase): from proton pump to signaling complex in health and disease. Am J Physiol Cell Physiol 2021; 320:C392-C414.

185. Wang S, Han Y, Nabben M, Neumann D, Luiken J, Glatz JFC. Endosomal v-ATPase as a Sensor Determining Myocardial Substrate Preference. Metabolites 2022; 12.

186. Forgac M. Structure and properties of the vacuolar (H+)-ATPases. J Biol Chem 1999; 274:12951-12954.

187. Di Paola S, Scotto-Rosato A, Medina DL. TRPML1: The Ca((2+))retaker of the lysosome. Cell Calcium 2018; 69:112-121.

188. Venkatachalam K, Wong CO, Zhu MX. The role of TRPMLs in endolysosomal trafficking and function. Cell Calcium 2015; 58:48-56.

189. Chandra M, Zhou H, Li Q, Muallem S, Hofmann SL, Soyombo AA. A role for the Ca2+ channel TRPML1 in gastric acid secretion, based on analysis of knockout mice. Gastroenterology 2011; 140:857-867.

190. Wang W, Zhang X, Gao Q, Xu H. TRPML1: an ion channel in the lysosome. Handb Exp Pharmacol 2014; 222:631-645.

191. Venugopal B, Browning MF, Curcio-Morelli C, Varro A, Michaud N, Nanthakumar N, Walkley SU, Pickel J, Slaugenhaupt SA. Neurologic, gastric, and opthalmologic pathologies in a murine model of mucolipidosis type IV. Am J Hum Genet 2007; 81:1070-1083.

192. Ye X, Hama K, Contos JJ, Anliker B, Inoue A, Skinner MK, Suzuki H, Amano T, Kennedy G, Arai H, Aoki J, Chun J. LPA3-mediated lysophosphatidic acid signalling in embryo implantation and spacing. Nature 2005; 435:104-108.

193. Ye X. Uterine Luminal Epithelium as the Transient Gateway for Embryo Implantation. Trends Endocrinol Metab 2020; 31:165-180.

194. Lee SH, Rho J, Jeong D, Sul JY, Kim T, Kim N, Kang JS, Miyamoto T, Suda T, Lee SK, Pignolo RJ, Koczon-Jaremko B, et al. v-ATPase V0 subunit d2-deficient mice exhibit impaired osteoclast fusion and increased bone formation. Nat Med 2006; 12:1403-1409.

195. Li P, Hu M, Wang C, Feng X, Zhao Z, Yang Y, Sahoo N, Gu M, Yang Y, Xiao S, Sah R, Cover TL, et al. LRRC8 family proteins within lysosomes regulate cellular osmoregulation and enhance cell survival to multiple physiological stresses. Proc Natl Acad Sci U S A 2020; 117:29155-29165.

196. Wang Z, El Zowalaty AE, Li Y, Andersen CL, Ye X. Association of luteal cell degeneration and progesterone deficiency with lysosomal storage disorder mucolipidosis type IV in Mcoln1-/- mouse modeldagger. Biol Reprod 2019; 101:782-790.

197. Li R, Zhao F, Diao H, Xiao S, Ye X. Postweaning dietary genistein exposure advances puberty without significantly affecting early pregnancy in C57BL/6J female mice. Reprod Toxicol 2014; 44:85-92.

198. Zhao F, Zhou J, El Zowalaty AE, Li R, Dudley EA, Ye X. Timing and recovery of postweaning exposure to diethylstilbestrol on early pregnancy in CD-1 mice. Reprod Toxicol 2014; 49C:48-54.

199. Wang Z, El Zowalaty AE, Li Y, Andersen CL, Ye X. Association of luteal cell degeneration and progesterone deficiency with lysosomal storage disorder MLIV in Mcoln1-/- mouse model. Biol Reprod 2019.

200. Wang Y, Liu M, Johnson SB, Yuan G, Arriba AK, Zubizarreta ME, Chatterjee S, Nagarkatti M, Nagarkatti P, Xiao S. Doxorubicin obliterates mouse ovarian reserve through both primordial follicle atresia and overactivation. Toxicol Appl Pharmacol 2019; 381:114714.

201. Duffy DM, Ko C, Jo M, Brannstrom M, Curry TE. Ovulation: Parallels With Inflammatory Processes. Endocr Rev 2019; 40:369-416.

202. Wakabayashi K, Gustafson AM, Sidransky E, Goldin E. Mucolipidosis type IV: an update. Mol Genet Metab 2011; 104:206-213.

203. Soyombo AA, Tjon-Kon-Sang S, Rbaibi Y, Bashllari E, Bisceglia J, Muallem S, Kiselyov K. TRP-ML1 regulates lysosomal pH and acidic lysosomal lipid hydrolytic activity. J Biol Chem 2006; 281:7294-7301.

204. Jennings JJ, Jr., Zhu JH, Rbaibi Y, Luo X, Chu CT, Kiselyov K. Mitochondrial aberrations in mucolipidosis Type IV. J Biol Chem 2006; 281:39041-39050.

205. Li Y, Wang Z, Andersen CL, Ye X. Functions of Lysosomes in Mammalian Female Reproductive System. Reprod Dev Med 2020; 4:109-122.

206. Long JA, Evans HM. The oestrous cycle in the rat and its associated phenomena. Mem. Univ. Calif. 1922; 6:1-148.

207. Tantayaporn P, Mallikarjuneswara VR, de Carlo J, Clemetson CA. The effects of estrogen and progesterone on the volume and electrolyte content of the uterine luminal fluid of the rat. Endocrinology 1974; 95:1034-1045.

208. Parr MB. Effects of ovarian hormones on endocytosis at the basal membranes of rat uterine epithelial cells. Biol Reprod 1982; 26:909-913.

209. Parr MB, Parr EL. Endocytosis in the rat uterine epithelium at implantation. Ann N Y Acad Sci 1986; 476:110-121.

210. Zhang Y, Chen Q, Zhang H, Wang Q, Li R, Jin Y, Wang H, Ma T, Qiao J, Duan E. Aquaporin-dependent excessive intrauterine fluid accumulation is a major contributor in hyper-estrogen induced aberrant embryo implantation. Cell Res 2015; 25:139-142.

211. Armstrong DT. Hormonal cohtrol of uterine lumen fluid retention in the rat. Am J Physiol 1968; 214:764-771.

212. Li S, Garcia M, Gewiss RL, Winuthayanon W. Crucial role of estrogen for the mammalian female in regulating semen coagulation and liquefaction in vivo. PLoS Genet 2017; 13:e1006743.

213. Anamthathmakula P, Winuthayanon W. Mechanism of semen liquefaction and its potential for a novel non-hormonal contraceptiondagger. Biol Reprod 2020; 103:411-426.

214. Simintiras CA, Drum JN, Liu H, Sofia Ortega M, Spencer TE. Uterine lumen fluid is metabolically semi-autonomous. Commun Biol 2022; 5:191.

215. Kelleher AM, DeMayo FJ, Spencer TE. Uterine Glands: Developmental Biology and Functional Roles in Pregnancy. Endocr Rev 2019.

216. Cha J, Sun X, Dey SK. Mechanisms of implantation: strategies for successful pregnancy. Nat Med 2012; 18:1754-1767.

217. Chien LW, Au HK, Xiao J, Tzeng CR. Fluid accumulation within the uterine cavity reduces pregnancy rates in women undergoing IVF. Hum Reprod 2002; 17:351-356.

218. Lu S, Peng H, Zhang H, Zhang L, Cao Q, Li R, Zhang Y, Yan L, Duan E, Qiao J. Excessive intrauterine fluid cause aberrant implantation and pregnancy outcome in mice. PLoS One 2013; 8:e78446.

219. Levi AJ, Segars JH, Miller BT, Leondires MP. Endometrial cavity fluid is associated with poor ovarian response and increased cancellation rates in ART cycles. Hum Reprod 2001; 16:2610-2615.

220. Palagiano A, Cozzolino M, Ubaldi FM, Palagiano C, Coccia ME. Effects of Hydrosalpinx on Endometrial Implantation Failures: Evaluating Salpingectomy in Women Undergoing in vitro fertilization. Rev Bras Ginecol Obstet 2021; 43:304-310.

221. Zhao F, Li R, Xiao S, Diao H, Viveiros MM, Song X, Ye X. Postweaning exposure to dietary zearalenone, a mycotoxin, promotes premature onset of puberty and disrupts early pregnancy events in female mice. Toxicol Sci 2013; 132:431-442.

222. Zhao F, Zhou J, Li R, Dudley EA, Ye X. Novel function of LHFPL2 in female and male distal reproductive tract development. Sci Rep 2016; 6:23037.

223. Butterworth MB. Regulation of the epithelial sodium channel (ENaC) by membrane trafficking. Biochim Biophys Acta 2010; 1802:1166-1177.

224. Chan HC, Liu CQ, Fong SK, Law SH, Leung PS, Leung PY, Fu WO, Cheng Chew SB, Wong PY. Electrogenic ion transport in the mouse endometrium: functional aspects of the cultured epithelium. Biochim Biophys Acta 1997; 1356:140-148.

225. Hanukoglu I, Hanukoglu A. Epithelial sodium channel (ENaC) family: Phylogeny, structure-function, tissue distribution, and associated inherited diseases. Gene 2016; 579:95-132.

226. Skou JC. The Identification of the Sodium-Potassium Pump (Nobel Lecture). Angew Chem Int Ed Engl 1998; 37:2320-2328.

227. Agre P. The aquaporin water channels. Proc Am Thorac Soc 2006; 3:5-13.

228. Papadopoulos MC, Verkman AS. Aquaporin water channels in the nervous system. Nat Rev Neurosci 2013; 14:265-277.

229. Henderson SW, Nourmohammadi S, Ramesh SA, Yool AJ. Aquaporin ion conductance properties defined by membrane environment, protein structure, and cell physiology. Biophys Rev 2022; 14:181-198.

230. Pellavio G, Laforenza U. Human sperm functioning is related to the aquaporin-mediated water and hydrogen peroxide transport regulation. Biochimie 2021; 188:45-51.

231. Richard C, Gao J, Brown N, Reese J. Aquaporin water channel genes are differentially expressed and regulated by ovarian steroids during the periimplantation period in the mouse. Endocrinology 2003; 144:1533-1541.

232. Enders AC, Nelson DM. Pinocytotic activity of the uterus of the rat. Am J Anat 1973; 138:277-299.

233. Martel D, Monier MN, Roche D, Psychoyos A. Hormonal dependence of pinopode formation at the uterine luminal surface. Hum Reprod 1991; 6:597-603.

234. Bartosch C, Lopes JM, Beires J, Sousa M. Human endometrium ultrastructure during the implantation window: a new perspective of the epithelium cell types. Reprod Sci 2011; 18:525-539.

235. Huang DM, Nardo LG, Huang GY, Lu FE, Liu YJ. Effect of a single dose of mifepristone on expression of pinopodes in endometrial surface of mice. Acta Pharmacol Sin 2005; 26:212-219.

236. Murr SM, Stabenfeldt GH, Bradford GE, Geschwind, II. Plasma progesterone during pregnancy in the mouse. Endocrinology 1974; 94:1209-1211.

237. Kosaka T, Saito TR, Takahashi KW. Changes in plasma progesterone levels during the estrous cycle and pregnancy in 4-day cyclic mice. Jikken Dobutsu 1988; 37:351-353.

238. Virgo BB, Bellward GD. Serum progesterone levels in the pregnant and postpartum laboratory mouse. Endocrinology 1974; 95:1486-1490.

239. Diao H, Paria BC, Xiao S, Ye X. Temporal expression pattern of progesterone receptor in the uterine luminal epithelium suggests its requirement during early events of implantation. Fertil Steril 2011; 95:2087-2093.

240. Michael Danielsen E, Hansen GH. Small molecule pinocytosis and clathrin-dependent endocytosis at the intestinal brush border: Two separate pathways into the enterocyte. Biochim Biophys Acta 2016; 1858:233-243.

241. Monici M. Cell and tissue autofluorescence research and diagnostic applications. Biotechnol Annu Rev 2005; 11:227-256.

242. Li F, Yang M, Wang L, Williamson I, Tian F, Qin M, Shah PK, Sharifi BG. Autofluorescence contributes to false-positive intracellular Foxp3 staining in macrophages: a lesson learned from flow cytometry. J Immunol Methods 2012; 386:101-107.

243. Buchwalow I, Atiakshin D, Samoilova V, Boecker W, Tiemann M. Identification of autofluorescent cells in human angioimmunoblastic T-cell lymphoma. Histochem Cell Biol 2018; 149:169-177.

244. Walsh AJ, Mueller KP, Tweed K, Jones I, Walsh CM, Piscopo NJ, Niemi NM, Pagliarini DJ, Saha K, Skala MC. Classification of T-cell activation via autofluorescence lifetime imaging. Nat Biomed Eng 2021; 5:77-88.

245. Parr MB, Parr EL. Uptake and fate of ferritin in the uterine epithelium of the rat during early pregnancy. J Reprod Fertil 1978; 52:183-188.

246. Parr MB, Parr EL. Uterine luminal epithelium: protrusions mediate endocytosis, not apocrine secretion, in the rat. Biol Reprod 1974; 11:220-233.

247. Chinigarzadeh A, Muniandy S, Salleh N. Estrogen, progesterone, and genistein differentially regulate levels of expression of alpha-, beta-, and gamma-epithelial sodium channel (ENaC) and alpha-sodium potassium pump (Na(+)/K(+)-ATPase) in the uteri of sex steroid-deficient rats. Theriogenology 2015; 84:911-926.

248. Nishimura H, Fan Z. Regulation of water movement across vertebrate renal tubules. Comp Biochem Physiol A Mol Integr Physiol 2003; 136:479-498.

249. Masyuk AI, Marinelli RA, LaRusso NF. Water transport by epithelia of the digestive tract. Gastroenterology 2002; 122:545-562.

250. MacAulay N. Molecular mechanisms of brain water transport. Nat Rev Neurosci 2021; 22:326-344.

251. Wang XF, Chan HC. Adenosine triphosphate induces inhibition of Na(+) absorption in mouse endometrial epithelium: a Ca(2+)-dependent mechanism. Biol Reprod 2000; 63:1918-1924.

252. Tsang LL, Chan LN, Wang XF, So SC, Yuen JP, Fiscus RR, Chan HC. Enhanced epithelial Na(+) channel (ENaC) activity in mouse endometrial epithelium by upregulation of gammaENaC subunit. Jpn J Physiol 2001; 51:539-543.

253. Matthews CJ, McEwan GT, Redfern CP, Thomas EJ, Hirst BH. Bradykinin stimulation of electrogenic ion transport in epithelial layers of cultured human endometrium. Pflugers Arch 1993; 422:401-403.

254. Matthews CJ, McEwan GT, Redfern CP, Thomas EJ, Hirst BH. Absorptive apical amiloride-sensitive Na+ conductance in human endometrial epithelium. J Physiol 1998; 513 (Pt 2):443-452.

255. Vetter AE, O'Grady SM. Sodium and anion transport across the avian uterine (shell gland) epithelium. J Exp Biol 2005; 208:479-486.

256. Satlin LM, Sheng S, Woda CB, Kleyman TR. Epithelial Na(+) channels are regulated by flow. Am J Physiol Renal Physiol 2001; 280:F1010-1018.

257. Zhang J, Yuan HK, Chen S, Zhang ZR. Detrimental or beneficial: Role of endothelial ENaC in vascular function. J Cell Physiol 2022; 237:29-48.

258. Baldin JP, Barth D, Fronius M. Epithelial Na(+) Channel (ENaC) Formed by One or Two Subunits Forms Functional Channels That Respond to Shear Force. Front Physiol 2020; 11:141.

259. McCormack JT, Greenwald GS. Progesterone and oestradiol-17beta concentrations in the peripheral plasma during pregnancy in the mouse. J Endocrinol 1974; 62:101-107.

260. Staruschenko A, Nichols A, Medina JL, Camacho P, Zheleznova NN, Stockand JD. Rho small GTPases activate the epithelial Na(+) channel. J Biol Chem 2004; 279:49989-49994.

261. Karpushev AV, Ilatovskaya DV, Pavlov TS, Negulyaev YA, Staruschenko A. Intact cytoskeleton is required for small G protein dependent activation of the epithelial Na+ channel. PLoS One 2010; 5:e8827.

262. Li Y, Konstantopoulos K, Zhao R, Mori Y, Sun SX. The importance of water and hydraulic pressure in cell dynamics. J Cell Sci 2020; 133.

263. Parr MB, Parr EL. Endocytosis in the uterine epithelium of the mouse. J Reprod Fertil 1977; 50:151-153.

264. Parr MB. Relationship of uterine closure to ovarian hormones and endocytosis in the rat. J Reprod Fertil 1983; 68:185-188.

265. Ali ST, Lau YC, Shan S, Ryu S, Du Z, Wang L, Xu XK, Chen D, Xiong J, Tae J, Tsang TK, Wu P, et al. Prediction of upcoming global infection burden of influenza seasons after relaxation of public health and social measures during the COVID-19 pandemic: a modelling study. Lancet Glob Health 2022; 10:e1612-e1622.

266. Lee SS, Viboud C, Petersen E. Understanding the rebound of influenza in the post COVID-19 pandemic period holds important clues for epidemiology and control. Int J Infect Dis 2022; 122:1002-1004.

267. Dhanasekaran V, Sullivan S, Edwards KM, Xie R, Khvorov A, Valkenburg SA, Cowling BJ, Barr IG. Human seasonal influenza under COVID-19 and the potential consequences of influenza lineage elimination. Nat Commun 2022; 13:1721.

268. Kwok KO, Riley S, Perera R, Wei VWI, Wu P, Wei L, Chu DKW, Barr IG, Malik Peiris JS, Cowling BJ. Relative incidence and individual-level severity of seasonal influenza A H3N2 compared with 2009 pandemic H1N1. BMC Infect Dis 2017; 17:337.

269. Taubenberger JK, Morens DM. Influenza: the once and future pandemic. Public Health Rep 2010; 125 Suppl 3:16-26.

270. Influenza Virus. Transfus Med Hemother 2009; 36:32-39.

271. Jester BJ, Uyeki TM, Jernigan DB. Fifty Years of Influenza A(H3N2) Following the Pandemic of 1968. Am J Public Health 2020; 110:669-676.

272. Merced-Morales A, Daly P, Abd Elal AI, Ajayi N, Annan E, Budd A, Barnes J, Colon A, Cummings CN, Iuliano AD, DaSilva J, Dempster N, et al. Influenza Activity and Composition of the 2022-23 Influenza Vaccine - United States, 2021-22 Season. Mmwr-Morbidity and Mortality Weekly Report 2022; 71:913-919.

273. Belongia EA, Simpson MD, King JP, Sundaram ME, Kelley NS, Osterholm MT, McLean HQ. Variable influenza vaccine effectiveness by subtype: a systematic review and meta-analysis of test-negative design studies. Lancet Infect Dis 2016; 16:942-951.

274. Gouma S, Kim K, Weirick ME, Gumina ME, Branche A, Topham DJ, Martin ET, Monto AS, Cobey S, Hensley SE. Middle-aged individuals may be in a perpetual state of H3N2 influenza virus susceptibility. Nature Communications 2020; 11.

275. Kang M, Zanin M, Wong SS. Subtype H3N2 Influenza A Viruses: An Unmet Challenge in the Western Pacific. Vaccines (Basel) 2022; 10.

276. Liang W, Tan TJC, Wang Y, Lv H, Sun Y, Bruzzone R, Mok CKP, Wu NC. Egg-adaptive mutations of human influenza H3N2 virus are contingent on natural evolution. PLoS Pathog 2022; 18:e1010875.

277. Tenforde MW, Patel MM, Lewis NM, Adams K, Gaglani M, Steingrub JS, Shapiro NI, Duggal A, Prekker ME, Peltan ID, Hager DN, Gong MN, et al. Vaccine Effectiveness

Against Influenza A(H3N2)-Associated Hospitalized Illness: United States, 2022. Clinical Infectious Diseases 2022.

278. Hussain M, Galvin HD, Haw TY, Nutsford AN, Husain M. Drug resistance in influenza A virus: the epidemiology and management. Infect Drug Resist 2017; 10:121-134.

279. Giurgea LT, Cervantes-Medina A, Walters KA, Scherler K, Han A, Czajkowski LM, Baus HA, Hunsberger S, Klein SL, Kash JC, Taubenberger JK, Memoli MJ. Sex Differences in Influenza: The Challenge Study Experience. J Infect Dis 2022; 225:715-722.

280. Eshima N, Tokumaru O, Hara S, Bacal K, Korematsu S, Tabata M, Karukaya S, Yasui Y, Okabe N, Matsuishi T. Sex- and age-related differences in morbidity rates of 2009 pandemic influenza A H1N1 virus of swine origin in Japan. PLoS One 2011; 6:e19409.

281. Small CM, Manatunga AK, Klein M, Dominguez CE, Feigelson HS, McChesney R, Marcus M. Menstrual cycle variability and the likelihood of achieving pregnancy. Rev Environ Health 2010; 25:369-378.

282. Small CM, Manatunga AK, Klein M, Feigelson HS, Dominguez CE, McChesney R, Marcus M. Menstrual cycle characteristics: associations with fertility and spontaneous abortion. Epidemiology 2006; 17:52-60.

283. Wise LA, Mikkelsen EM, Rothman KJ, Riis AH, Sorensen HT, Huybrechts KF, Hatch EE. A prospective cohort study of menstrual characteristics and time to pregnancy. Am J Epidemiol 2011; 174:701-709.

284. Ajayi AF, Akhigbe RE. Staging of the estrous cycle and induction of estrus in experimental rodents: an update. Fertil Res Pract 2020; 6:5.

285. Byers SL, Wiles MV, Dunn SL, Taft RA. Mouse estrous cycle identification tool and images. PLoS One 2012; 7:e35538.

286. Robinson DP, Lorenzo ME, Jian W, Klein SL. Elevated 17beta-estradiol protects females from influenza A virus pathogenesis by suppressing inflammatory responses. PLoS Pathog 2011; 7:e1002149.

287. Li K, Chen G, Hou H, Liao Q, Chen J, Bai H, Lee S, Wang C, Li H, Cheng L, Ai J. Analysis of sex hormones and menstruation in COVID-19 women of child-bearing age. Reprod Biomed Online 2021; 42:260-267.

288. Male V. COVID-19 vaccination and menstruation. Science 2022; 378:704-706.

289. Chao MJ, Menon C, Elgendi M. Effect of COVID-19 vaccination on the menstrual cycle. Front Med (Lausanne) 2022; 9:1065421.

290. Male V. Menstruation and covid-19 vaccination. BMJ 2022; 376:o142.

291. Latha K, Jamison KF, Watford WT. Tpl2 Ablation Leads to Hypercytokinemia and Excessive Cellular Infiltration to the Lungs During Late Stages of Influenza Infection. Front Immunol 2021; 12:738490.

292. Li R, Andersen CL, Hu L, Wang Z, Li Y, Nagy T, Ye X. Dietary exposure to mycotoxin zearalenone (ZEA) during post-implantation adversely affects placental development in mice. Reprod Toxicol 2019; 85:42-50.

293. Zowalaty AEE, Ye X. Seipin deficiency leads to defective parturition in mice. Biol Reprod 2017; 97:378-386.

294. Nelson JF, Gosden RG, Felicio LS. Effect of dietary restriction on estrous cyclicity and follicular reserves in aging C57BL/6J mice. Biol Reprod 1985; 32:515-522.

295. Latha K, Rao S, Sakamoto K, Watford WT. Tumor Progression Locus 2 Protects against Acute Respiratory Distress Syndrome in Influenza A Virus-Infected Mice. Microbiology Spectrum 2022.

296. Askovich PS, Sanders CJ, Rosenberger CM, Diercks AH, Dash P, Navarro G, Vogel P, Doherty PC, Thomas PG, Aderem A. Differential host response, rather than early viral replication efficiency, correlates with pathogenicity caused by influenza viruses. PLoS One 2013; 8:e74863.

297. Galvao-Filho B, de Castro JT, Figueiredo MM, Rosmaninho CG, Antonelli L, Gazzinelli RT. The emergence of pathogenic TNF/iNOS producing dendritic cells (Tip-DCs) in a malaria model of acute respiratory distress syndrome (ARDS) is dependent on CCR4. Mucosal Immunol 2019; 12:312-322.

298. Leon B, Ballesteros-Tato A, Randall TD, Lund FE. Prolonged antigen presentation by immune complex-binding dendritic cells programs the proliferative capacity of memory CD8 T cells. J Exp Med 2014; 211:1637-1655.

299. Norden DM, Bethea JR, Jiang J. Impaired CD8 T cell antiviral immunity following acute spinal cord injury. J Neuroinflammation 2018; 15:149.

300. To EE, Erlich J, Liong F, Luong R, Liong S, Bozinovski S, Seow HJ, O'Leary JJ, Brooks DA, Vlahos R, Selemidis S. Intranasal and epicutaneous administration of Toll-like receptor 7 (TLR7) agonists provides protection against influenza A virus-induced morbidity in mice. Sci Rep 2019; 9:2366.

301. Wang YH, Noyer L, Kahlfuss S, Raphael D, Tao AY, Kaufmann U, Zhu J, Mitchell-Flack M, Sidhu I, Zhou F, Vaeth M, Thomas PG, et al. Distinct roles of ORAI1 in T cell-

mediated allergic airway inflammation and immunity to influenza A virus infection. Sci Adv 2022; 8:eabn6552.

302. Xu T, Qiao J, Zhao L, Wang G, He G, Li K, Tian Y, Gao M, Wang J, Wang H, Dong C. Acute respiratory distress syndrome induced by avian influenza A (H5N1) virus in mice. Am J Respir Crit Care Med 2006; 174:1011-1017.

303. Narasaraju T, Yang E, Samy RP, Ng HH, Poh WP, Liew AA, Phoon MC, van Rooijen N, Chow VT. Excessive neutrophils and neutrophil extracellular traps contribute to acute lung injury of influenza pneumonitis. Am J Pathol 2011; 179:199-210.

304. Bin NR, Prescott SL, Horio N, Wang Y, Chiu IM, Liberles SD. An airway-to-brain sensory pathway mediates influenza-induced sickness. Nature 2023.

305. Gabloffsky T, Gill S, Staffeld A, Salomon R, Power Guerra N, Joost S, Hawlitschka A, Kipp M, Frintrop L. Food Restriction in Mice Induces Food-Anticipatory Activity and Circadian-Rhythm-Related Activity Changes. Nutrients 2022; 14.

306. Webber LJ, Stubbs S, Stark J, Trew GH, Margara R, Hardy K, Franks S. Formation and early development of follicles in the polycystic ovary. Lancet 2003; 362:1017-1021.

307. WorldBank. Fertility rate, total (births per woman). In: World Bank Group; 2023.

308. S.C YENS, Strauss JF, III, Barbieri RL, Gargiulo AR, Yen SSC, Jaffe RB. Yen and Jaffe's reproductive endocrinology : physiology, pathology, and clinical management. Philadelphia: Elsevier; 2019.

309. Shaker M, Smith A. First Trimester Miscarriage. Obstet Gynecol Clin North Am 2022; 49:623-635.

310. Dimitriadis E, Menkhorst E, Saito S, Kutteh WH, Brosens JJ. Recurrent pregnancy loss. Nat Rev Dis Primers 2020; 6:98.

311. Dugas C, Slane VH. Miscarriage. In: StatPearls. Treasure Island (FL); 2022.

312. Zinaman MJ, Clegg ED, Brown CC, O'Connor J, Selevan SG. Estimates of human fertility and pregnancy loss. Fertil Steril 1996; 65:503-509.

313. Hertz-Picciotto I, Samuels SJ. Incidence of early loss of pregnancy. N Engl J Med 1988; 319:1483-1484.

314. Wilcox AJ, Baird DD, Wenberg CR. Time of implantation of the conceptus and loss of pregnancy. New England Journal of Medicine 1999; 340:1796-1799.

315. Huisman GJ, Fauser BCJM, Eijkemans MJC, Pieters MHEC. Implantation rates after in vitro fertilization and transfer of a maximum of two embryos that have undergone three to five days of culture. Fertility and Sterility 2000; 73:117-122.

316. Liang YX, Liu L, Jin ZY, Liang XH, Fu YS, Gu XW, Yang ZM. The high concentration of progesterone is harmful for endometrial receptivity and decidualization. Scientific Reports 2018; 8.

317. Bashiri A, Halper KI, Orvieto R. Recurrent Implantation Failure-update overview on etiology, diagnosis, treatment and future directions. Reproductive Biology and Endocrinology 2018; 16.

318. Wetendorf M, DeMayo FJ. The progesterone receptor regulates implantation, decidualization, and glandular development via a complex paracrine signaling network. Molecular and Cellular Endocrinology 2012; 357:108-118.

319. Cakmak H, Taylor HS. Implantation failure: molecular mechanisms and clinical treatment. Human Reproduction Update 2011; 17:242-253.

320. Daya S. Efficacy of Progesterone Support for Pregnancy in Women with Recurrent Miscarriage - a Meta-Analysis of Controlled Trials. British Journal of Obstetrics and Gynaecology 1989; 96:275-280.

321. Parenti G, Medina DL, Ballabio A. The rapidly evolving view of lysosomal storage diseases. EMBO Mol Med 2021; 13:e12836.

322. Rajkumar V, Dumpa V. Lysosomal Storage Disease. In: StatPearls. Treasure Island (FL); 2023.

323. Sharma S, Majumdar A. Determining the Optimal Duration of Progesterone Supplementation prior to Transfer of Cryopreserved Embryos and Its Impact on Implantation and Pregnancy Rates: A Pilot Study. Int J Reprod Med 2016; 2016:7128485.

324. Omidi M, Halvaei I, Akyash F, Khalili MA, Agha-Rahimi A, Heydari L. The exact synchronization timing between the cleavage embryo stage and duration of progesterone therapy-improved pregnancy rates in frozen embryo transfer cycles: A cross-sectional study. International Journal of Reproductive Biomedicine 2021; 19:227-234.

325. Bulletti C, Bulletti FM, Sciorio R, Guido M. Progesterone: The Key Factor of the Beginning of Life. Int J Mol Sci 2022; 23.